Magnetic Tunnel Junctions and Superconductor/Ferromagnet Hybrids Investigated by Low-Temperature Scanning Laser Microscopy

Dissertation
der Mathematisch-Naturwissenschaftlichen Fakultät
der Eberhard Karls Universität Tübingen
zur Erlangung des Grades eines
Doktors der Naturwissenschaften
(Dr. rer. nat.)

vorgelegt von
Robert Werner
aus Laupheim

Tübingen
2011

Tag der mündlichen Qualifikation:	1. Februar 2012
Dekan:	Prof. Dr. Wolfgang Rosenstiel
1. Berichterstatter:	Prof. Dr. Dieter Kölle
2. Berichterstatter:	Prof. Dr. Reinhold Kleiner

Abstract

Low-temperature scanning laser microscopy (LTSLM) allows the investigation of local properties in thin film structures in a broad temperature range. Depending on the sample under investigation, LTSLM can map various kinds of physical properties such as the current distribution or the magnetic microstructure. In this thesis, the correlation between local and integral magnetotransport properties in thin-film superconductor/ferromagnet (S/F) hybrids and magnetic tunnel junctions are investigated.

In S/F hybrids composed of Pb/$BaFe_{12}O_{19}$, we studied experimentally the effect of the stripe like domain structure of the $BaFe_{12}O_{19}$ substrate on the magnetoresistance of superconducting Pb microbridges. A thin insulating layer between Pb and the ferromagnet ensures pure electromagnetic coupling between the antagonistic phenomena of singlet superconductivity and ferromagnetism. Two bridges with different orientation with respect to the stripe-like domain walls (parallel and perpendicular) were probed by LTSLM. In this technique, the sample is locally heated in the thin film (x, y) plane by a laser beam, which can induce a detectable voltage change $\Delta V(x, y)$, depending on the physical properties of the heated area. The resulting voltage images can visualize various physical properties, depending on the investigated sample. Direct verification of the formation of inhomogeneous superconducting states in the Pb bridges, induced by the inhomogeneous stray field of the ferromagnet and their manipulation by an external magnetic field were obtained by LTSLM. In particular, the localized state of domain-wall superconductivity was visualized in a sample where exactly one domain wall is running along the center of the Pb bridge, inducing a superconducting path for the current. Another state of localized superconductivity, called edge superconductivity, was probed in Nb microbridges. In an external magnetic field applied perpendicular to the sample surface, superconductivity survives at the edges even for fields larger than the upper critical field H_{c2} for bulk superconductivity.

The interaction between superconductivity and ferromagnetism was also studied in heteroepitaxially grown bilayers composed of ferromagnetic $La_{0.7}Ca_{0.3}MnO_3$ on top of superconducting $YBa_2Cu_3O_7$ (YBCO). The focus was on transport properties as well as on magnetic ordering and orbital occupation at the interface. We found, that a significant reduction of the superconducting transition temperature T_c of single YBCO thin films occurs only for a layer thickness below 10 nm. The suppression of T_c in the bilayers was only slightly stronger compared to single YBCO films. Our x-ray magnetic circular dichroism measurements confirm recently published data of an induced magnetic moment on the interfacial Cu by the ferromagnetically ordered Mn ions. However, we observe a significantly larger Cu moment than previously reported, indicating stronger coupling between Cu and Mn at the interface. This can explain the reduced suppression of T_c in our samples.

Magnetic tunnel junctions (MTJs) were investigated by LTSLM to correlate integral magnetotransport measurements with local sample properties. We have performed resistance versus magnetic field measurements for a MTJ based on $La_{0.65}Sr_{0.35}MnO_3$ (LSMO) with $SrTiO_3$ barrier, grown by molecular-beam epitaxy. Magnetoresistance measurements show a large field window of extremely high tunneling magnetoresis-

tance (TMR) at low temperature which reached about 1900 %. This is the highest TMR value reported so far. Assuming identical interfaces, this TMR ratio corresponds to an interfacial spin polarization of $\sim 95\,\%$. Studies with LTSLM allow the determination of the local relative magnetization orientation of the two electrodes as a function of magnitude and orientation of the external magnetic field. Sweeping the field amplitude at fixed orientation revealed magnetic domain nucleation and propagation in the junction electrodes. The results show that LTSLM can be used to link the magnetic microstructure to the integral magnetotransport properties and thus provides a valuable tool for further investigations of MTJs. Moreover, the obtained information on the relative magnetization orientation could not be obtained by any other imaging technique, so far.

Kurzfassung

Die Tieftemperatur-Rasterlasermikroskopie (TTRLM) ermöglicht die Untersuchung lokaler Eigenschaften von Dünnfilmstrukturen in einem breiten Temperaturbereich. Abhängig von der untersuchten Probe lassen sich durch die TTRLM verschiedenste physikalische Eigenschaften wie zum Beispiel die Stromverteilung oder die magnetische Mikrostruktur abbilden. In dieser Arbeit wird die Beziehung zwischen lokalen und integralen Magnetotransport-Eigenschaften von Dünnfilmstrukturen aus Supraleiter/Ferromagnet Hybriden und magnetischen Tunnelkontakten untersucht. In S/F Hybriden aus Pb/$BaFe_{12}O_{19}$ wurde experimentell der Effekt der ferromagnetischen Streifendomänen des $BaFe_{12}O_{19}$ Substrates auf den Magnetowiderstand von supraleitenden Pb Brücken untersucht. Eine dünne isolierende Schicht zwischen Pb und dem Ferromagnet garantiert eine rein elektromagnetische Wechselwirkung zwischen den gegensätzlichen Phänomenen von Spin-Singulett Supraleitung und Ferromagnetismus. Es wurden zwei Brücken mit unterschiedlicher Orientierung bezüglich der streifenartigen Domänen (parallel oder senkrecht) mittels TTRLM untersucht. Bei dieser Technik wird die Probe lokal in der Filmebene (x, y) mit einem Laser erwärmt. Je nach Eigenschaft der bestrahlten Fläche kann dies zu einer messbaren Spannungsänderung $\Delta V(x, y)$ führen. Die dabei entstehenden Spannungsbilder können verschiedenste physikalische Eigenschaften abbilden. Mit Hilfe der TTRLM konnte ein direkter Nachweis von Zuständen inhomogener Supraleitung in den Pb Brücken erbracht werden. Desweiteren konnte gezeigt werden, dass sich die Zustände durch ein externes Magnetfeld manipulieren lassen. Insbesondere wurde der Zustand der Domänenwandsupraleitung in einer Brücke abgebildet, in der genau eine einzige Domänenwand entlang der Mitte der Brücke verläuft und welche einen als supraleitenden Pfad für den Strom induziert. Ein weiterer Zustand lokalisierter Supraleitung wurde in Nb Brücken untersucht, die sogenannte Randsupraleitung. Dabei existiert die Supraleitung an den Probenrändern in einem externen Magnetfeld senkrecht zur Probenoberfläche, auch wenn das Feld größer als das obere kritische Feld H_{c2} ist.

Die Wechselwirkung von Supraleitung und Ferromagnetismus wurde auch in heteroepitaktisch gewachsenen Bilagen aus ferromagnetischem $La_{0.7}Ca_{0.3}MnO_3$ und supraleitendem $YBa_2Cu_3O_7$ (YBCO) untersucht. Dabei lag der Schwerpunkt auf den Transporteigenschaften sowie der magnetischen Ordnung und den elektronischen Eigenschaften an der Grenzfläche. Eine deutliche Unterdrückung der kritischen Temperatur T_c von YBCO Dünnfilmen trat erst unterhalb einer Dicke von 10 nm auf. In Bilagen war die Unterdrückung im Vergleich zu einzelnen YBCO Dünnfilmen nur etwas stärker. Mit Hilfe von Röntgenabsorptionsspektroskopie mit zirkular polarisierten Röntgenstrahlen konnten kürzlich erschienene Messungen eines induzierten magnetischen Moments auf Cu Atomen durch die ferromagnetisch geordneten Mn Momente an der Grenzfläche bestätigt werden. Jedoch zeigte die vermessene Probe ein deutlich stärkeres Cu Moment, was für eine stärkere Wechselwirkung an der Grenzfläche spricht. Dies könnte die relativ geringe Unterdrückung von T_c in unseren Proben erklären.

Magnetische Tunnelkontakte (MTK) wurden mittels TTRLM untersucht um die lokalen und integralen Eigenschaft miteinander zu korrelieren. An $La_{0.65}Sr_{0.35}MnO_3$

(LSMO) basierten MTK mit $SrTiO_3$ Barriere wurden Widerstandsmessungen in Abhängigkeit vom äußeren Magnetfeld durchgeführt. Die LSMO/$SrTiO_3$/LSMO Trilagen wurden mittels Molekularstrahlepitaxie gewachsen. Widerstandsmessungen in Abhängigkeit des äußeren Magnetfeldes zeigen einen großen Magnetfeldbereich mit sehr hohem Tunnelmagnetowiderstand (TMR), welcher bei tiefen Temperaturen einen Wert von bis zu $\sim 1900\,\%$ erreicht. Dies ist bisher der höchste gemessene TMR Wert überhaupt. Unter der Annahme von identischen Grenzflächen ergibt sich daraus eine Spinpolarisation an den Grenzflächen von ungefähr $95\,\%$. Mit Hilfe der Abbildungen konnte lokal die relative Magnetisierung in Abhängigkeit von Richtung und Größe des angelegten Magnetfeldes bestimmt werden. Beim Durchfahren des Magnetfeldes zeigen die Abbildungen die Bildung und die Ausbreitung von Domänen in den ferromagnetischen Elektroden. Die Ergebnisse zeigen, dass durch TTRLM eine Beziehung zwischen der lokalen magnetischen Struktur und den integralen Magnetowiederstandskurven hergestellt werden kann. Darüber hinaus erhält man Information über die Verteilung der relativen Orientierung der Magnetisierung beider Elektroden, was bisher mit keiner anderen Abbildungstechnik möglich war.

List of publications

This is a cumulative thesis which is based on the publications listed below. They are referred to in the text by their roman numerals. The publications are attached at the very end of the thesis.

Appended publications

I A.Yu. Aladyshkin, J. Fritzsche, **R. Werner**, R.B.G. Kramer, S. Guénon, R. Kleiner, D. Koelle and V.V. Moshchalkov,
Crossover between different regimes of inhomogeneous superconductivity in planar superconductor-ferromagnet hybrids,
Phys. Rev. B **84**, 094523 (2011)

II **R. Werner**, A.Yu. Aladyshkin, S. Guénon, J. Fritzsche, I.M. Nefedov, V.V. Moshchalkov, R. Kleiner and D. Koelle,
Domain-wall and reverse-domain superconducting states of a Pb thin-film bridge on a ferromagnetic $BaFe_{12}O_{19}$ single crystal,
Phys. Rev. B **84**, 020505(R) (2011)

III **R. Werner**, A. Yu. Aladyshkin, I. M. Nefedov, A. V. Putilov, M. Kemmler, D. Bothner, A. Loerincz, K. Ilin, M. Siegel, R. Kleiner, and D. Koelle,
Edge superconductivity in Nb thin film microbridges revealed by integral and spatially resolved electric transport,
submitted to Phys. Rev. B (2011), arXiv:1112.2256

IV **R. Werner**, C. Raisch, A. Ruosi, B. A. Davidson, P. Nagel, M. Merz, S. Schuppler, M. Glaser, J. Fujii, T. Chassé, R. Kleiner and D. Koelle, *$YBa_2Cu_3O_7$ / $La_{0.7}Ca_{0.3}MnO_3$ bilayers: Interface coupling and electric transport properties*,
Phys. Rev. B **82**, 224509 (2011)

V **R. Werner**, M. Weiler, A. Yu. Petrov, B. A. Davidson, R. Gross, R. Kleiner, S. T. B. Goennenwein and D. Koelle,
Local Tunneling Magnetoresistance probed by Low-Temperature Scanning Laser Microscopy,
App. Phys. Lett. **99**, 182513 (2011)

VI **R. Werner**, A. Yu. Petrov, L. Alvarez Miño, R. Kleiner, D. Koelle and B. A. Davidson,
Improved tunneling magnetoresistance at low temperature in manganite junctions grown by molecular beam epitaxy,
App. Phys. Lett. **98**, 162505 (2011)

Publications not included in this thesis

VII **R. Werner**, C. Raisch, V. Leca, V. Ion, S. Bals, G. Van Tendeloo, T. Chassé, R. Kleiner and D. Koelle,
Transport, magnetic, and structural properties of $La_{0.7}Ce_{0.3}MnO_3$ *thin films: Evidence for hole-doping*,
Phys. Rev. B **79**, 054416 (2009)

VIII J. Nagel, K. B. Konovalenko, M. Kemmler, M. Turad, **R. Werner**, E. Kleisz, S. Menzel, R. Klingeler, B. Büchner, R. Kleiner and D. Koelle,
Resistively shunted $YBa_2Cu_3O_7$ *grain boundary junctions and low-noise SQUIDs patterned by a focused ion beam down to 80 nm linewidth*,
Supercond. Sci. Technol. **24**, 015015 (2011)

Contents

Introduction

Transition metal oxides with strong electron correlations form since many years an active and constantly growing research field of solid state physics.[1–3] The interplay of spin, charge and orbital degree of freedom leads to a number of different phenomena such as ferroelectricity, ferromagnetism, antiferromagnetism and superconductivity.[4] In strongly correlated electron systems, interfacial properties can be crucial for the macroscopic behavior of the system and they can differ significantly from those of the bulk compounds. This allows for the possibility to create new physical states which do not exist in bulk compounds.[5] The most prominent example of unexpected interface effects is the system $LaAlO_3/SrTiO_3$.[6,7] Though both materials are insulators, a quasi-two dimensional electron liquid is formed at the interface which even becomes superconducting. Another possibility is the combination of oxide materials with different ordering phenomena. Of special interest is the combination of two antagonistic phenomena such as superconductivity and ferromagnetism in an all oxide heterostructure.[8,9] While superconductor/ferromagnet (S/F) hybrid structures based on metallic ferromagnets and conventional superconductors have been investigated in detail,[10] there are much less studies on S/F systems involving oxide materials.[11–14]

Interface properties also determine the characteristics of many devices such as pn-junctions, metal-oxide-semiconductor field-effect transistors or magnetic tunnel junctions (MTJs). In the latter one, the tunnel magnetoresistance (TMR) which is the figure of merit of MTJs, depends on the spin polarization at the interface.[15] The higher the spin polarization, the higher the TMR ratio. It has been shown that the interfacial spin polarization can be increased by the so-called "interface engineering", where the doping profile is gradually changed at the interface.[16,17] Beside that, improving the TMR ratio as well as the switching behavior needs investigations of the impact of the magnetic microstructure on the integral magnetotransport properties. The domain structure is also crucial in electrically decoupled S/F hybrids where the stray field of the ferromagnetic domains can lead to inhomogeneous superconductivity, tunable by an external magnetic field H.[18–22] This leads to a complex $H-T$ phase diagram with various different states of inhomogeneous superconductivity. While fingerprints of this inhomogeneous states have been found in magnetotransport measurements,[19] a clear correlation between integral and local properties is still lacking for most states[22].

Since many years, low-temperature scanning laser microscopy (LTSLM) is used to map various kinds of physical properties such as the critical current or critical temperature distribution in superconducting thin films or the magnetic domain structure in ferromagnetic thin films and to correlate them with integral transport mea-

surements.[22–24] Therefore, LTSLM seems to be a valuable technique, to visualize inhomogeneous properties in S/F hybrids as well as in MTJs.
In the framework of this thesis, the transport and interface properties of S/F hybrids composed of $YBa_2Cu_3O_7$ (YBCO) and $La_{0.7}Ca_{0.3}MnO_3$ (LCMO) have been probed. Due to the similar crystal structure of these materials, it is possible to combine the different ordering phenomena in epitaxial heterostructures with well defined interfaces. The aim of our investigations was to improve the understanding of the influence of LCMO on YBCO transport properties as well as the electronic and magnetic properties at the interface.
MTJs based on the half-metal oxide $La_{0.65}Sr_{0.35}MnO_3$ (LSMO), grown by molecular-beam epitaxy (MBE), were investigated. LSMO has a Curie-temperature well above room temperature and it is, due to its spin polarization of about 100 %, a promising candidate for high TMR ratios at room temperature. We used MBE, as it is the growth technique with the highest growth control on the atomic scale and it allows to adjust the doping level at any time during the growth process. It is therefore the most suitable technique to realize MTJ with engineered interfaces. But first, the idea was to grow and pattern reproducible MTJs and to probe the influence of the local microstructure on the integral magnetotransport by LTSLM.
The technique of LTSLM was also applied to electrically decoupled S/F hybrids composed of $Pb/BaFe_{12}O_{19}$. Here we focused on the electrical characterization of the S/F hybrid and the visualization of inhomogeneous states of superconductivity at different positions in the $H-T$ phase diagram, induced by the stray field of the domain structure in the ferromagnetic substrate. A correlation between local and integral properties should be established. In these studies we included investigations on Nb microbridges, where we probed one particular case of inhomogeneous superconductivity, localized at the samples edges.

This thesis is organized as follows:

The first part of **chapter 1**, gives a general introduction to the field of S/F systems, followed by a detailed overview on states of inhomogeneous superconductivity in electrically decoupled S/F hybrids and superconducting bridges in an external magnetic field. In the following, the signal mechanism of LTSLM which was used to investigate states of inhomogeneous superconductivity is described. Subsequently, the most important findings of the publications dealing with inhomogeneous superconductivity are summarized. The next section gives an introduction to interface effects of electrically coupled YBCO/LCMO bilayers, followed by a summary of the main results.
The content of **chapter 2** are MTJs. The first paragraph gives an introduction to MTJs and describes open issues in this field. The paragraph thereafter summarizes the main results of the electrical characterization of $LSMO/SrTiO_3/LSMO$ MTJs. The last section in this chapter summarized the investigations of local properties of a MTJ by LTSLM. The publications on which this thesis is based on are attached after the bibliography.

Chapter 1

Superconductor/ferromagnet hybrids

This chapter presents investigations on superconductor/ferromagnet hybrids. The first paragraph will briefly introduce the interplay between ferromagnetism and superconductivity and motivate the research. In the framework of this thesis, various aspects of two superconductor/ferromagnet systems have been studied. Electric transport and interface properties were investigated in $YBa_2Cu_3O_7/La_{0.7}Ca_{0.3}MnO_3$ bilayers with both materials in direct electrical contact, while in electrically decoupled $Pb/BaFe_{12}O_{19}$ hybrids, the aim was the visualization of inhomogeneous superconductivity. Although it is not an superconductor/ferromagnet hybrid, studies of inhomogeneous superconductivity in Nb bridges are included in this chapter, as they complete the experiments on $Pb/BaFe_{12}O_{19}$ hybrids.

1.1 Introduction

Superconductivity and ferromagnetism are two ordering phenomena which have been investigated in detail over the past decades. While, initially, both phenomena were investigated separately, the interest in combining and exploring the interaction of both phenomena under various circumstances has been increasing in the last years. Ferromagnetism and superconductivity are two antagonistic phenomena, as ferromagnets tends to align the electron spins parallel, due to the exchange interaction[†], while the superconducting condensate is formed by Cooper-pairs (CPs) which consist of two electrons (or holes) with opposite spin orientation (spin-singlet state). These fundamental differences make it very unlikely to find the phenomena of spin-singlet superconductivity and long-ranged ferromagnetism (FM) in bulk materials. It should be noted, that beside the spin-singlet state ($S = 0$), CPs can also be in the spin-triplet state ($S = 1$), which leads to completely different interaction between superconductivity and ferromagnetism. Only spin-singlet superconductivity will be considered in the following, if not stated otherwise.
The interaction between both phenomena was first considered by Ginzburg,[26] who described the suppression of superconductivity by a pure electromagnetic interaction which will be shortly described in the following. Besides the opposite spin alignment

[†]The exchange interaction is a quantum mechanical effect, based on the Pauli Principle and the coulomb repulsion. For details see Blundell *et al.*.[25]

in spin singlet CPs, the electrons have wavenumbers $\boldsymbol{k}$ with opposite sign, corresponding to an opposite momentum $\boldsymbol{p} = \hbar\boldsymbol{k}$. According to classical electrodynamics, electrons get diffracted in a magnetic field by the Lorentz force $\boldsymbol{F}_L \propto (\boldsymbol{p} \times \boldsymbol{H})$. Since the electrons of the CPs have opposite momentum, the field of the ferromagnet creates a Lorentz force in opposite directions, leading to pair-breaking of the CPs. Such a suppression of superconductivity is called the "orbital effect". Another effect which suppresses superconductivity in presence of FM is the so-called "paramagnetic effect". This effect is based on the exchange interaction between the magnetic moments and the electrons of the CP which favors parallel spin alignment and thus suppresses CP formation. The first experimental investigations of this effect were made by Matthias *et al.*, who observed a reduction of the critical temperature T_c by introducing magnetic impurities in conventional superconductors.[27]

A compromise between both phenomena was theoretically proposed by Anderson and Suhl.[28] They predicted that superconductivity and FM can coexist, if the ferromagnetic domain size is much smaller than the superconducting coherence length ξ_{GL}, which is the length scale for the suppression of the superconducting order parameter. Such a non-uniform magnetic ordering is called "crypto-ferromagnetism". In this case superconductivity can survive, as the CPs see a vanishing averaged magnetization.[29] Alternatively, it was theoretically proposed, that superconductivity and FM can co-exist, if the superconducting order parameter is spatially modulated (FFLO-state).[30–32] While the superconducting ground state is usually characterized by a zero value of the pairing momentum, the exchange field of the ferromagnet leads to a nonzero value of the pairing momentum and thus to a different superconducting state.

Due to the antagonism of both phenomena, the discovery of truly ferromagnetic superconductors like UGe_2 and URhGe was highly unexpected.[33,34] However, it turned out, that the CPs in this materials are not in the spin-singlet state but in the spin-triplet state. Since spin-triplet CPs are formed by electrons with parallel spin-orientation, the paramagnetic-effect can not harm the pairing mechanism and thus superconductivity is not suppressed.

Since the coexistence of superconductivity and long-range FM is very unlikely to exist in bulk compounds, the competing ordering phenomena can be studied in artificial superconductor/ferromagnet (S/F) structures where both phenomena are physically separated. The layers in artificial S/F systems can be either in direct electric contact or they can be electrically decoupled. First, the properties of systems in direct electric contact will be discussed. Typically, the paramagnetic effect is much stronger than the orbital effect and dominates the properties of the system. But in artificial S/F systems, the paramagnetic effect is limited to the interface region. At the interface, CPs penetrate into the ferromagnet (proximity-effect) on a certain length scale while simultaneously spin-polarized particles are injected into the superconductor close to the interface and superconductivity is suppressed (inverse proximity effect)[35]. This coexistence in the interface region results in a unique opportunity to study the interplay of superconductivity and FM. This leads to a large number of interesting physical phenomena such as Josephson π-junctions,[36] long range proximity effect,[37,38] strong magnetoresistance in F/S/F structures,[39,40] induced FM in the superconductor at S/F oxide interfaces[8] and many more. An

overview of S/F structures in electrical contact can be found in recent reviews.[10,41] It should be noted, that only recent progress in thin film growth and sample fabrication have made it possible to investigate these effects, which mainly occur at the nanoscale range.
Another class of S/F systems are electrically decoupled S/F layers, e.g by an insulating layer in between. In this case, the paramagnetic effect is prevented and the systems only interact via the orbital effect. In other words, superconductivity is only influenced by the magnetic stray field of the ferromagnet. So far, the focus of experimental investigations was primarily on the pinning properties of superconducting thin films with arrays of magnetic dots[42,43] and planar S/F bilayers[18,19,44–46]. In the latter case, superconductivity is influenced by the nonuniform magnetic field of the domain structure in the ferromagnet. In such a system, the conditions for the appearance of superconductivity are modified by the magnetic stray field of the domains which results in the formation of inhomogeneous superconducting states and an exotic dependence of the superconducting critical temperature T_c on the external magnetic field.[19,22,46–50]
A detailed introduction about the appearance of inhomogeneous states in S/F hybrids depending on temperature and external magnetic field will be given in the following section.

1.2 Inhomogeneous superconductivity

1.2.1 Introduction

In purely electromagnetically coupled planar S/F hybrids, superconductivity is affected only by the stray field of the ferromagnet $\boldsymbol{H}_{\mathrm{FM}}$. Bulk superconductivity is destroyed, if H_{FM} is larger than the upper critical field H_{c2} for a type-II superconductor. More precisely, in a planar thin film structure, it is the field component perpendicular to the surface which destroys superconductivity, because $H_{\mathrm{c2}}^{\perp}$ is usually much smaller than the parallel critical field $H_{\mathrm{c2}}^{||}$. This can bee seen by a simple estimate of the critical fields, $H_{\mathrm{c2}}^{\perp} \sim \Phi_0/\xi_{\mathrm{GL}}^2$ and $H_{\mathrm{c2}}^{||} \sim \Phi_0/(\xi_{\mathrm{GL}} D_s)$, where Φ_0 is the flux quantum and D_s the sample thickness. For $D_s \ll \xi_{\mathrm{GL}}$, $H_{\mathrm{c2}}^{\perp}$ is much smaller than $H_{\mathrm{c2}}^{||}$.[51] This is the case if D_s is small enough, or if the sample temperature T is close to the critical temperature T_c where ξ_{GL} diverges[†]. Therefore, only the out-of-plane component $H_{\mathrm{FM}}^{\perp}$ will be considered in the following discussion and $H_{\mathrm{c2}} = H_{\mathrm{c2}}^{\perp}$.
An external magnetic field $\boldsymbol{H}$ can be used to manipulate the effective field which suppresses superconductivity. If $\boldsymbol{H}$ is applied in the same direction as $\boldsymbol{H}_{\mathrm{FM}}^{\perp}$, superconductivity can be destroyed, if $|\boldsymbol{H}_{\mathrm{FM}}^{\perp} + \boldsymbol{H}| > H_{\mathrm{c2}}$ while superconductivity can be turned on, if $|\boldsymbol{H}_{\mathrm{FM}}^{\perp} - \boldsymbol{H}| < H_{\mathrm{c2}}$. If we assume a domain structure where the domains have an out-of-plane component with opposite sign, superconductivity is suppressed above the domains with parallel magnetization orientation (positive domains), while it is enhanced above domains with antiparallel magnetization orientation (negative domains). The state, when superconductivity is turned on in the negative domains

[†] $\xi_{\mathrm{GL}}(T) = \xi_{\mathrm{GL}}(T = 0\,K)/\sqrt{1 - T/T_c}$

by $\boldsymbol{H}$, is called reverse-domain superconductivity (RDS). The state when superconductivity survives above positive domains, is called parallel-domain superconductivity (PDS). RDS and PDS have been observed experimentally in transport measurements of Pb/$BaFe_{12}O_{19}$, Nb/$BaFe_{12}O_{19}$, and Al/$BaFe_{12}O_{19}$ hybrid structures.[20,45,52,53]

While RDS and PDS are inhomogeneous "bulk" states, another state of inhomogeneous superconductivity in S/F systems is localized above domain walls. This state of localized superconductivity has been theoretically investigated by Buzdin and Mel'nikov, which considered a step-like distribution of $H_{\mathrm{FM}}^{\perp}$.[21] They have demonstrated, that superconductivity will survive in the vicinity along the step, even if the amplitude $H_{\mathrm{FM}}^{\perp}$ is larger than H_{c2}. This state of localized superconductivity is called domain-wall superconductivity (DWS). The onset of DWS depending on H and $H_{\mathrm{FM}}^{\perp}$ has been estimated by Aladyshkin *et al.*.[47] First experimental fingerprints of DWS were found by transport measurements of a Nb thin film on top of a $BaFe_{12}O_{19}$ single crystal, separated by a thin insulating layer.[19] In the same samples, Fritzsche *et al.* visualized different states of inhomogeneous superconductivity by low-temperature scanning laser microscopy (LTSLM).[22] Details about the signal mechanism of LTSLM will be described later. While the regime of RDS and PDS was successfully visualized, no indication for DWS was found in these experiments. This was mainly attributed to the rather complex domain structure (bubble domains) of the $BaFe_{12}O_{19}$ single crystal.[19]

Similar to DWS, localized superconductivity can also appear at the surface of a superconductor in an external magnetic field. This state is called surface superconductivity (SuSc). It is well known, that so-called surface or bound states can be generated by the presence of boundaries in a material.[54,55] The formation of surface bound states for the superconducting order parameter was first considered by Saint-James and de Gennes.[56,57] They showed that localized superconductivity at a superconductor/vacuum or superconductor/insulator interface can nucleate in H larger than the upper critical field H_{c2} for bulk superconductivity. The upper critical field for SuSc is given by $H_{c3} \approx 1.7 H_{c2}$. Experimental evidence for SuSc has been found by dc transport[58–61] or inductive measurements[62] shortly after the theoretical prediction in 1963.[56] Later on, other methods such as ac-susceptibility and permeability measurements,[62–65] magnetization measurements,[66,67] surface impedance measurements[68] and tunneling spectroscopy[69] confirmed the existence of SuSc when $\boldsymbol{H}$ was applied parallel to the surface. While two different regions for bulk and SuSc were clearly observed for fields parallel to the surface, no signature for SuSc was observed when $\boldsymbol{H}$ was applied perpendicularly. The in-plane field dependence of the critical current $I_c(H)$ in the regime of SuSc for $\boldsymbol{H}$ parallel to the bias current was described by Abrikosov[70] and studied experimentally[71–73]. Park described theoretically the evolution of $I_c(H)$ in the state of SuSc when the in-plane field $\boldsymbol{H}$ is applied perpendicular to the bias current flow.[74] He predicted an asymmetry in the critical surface current, resulting from the superposition of surface screening currents and external currents. Such an asymmetry has not been observed experimentally yet.

Similarly to SuSc, localized superconductivity can also nucleate near the sample edge in a thin semi-infinite superconducting film, in a thin superconducting disk of very large diameter or around holes in a perpendicular magnetic field.[75–80] It should be

mentioned, that SuSc and localized states at the sample edges in perpendicular field (called edge superconductivity (ES)) are qualitatively and quantitatively the same. While SuSc has been investigated in several compounds like Pb-based alloys,[62,66,81] Nb and Nb-based alloys,[61,65,66,68] polycrystalline MgB_2,[82] Pb,[62,69,83] UPt_3 whiskers[84] and $NbSe_2$,[85] experimental studies on ES in thin film structures are rare[86,87]. Recently, the first real space observation of ES was obtained by scanning tunneling microscopy on Pb thin film islands[88].
Before we discuss the experimental results of the investigations on inhomogeneous superconducting states by LTSLM technique, the signal mechanism of LTSLM will be described in the following section.

1.2.2 Low-temperature scanning laser microscopy

Depending on the sample under investigation, various kinds of physical properties can be mapped with LTSLM.[24,89–91] For LTSLM, the sample is mounted on a cold finger of a Helium flow cryostat with an optical window which enables irradiation of the sample surface in the (x, y) plane by a focused laser beam with beam spot diameter $\sim 1.5 - 2\,\mu$m.[22,24,89] The amplitude modulated laser beam (at frequency $\sim 10\,$kHz) induces a local increase of temperature $\delta T(x - x_0, y - y_0)$, centered at the beam spot position (x_0, y_0) on the sample surface. During imaging, the bridge under investigation is biased at a constant current I and the beam-induced change of voltage $\Delta V(x_0, y_0)$ is recorded by lock-in technique. The LTSLM voltage signal of a superconducting sample can be interpreted in the following way: If the irradiated part of the sample is in the normal state with conductivity g_n, the laser beam induces a very small voltage signal $\Delta V \propto \partial g_n/\partial T$. However, if the irradiated region takes part in the transfer of a substantial part of the supercurrents, the beam-induced suppression of superconductivity might switch the sample from a low-resistive to a high-resistive state. This effect should be maximum, if I is close to the overall critical current $I_c = I_c(T, H)$ of the sample. In this case, LTSLM allows one to map out the ability of the sample to carry supercurrents, depending on T and $\boldsymbol{H}$.
In this thesis, LTSLM was used to visualize different states of inhomogeneous superconductivity in $Pb/BaFe_{12}O_{19}$ hybrids and in Nb bridges. The main results of the investigations are summarized in the following three sections, starting with the S/F hybrids.

1.2.3 Summary of pub. I: inhomogeneous superconducting states

The aim of our investigations of an electrically decoupled S/F hybrid was to visualize states of inhomogeneous superconductivity by means of LTSLM. The investigated S/F hybrid was composed of Pb on top of a ferromagnetic $BaFe_{12}O_{19}$ (BFO) single crystal, separated by a thin Ge layer. BFO single crystals have two main advantages: First, the domain structure is almost not affected by external fields in the used magnetic field range ($|\boldsymbol{H}| \sim 1200\,$Oe) and second, the domain structure as well as $H_{\mathrm{FM}}^{\perp}$ can be adjusted by the cutting angle with respect to the crystal axis. While the domain pattern of the BFO substrate was rather complex in the first experiments,[19]

recent progress in the preparation have made it possible to get well defined stripe-like domain patterns with a width of about $30\,\mu$m.[20] This allowed the patterning of microbridges with two particular orientations with respect to the domain walls. One bridge was oriented perpendicularly to the domain walls while the other bridge, investigated in publication II, was oriented parallel to the domains with exactly one domain wall underneath.
In publication I, we studied experimentally the effect of the stripe-like domain pattern of the BFO substrate on the magnetoresistance of a superconducting Pb microbridge which was oriented perpendicular to the domain walls. The sample was electrically characterized by variation of temperature T and external field H and an experimental $H-T$ phase diagram was composed out of the $R(H,T)$ measurements. The out-of-plane component of the stray field $H_{\mathrm{FM}}^{\perp}$ ($H_{\mathrm{FM}}^{\perp} \sim \pm 500\,\mathrm{Oe}$) leads to a splitting of the phase boundary for the Pb film above positive ($+H_{\mathrm{FM}}^{\perp}$) and negative domains ($-H_{\mathrm{FM}}^{\perp}$). The sample only shows zero resistance, when the regions of inhomogeneous superconductivity above positive and negative domains overlap in the $H-T$ plane. It is demonstrated that high T superconductivity appears in the form of reverse-domain superconductivity only above negative domains which have an out-of-plane magnetization opposite to the sign of H. By transport measurements, we experimentally determined the critical currents, corresponding to the suppression of inhomogeneous superconductivity above parallel and antiparallel magnetic domains in a broad T range. LTSLM made it possible to directly visualize the temperature- and field-induced transitions from complete superconductivity to RDS and PDS and from these inhomogeneous superconducting states to the normal state. We clearly observed the migration of the maximum of the beam-induced response along the bridge between the domains of different polarity upon sweeping H. While slight indications of edge superconductivity were found, no signature of DWS was observed.

1.2.4 Summary of pub. II: domain-wall superconductivity

This publication presents the visualization of non-uniform superconducting states in a Pb thin-film bridge with a single straight domain wall along the center of the bridge. In this sample, the state of DWS was successfully visualized for the first time. The evolution of the DWS state with decreasing T was mapped. Using H as a control parameter, it is demonstrated that superconductivity in a wide superconducting bridge can be switched from the DWS to RDS state. This opens up interesting perspectives for the creation of spatially non-uniform superconducting states and for their manipulation by external and internal magnetic fields.

1.2.5 Summary of pub. III: edge superconductivity

For the investigation of edge superconductivity (ES), two Nb microbridges have been studied in H, applied perpendicularly to the sample surface. As LTSLM has been successfully used to visualize inhomogeneous superconducting states in the Pb/BFO hybrids, the idea was to map the current distribution close to the transition from the superconducting to the normal state. In the study we compare microbridges

with and without microholes (antidots (ADs)).
The resistance R vs perpendicular external magnetic field H was measured for superconducting Nb thin–film microbridges with and without ADs. Well below the transition temperature, integral $R(H)$ measurements of the resistive transition to the normal state on the plain bridge show two distinct regions, which can be identified as bulk and edge superconductivity, respectively. The transition from bulk to ES, and finally to the full normal state, can be identified by a pronounced change in slope dR/dH, which however strongly depends on the applied bias current density. ES appears, when bulk superconductivity becomes suppressed at the upper critical field H_{c2} and below the critical field of edge superconductivity $H_{c3} \approx 1.7\,H_{c2}$. The presence of additional edges in the AD bridge leads to a different shape of the $R(H)$ curves. We used LTSLM to visualize the current distribution in the plain and AD bridge upon sweeping H. While the plain bridge shows a dominant LTSLM signal at its edges for $H > H_{c2}$ the AD bridge also gives a signal from the inner parts of the bridge due to the additional edge states around the ADs. LTSLM reveals an asymmetry in the current distribution between left and right edges, which confirms theoretical predictions by Park *et al.*.[74] The experimental results are in good agreement with our numerical simulations (based on the time-dependent Ginzburg–Landau model) yielding the spatial distribution of the order parameter and current density for different bias currents and H values.

1.3 Electrically coupled S/F oxide heterostructures

1.3.1 Introduction

In this paragraph we come back to S/F hybrids, now in direct electrical contact. In contrast to the previously described experiments on inhomogeneous superconducting states, we have been interested in the transport and interface properties of oxide heterostructures, composed of the unconventional high-T_c superconductor $YBa_2Cu_3O_7$ (YBCO) and the transition metal oxide $La_{0.7}Ca_{0.3}MnO_3$ (LCMO). Recent progress on the atomic scale growth, make it possible to combine different physical phenomena such as superconductivity and ferromagnetism in epitaxial heterostructures. In such S/F hybrids, superconducting correlations may be established in the ferromagnet due to the proximity effect, allowing superconductivity and ferromagnetism to coexist within a short distance from the interface of the order of the induced superconducting correlation length.[10,92,93] Simultaneously, the exchange field causes pair breaking in the superconductor, weakening or even suppressing the superconducting order parameter, and inducing a local magnetic moment in the superconductor at a distance from the S/F interface set by the superconducting coherence length. Magnetic ordering is generally more robust than superconductivity (the exchange energy in ferromagnets is typically $\sim 1\,\mathrm{eV}$, while the Cooper pair formation energy is $\sim 0.01\,\mathrm{eV}$), and for materials having a strong exchange field, magnetism may be unperturbed by the proximity of a superconductor. While S/F hybrid structures based on metallic ferromagnets and conventional superconductors have been investigated in detail,[10] there are much less studies on S/F systems involving high-T_c cuprate superconductors, characterized by a very short coherence

length and an anisotropic superconducting gap. In this context, half metallic rare earth manganites like LCMO are ideal ferromagnets, as they are nearly perfectly in-plane lattice matched with cuprates like YBCO, which enables heteroepitaxial growth of cuprate/manganite SF bilayers and superlattices with well defined interfaces.[94–96] YBCO/LCMO superlattices have allowed the study of novel phenomena, such as a long range proximity effect,[11,12] spin polarized quasiparticle injection into the superconducting layer within a spin diffusion length ξ_{FM},[13] giant magnetoresistance[97] and a giant modulation of the ferromagnetic layer magnetization induced by superconductivity[14].
Another issue which is investigated with increasing intensity, are physical properties of interfaces between complex oxides. In strongly correlated electron systems, interfacial properties can be crucial for the macroscopic behavior of the system and they can differ significantly from those of bulk materials. This allows the possibility to create new physical states which do not exist in bulk compounds. The most prominent example of unexpected interface effects is the system $LaAlO_3/SrTiO_3$.[6,7] Though both materials are insulators, a quasi-two dimensional electron gas is formed at the interface which even becomes superconducting. Since YBCO/LCMO heterostructures with well-defined interfaces can be grown, it is a perfect system for the investigation of the interface properties of an S/F system based on oxide materials. Recently, interfacial properties in YBCO/LCMO superlattices were investigated by x-ray magnetic circular dichroism (XMCD)†.[8,9] The studies revealed an induced ferromagnetic moment on the interfacial Cu, oriented antiparallel to the adjacent Mn, whose temperature dependence follows that of the Mn moment. The authors suggest that Cu and Mn are coupled across the interface by covalent chemical bonding that results in strong hybridization and large rearrangements of the orbital occupancies ("orbital reconstruction"). Within this context, the Mn-O-Cu superexchange interaction explains the induced magnetic moment in the cuprate and the presence of a non-superconducting YBCO layer at the interface.
In our investigation of YBCO/LCMO bilayers, we have focused on transport properties as well as on interface properties studied by spectroscopic techniques such as XMCD. The results are summarized in the following publication.

1.3.2 Summary of pub. IV: YBCO/LCMO bilayers

In publication IV, we present a detailed investigation of YBCO/LCMO bilayers, focusing on the transport properties depending on the YBCO layer thickness as well as on interface properties on the atomic length scale. In order to study the influence of the injection of spin-polarized particles, we prepared bilayers with different YBCO layer thickness d_Y, ranging from $5 - 50\,\mathrm{nm}$ with a constant LCMO layer thickness of 50 nm on top. To extract the influence of the LCMO layer, we fabricated YBCO single layers with the same thicknesses. Transport measurements indicate high-quality bilayers, showing a reduction in the superconducting transition temperature T_c only below $d_Y \approx 10$ unit cells. We found, that in our samples, the suppression of

†XMCD is an experimental technique, which reveals the element-specific magnetization.[98] When a magnetic atom is irradiated by circular polarized light, the absorption spectra depends on the helicity of the light. The difference of the absorption spectra is the XMCD signal.

T_c by the injection of spin-polarized particles is much less than observed in previous experiments.[13] This leads to a smaller spin-diffusion length. The observation can be explained by the stronger interaction between Mn and Cu moments at the interface, which we observed by XMCD measurements. Our XMCD data clearly confirm the phenomenon of magnetic moments being induced on Cu atoms at the LCMO/YBCO interface, with an even stronger interaction than found in the original report of Chakhalian *et al.*.[8] Dichroism measurements with linearly polarized light, which give information about the orbital occupancy, show no evidence of any significant difference between the orbital occupations in the interfacial Cu as compared to the Cu in bulk YBCO. This implies, that an induced magnetic moment on Cu through hybridization at the interface with Mn can result without any accompanying "orbital reconstruction", as found by Chakhalian *et al.*.[9]

Chapter 2

Magnetic tunnel junctions

This chapter presents studies on magnetic tunnel junctions, obtained in the framework of this thesis. The first part will briefly introduce the field of magnetic tunnel junctions, and the actual challenges which need to be solved for further improvements will be mentioned. The main experimental results on this topic are summarized in the second part.

2.1 Introduction

For a long time, charge and spin of the electron were only considered separately. While charges were controlled by electric fields, the electron spin was used only indirectly via the resulting magnetization in ferromagnets, e.g. to store information. This situation changed with the discovery of the giant magnetoresistance (GMR) effect which allows the control of the charge transport through magnetization.[99,100] This pioneering work of the groups around Fert and Grünberg was honored by the Nobel Prize in Physics in 2007.[101] The discovery of the GMR effect was the beginning of a new field in physics, nowadays called spintronics, where charge and spin of the electron are considered simultaneously.[102] Magnetoresistive effects have been investigated intensively in the following years and only a few years after its discovery, the GMR effect was already used in read heads of hard disc drives which lead to an increase of the storage density of about three orders of magnitude. The ever increasing need for higher storage density of hard disc drives could be fulfilled by further progress in micropatterning which led to smaller device sizes and by the use of larger and more sensitive magnetoresistive effects. Nowadays, the industrial standard of read heads in hard disc drives is based on magnetic tunnel junctions (MTJs).[103] Although they are already used in various applications, there are still many open issues which need to be solved to exploit the full potential of MTJs.
MTJs consist of two ferromagnetic layers separated by a thin insulating tunneling barrier. The resistance of such a device depends on the relative magnetization orientation of the electrodes. This results from the difference in the density of states at the Fermi-level $N(E_F)$ for spin-up $N_\uparrow(E_F)$ and spin-down $N_\downarrow(E_F)$ electrons in a ferromagnetic material which leads to subbands for spin-up and spin-down electrons. When the electron conserves its spin, it can only tunnel into the subband with the same spin orientation. In an elastic tunneling process, the tunneling probability

is proportional to the number of occupied states on one side and the number of unoccupied states on the other side for the same spin orientation and energy (Fermi´s golden rule). The total conductivity of the MTJ can be explained in the two channel model. In the parallel magnetization orientation of the electrodes, the number of occupied and unoccupied states is large for one spin orientation while it is small for the other spin orientation. This leads to a high and low conductivity in the two channels, respectively. In the antiparallel state, the number of occupied states for one spin orientation is high on one side while the number of unoccupied states for the same spin orientation is low on the other side and vice versa for the other spin orientation. This yields a higher total conductivity for the parallel state as compared to the antiparallel state.

The first spin-dependent tunneling experiments were made by Meservey and Tedrow with superconductor/insulator/ferromagnet junctions.[104] They showed that the spin-polarization of the electron is conserved in the tunneling process. The tunneling spectra allows to calculate the spin polarization of the ferromagnet, defined as $P = \frac{N\uparrow(E_F)-N\downarrow(E_F)}{N\uparrow(E_F)+N\downarrow(E_F)}$. Motivated by this results, Jullière investigated Fe/Ge/Co junctions where he observed a difference in the conductance for parallel and antiparallel magnetization orientation of the electrodes.[15] With the assumption that the spin polarization is conserved during the tunneling process, Jullière relates the relative change in conductance to the spin polarization P_1 and P_2 directly at the interface of the two ferromagnetic electrodes. According to the Jullière model, the tunnel magneto resistance (TMR) is defined as $\mathrm{TMR} = 2\mathrm{P_1P_2}/(1 - \mathrm{P_1P_2}) = (\mathrm{R_{ap}} - \mathrm{R_p})/\mathrm{R_{ap}}$. R_{ap} and R_p is the resistance in the antiparallel and parallel state, respectively. The Jullière model is a phenomenological model and far too simple to describe the entire properties of MTJs satisfyingly, but it captures all essentials of the tunneling process. The model was further improved by Slonczewski who also took the height and the thickness of the tunneling barrier into account.[105]

The intensity of the research in the field of MTJs was rather low in the years after the discovery of the TMR effect. This was mainly due to low reproducibility in fabricating working junctions and the effect was too low for technological applications. Only the discovery of the GMR effect in the groups of Grünberg and Fert has fuelled the renewed interest on MTJs.[99,100,106] This was because the potential of spintronic based devices, which not only explore the charge but also the spin of the electron, was considered as huge. Similar to a MTJ, a GMR element is based on two ferromagnetic layers separated by a nonmagnetic metal instead of an insulating barrier.

The breakthrough of MTJs regarding reproducibility and higher TMR ratios was accomplished by Moodera *et al.* and Miyazaki *et al.*[107,108] They used amorphous Al_2O_3 as a tunneling barrier and achieved a TMR ratio of $\sim 10\,\%$ at room temperature which increased up to $\sim 70\,\%$ in the following years.[109] This improvement in device operation and reproducibility can be mainly attributed to the fabrication of well-controlled, uniform tunneling barriers of Al_2O_3 by evaporating and oxidizing a thin amorphous Al layer. Nowadays, the highest TMR ratios of about $\sim 500\,\%$ at room temperatures are reached by using (001)-oriented single crystal MgO tunneling barriers.[110–112] Theoretical calculations even predict higher TMR ratios of more than $1000\,\%$ at room temperature for MgO based MTJs. This is due to the elec-

tronic band structure of MgO ("spin-filtering effect").[113,114] According to the Jullière model, an infinite TMR ratio is expected for ferromagnets with a spin polarization of 100 %. Half-metallic oxides like Fe_3O_4,[115] CrO_2,[116] Heusler alloys[117] or doped manganites $La_xA_{1-x}MnO_3$ (A = Ca, Sr, Ba)[118] are believed to be 100 % spin polarized well below the Curie-temperature (T_C) and are therefore the most promising candidates for huge TMR ratios. Among the doped manganites, especially the compound $La_{0.65}Sr_{0.35}MnO_3$ is intensively studied because of its high T_C of about 360 K. Therefore it is a promising candidate for room temperature applications.

2.2 Magnetoresistance of LSMO based MTJs

2.2.1 Introduction

Due to a spin polarization of about 100 %, $La_{0.65}Sr_{0.35}MnO_3$ (LSMO) is a promising candidate for huge TMR ratios which should be even infinite according to the Jullière model. However, the first experimental results on LSMO based MTJs have been disillusioning. TMR ratios even at low temperatures were low ($\sim$ 100 %) and difficult to reproduce. In the following years, the TMR ratio could be continuously increased up to 1800 % at 4.2 K for LSMO electrodes separated by a $SrTiO_3$ (STO) tunneling barrier.[119] This was the highest TMR ratio for any kind of MTJ reported so far. Assuming identical interfaces, this results in a spin polarization of $P \sim 95$ %. Unfortunately, this high TMR ratio was only found in one junction and the shape of the resistance versus field measurements was very uncommon and not reproducible. The main problem of LSMO based junctions is the fast decay of the TMR ratio with increasing temperature and the disappearance well below T_C. It is known, that ferromagnetic correlations at manganite surfaces and interfaces are weaker than in bulk, causing a "dead layer".[120–122] For example, at the vacuum/LSMO interface the non-ferromagnetic layer is about 3 unit cells thick at 200 K , well below bulk T_C.[123] It has been shown, that a robust ferromagnetism can be realized even at room temperature by changing the doping profile at the interface ("interface engineering").[16,17] Therefore, investigations and improvements in the interfacial spin polarization might be the key for a further increase of the TMR ratio and an improved temperature dependence. This could help to exploit the full potential of LSMO based MTJs at room temperature.

In this work, we report on the TMR effect in LSMO based tunnel junctions grown by molecular-beam epitaxy (MBE). MBE is the growth technique with the highest growth control on the atomic scale. It further allows to adjust the doping level at any time during the growth process.[124] This makes MBE the most suitable technique to realize interface engineering, which was proposed to increase the spin-polarization at the interface.[16,17] Before one can start with investigations on interface engineering, reproducible junctions have to be fabricated and other effects like surface roughness or the quality of the tunneling barrier, which also lead to a fast decay of the TMR, have to be improved.[120,125–127]

The following publication presents the electrical characterization of a LSMO based MTJ grown by MBE engineered interfaces.

2.2.2 Summary of pub. V: TMR in LSMO based MTJ

Vertical mesa MTJs were patterned in several steps by photolithography and Ar-ion milling. The patterning process of the investigated MTJs is described in detail in the supplement of this publication. The investigated MTJ was grown on top of an antiferromagnetic $La_{0.35}Sr_{0.65}MnO_3$ (AF-LSMO) layer. This was necessary to increase the coercive field of the bottom electrode based on the "exchange bias" effect.[128] Without this AF-LSMO layer, the coercive field was almost the same for both electrodes and the field window for a high TMR ratio was extremely small. A detailed study on the influence of the exchange bias on the coercive field, depending on layer thickness and doping level of the antiferromagnetic layer has been made and will be published in the near future.
The investigated MTJ shows a large field window of extremely high TMR at low temperature. The TMR reaches $\sim 1900\,\%$ at 4 K. Assuming identical interfaces, this corresponds to an interfacial spin polarization higher than 95 %. This is the largest TMR ratio for any MTJ reported in the literature so far. The TMR decays quickly with increasing temperature and vanished around ~ 280 K, which is close to the temperature where the exchange bias effect disappears. Scanning the in-plane applied field orientation through 360°, the TMR shows 4-fold symmetry, i.e. biaxial anisotropy, aligned with the crystalline axes but not with the junction geometrical long axis. This indicates that an uniaxial anisotropy is not necessarily required to stabilize well-defined antiparallel states and high TMR ratios, as proposed by Bowen *et al.* and Jo *et al.*.[119,126]
The first measurements on MBE grown MTJs already showed an improvement in the TMR ratio compared to previous manganite based tunnel junctions. This can be mainly attributed to the high crystal and interface quality of the samples. The group of B. A. Davidson, which has grown the samples, has already verified by spectroscopic measurements, that they can enforce the interface ferromagnetism by changing the doping profile at the interface. Therefore, further improvement in the TMR ratio as well as in the temperature dependence can be expected in future devices.

2.3 Visualization of local properties in a MTJ

2.3.1 Introduction

This section presents investigations on a MTJ by low-temperature scanning laser microscopy (LTSLM) with the aim to correlate local properties with integral magnetotransport measurements. While TMR properties of MTJs have been investigated in detail in various material systems,[129,130] not much is known about the impact of their magnetic microstructure on the integral TMR properties. However, both in view of applications and from a fundamental point of view, it is of high interest to identify the spatial dependence of TMR on the magnetic properties of the electrodes. Nucleation and growth of magnetic domains in ferromagnets has been the focus of many efforts using various imaging techniques.[131–136] LTSLM has already been used to visualize locally different resistive states in a quasi-1-dimensional

$La_{0.67}Ca_{0.33}MnO_3$ thin film grain boundary junction. It has been shown that the obtained LTSLM signal is directly proportional to the local TMR ratio.[24] These results suggest that LTSLM could also be useful to investigate TMR in vertical MTJs under typical bias conditions.
The signal mechanism of LTSLM in terms of MTJs differs from the mechanism in superconducting samples (cf. 1.2.2) and will be shortly described in the following. The amplitude modulated laser beam is scanned across the sample which locally heats the sample in vicinity of the beam spot position (x_0, y_0). In the case of LSMO, the penetration depth of light with $\lambda = 680\,\mathrm{nm}$ is $\sim 65\,\mathrm{nm}$.[137] Therefore the heating occurs throughout the entire thickness of the LSMO/STO/LSMO stack. This induces a change in the local tunneling conductivity $g(x, y)$ and in turn a change in the global conductance. This change in conductance leads to a laser induced voltage drop $\Delta V(x_0,\ y_0) \propto dg/dT(x_0, y_0)$ which is recorded by lock-in technique. Therefore, if $dg/dT(x, y)$ depends on the magnetization orientation of the electrodes, the voltage image ΔV will give information on the local properties of the sample.

2.3.2 Summary of pub. VI: local TMR probed by LTSLM

This publication reports on LTSLM imaging of local resistive states in a vertical LSMO/STO/LSMO MTJ upon variation of direction and amplitude of the external in-plane magnetic field. The electric properties of the investigated sample are presented in publication V. The investigation of the MTJ by LTSLM was possible due to the difference in $dg/dT(\Theta)$, with Θ being the relative angle between the magnetization orientation of the electrodes. In a quantitative analysis, we have calculated from the voltage images the convolution[1] of $\cos\{\Theta(x_0, y_0)\}$ with the beam induced temperature profile δT, for different values of amplitude and direction of applied magnetic field. By assuming that the domain size is larger than the temperature profile, the convolution $\langle\cos\{\Theta(x_0, y_0)\}\rangle = \cos\{\Theta(x_0, y_0)\}$ and we can get the distribution of the relative magnetization orientation $\Theta(x, y)$ from the voltage images. With $\Theta(x, y)$ we can calculate the global resistance for each image, yielding quantitative agreement with the integral $R(H)$ measurements. A detailed description of the calculation can be found in the supplement of this publication. By means of LTSLM, it is possible to visualize magnetic domain nucleation and propagation during magnetic field sweeps. It is found that the domain walls are predominantly oriented along the crystalline *a*- and *b*-axes of LSMO. The results show that LTSLM can be used to link the magnetic microstructure to the integral magnetotransport and thus provides a valuable tool for further investigations of MTJs.
It should be mentioned, that there are various other techniques to visualize the domain structure in ferromagnets. This can be divided into two classes, depending on the interaction between probe and sample.[131–136] Techniques like magnetic force or Lorentz microscopy are using the stray fields while in magneto-optical Kerr or spin-dependent tunneling microscopy, the magnetization is used to map out the domain structure. None of this techniques is able to measure locally the relative magnetization orientation Θ in real-life operating conditions (i.e., with applied voltages and

[1] $\langle\cos\{\Theta(x_0, y_0)\}\rangle = \frac{1}{\Delta T A_s}\int_{A_J}\cos\{\Theta(x, y)\}\delta T(x - x_0, y - y_0)dxdy$ with A_s is the approximate size of the area warmed up by the laser and ΔT is the maximal induced increase in temperature.

in large magnetic fields) in MTJs as shown in publication VI. Therefore the investigation of MTJs by means of LTSLM gives additional information not attainable by any other imaging technique so far.

Bibliography

[1] Yoshinori Tokura and Harold Y. Hwang. Condensed-Matter Physics: Complex Oxides on Fire. *Nature Mater.*, 7:694, 2008.

[2] Sang-Wook Cheong. Transition metal oxides: The exciting world of orbitals. *Nature Mater.*, 6:927, 2007.

[3] S.-W. Cheong and M. Mostovoy. Multiferroics: a magnetic twist for ferroelectricity. *Nature Mater.*, 6:13, 2007.

[4] Y. Tokura and N. Nagaosa. Orbital Physics in Transition-Metal Oxides. *Science*, 288:462, 2000.

[5] Jacobo Santamaría. Interfaces on stage. *Nature Mater.*, 2:229, 2008.

[6] A. Ohtomo and H. Y. Hwang. A high-mobility electron gas at the $LaAlO_3/SrTiO_3$ heterointerface. *Nature*, 427:423, 2004.

[7] S. Thiel, G. Hammerl, A. Schmehl, C. W. Schneider, and J. Mannhart. Tunable Quasi-Two-Dimensional Electron Gases in Oxide Heterostructures. *Science*, 313:1942, 2006.

[8] J. Chakhalian, J. W. Freeland, G. Srajer, J. Strempfer, G. Khaliullin, J. C. Cezar, T. Charlton, R. Dalgliesh, C. Bernhard, G. Cristiani, H.-U. Habermeier, and B. Keimer. Magnetism at the Interface between Ferromagnetic and Superconducting Oxides. *Nature Phys.*, 2:244, 2006.

[9] J. Chakhalian, J. W. Freeland, H.-U. Habermeier, G. Cristiani, G. Khaliullin, M. van Veenendaal, and B. Keimer. Orbital Reconstruction and Covalent Bonding at an Oxide Interface . *Science*, 318:1114, 2007.

[10] A. I. Buzdin. Proximity Effects in Superconductor-Ferromagnet Heterostructures. *Rev. Mod. Phys.*, 77:935, 2005.

[11] Z. Sefrioui, D. Arias, V. Peña, J. E. Villegas, M. Varela, P. Prieto, C. León, J. L. Martinez, and J. Santamaria. Ferromagnetic/Superconducting Proximity Effect in $La_{0.7}Ca_{0.3}MnO_3/YBa_2Cu_3O_{7-\delta}$ Superlattices. *Phys. Rev. B*, 67:214511, 2003.

[12] V. Peña, Z. Sefrioui, D. Arias, C. Leon, and J. Santamaria. Coupling of superconductors through a half-metallic ferromagnet: Evidence for a long-range proximity effect. *Phys. Rev. B*, 69:224502, 2004.

[13] S. Soltan, J. Albrecht, and H.-U. Habermeier. Ferromagnetic/superconducting bilayer structure: A model system for spin diffusion length estimation. *Phys. Rev. B*, 70:144517, 2004.

[14] J. Hoppler, J. Stahn, Ch. Niedermayer, V. K. Malik, H. Bouyanfif, A. J. Drew, M. Rössle, A. Buzdin, G. Cristiani, H.-U. Habermeier, B. Keimer, and C. Bernhard. Giant Superconductivity-Induced Modulation of the Ferromagnetic Magnetization in a Cuprate–Manganite Superlattice. *Nature Mater.*, 8:315, 2009.

[15] M. Julliere. Tunneling between ferromagnetic films. *Phys. Lett. A*, 54:225, 1975.

[16] H. Yamada, Y. Ogawa, Y. Ishii, H. Sato, M. Kawasaki, H. Akoh, and Y. Tokura. Engineered Interface of Magnetic Oxides. *Science*, 305:646, 2004.

[17] J. J. Kavich, M. P. Warusawithana, J. W. Freeland, P. Ryan, X. Zhai, R. H. Kodama, and J. N. Eckstein. Nanoscale suppression of magnetization at atomically assembled manganite interfaces: XMCD and XRMS measurements. *Phys. Rev. B*, 76:014410, 2007.

[18] W. Gillijns, A. Yu. Aladyshkin, A. V. Silhanek, and V. V. Moshchalkov. Magnetic confinement of the superconducting condensate in superconductor-ferromagnet hybrid composites. *Phys. Rev. B*, 76:060503(R), 2007.

[19] Z. R. Yang, M. Lange, A. Volodin, R. Szymczak, and V. V. Moshchalkov. Domain-Wall Superconductivity in Superconductor-Ferromagnet Hybrids. *Nature Mater.*, 3:793, 2004.

[20] J. Fritzsche, R. B. G. Kramer, and V. V. Moshchalkov. Highly transparent superconducting-normal junctions induced by local fields of magnetic domains in a homogeneous superconductor. *Phys. Rev. B*, 80:094514, 2009.

[21] A. I. Buzdin and A. S. Mel'nikov. Domain Wall Superconductivity in Ferromagnetic Superconductors. *Phys. Rev. B*, 67:020503(R), 2003.

[22] J. Fritzsche, V. V. Moshchalkov, H. Eitel, D. Koelle, R. Kleiner, and R. Szymczak. Local Observation of Reverse-Domain Superconductivity in a Superconductor-Ferromagnet Hybrid. *Phys. Rev. Lett.*, 96:247003, 2006.

[23] R. Gross and D. Koelle. Low Temperature Scanning Electron Microscopy of Superconducting Thin Films and Josephson Junctions. *Rep. Prog. Phys.*, 57:651, 1994.

[24] M. Wagenknecht, H. Eitel, T. Nachtrab, J. B. Philipp, R. Gross, R. Kleiner, and D. Koelle. Laser Microscopy of Tunneling Magnetoresistance in Manganite Grain-Boundary Junctions. *Phys. Rev. Lett.*, 96:047203, 2006.

[25] Stephen Blundell. *Magnetism in Condensed Matter*. Oxford University Press, 2001.

[26] V. L. Ginzburg. *J. Exp. Theor. Phys.*, 4:153, 1956.

[27] B. T. Matthias, H. Suhl, and E. Corenzwit. Ferromagnetic Superconductors. *Phys. Rev. Lett.*, 1:449, 1958.

[28] P. W. Anderson and H. Suhl. Spin Alignment in the Superconducting State. *Phys. Rev.*, 116:898, 1959.

[29] S. K. Sinha, G. W. Crabtree, D. G. Hinks, and H. Mook. Study of Coexistence of Ferromagnetism and Superconductivity in Single-Crystal $ErRh_4B_4$. *Phys. Rev. Lett*, 48:950, 1982.

[30] A. I. Larkin and Yu. N. Ovchinnikov. Inhomogeneous state of superconductors. *Zh. Eksp. Teor. Fiz.*, 47:1136, 1964.

[31] Peter Fulde and Richard A. Ferrell. Superconductivity in a Strong Spin-Exchange Field. *Phys. Rev.*, 135:A550, 1964.

[32] E. A. Demler, G. B. Arnold, and M. R. Beasley. Superconducting proximity effects in magnetic metals. *Phys. Rev. B*, 55:15174, 1997.

[33] S. S. Saxena, P. Agarwal, K. Ahilan, F. M. Grosche, R. K. W. Haselwimmer, M. J. Steiner, E. Pugh, I. R. Walker, S. R. Julian, P. Monthoux, G. G. Lonzarich, A. Huxley, I. Sheikin, D. Braithwaite, and J. Flouquet. Superconductivity on the border of itinerant-electron ferromagnetism in UGe_2. *Nature*, 406:587, 2000.

[34] Dai Aoki, Andrew Huxley, Eric Ressouche, Daniel Braithwaite, Jacques Flouquet, Jean-Pascal Brison, Elsa Lhotel, and Carley Paulsen. Coexistence of superconductivity and ferromagnetism in URhGe. *Nature*, 413:613, 2001.

[35] A. Levy Yeyati F. S. Bergeret and A. Martín-Rodero. Inverse proximity effect in superconductor-ferromagnet structures: From the ballistic to the diffusive limit. *Phys. Rev. B*, 72:064524, 2005.

[36] V.V. Ryazanov, V. A. Oboznov, A.Yu. Rusanov, A.V. Veretennikov, A. A. Golubov, and J. Aarts. Coupling of Two Superconductors through a Ferromagnet: Evidence for a π Junction˙ *Phys. Rev. Lett.*, 86:2427, 2001.

[37] F. S. Bergeret, A. F. Volkov, and K. B. Efetov. Long-Range Proximity Effects in Superconductor-Ferromagnet Structures. *Phys. Rev. Lett.*, 86:4096, 2001.

[38] R. S. Keizer, S. T. B. Goennenwein, T. M. Klapwijk, G. Miao, G. Xiao, and A. Gupta. A spin triplet supercurrent through the half-metallic ferromagnet CrO_2. *Nature*, 439:825, 2006.

[39] L. R. Tagirov. Low-Field Superconducting Spin Switch Based on a Superconductor/Ferromagnet Multilayers. *Phys. Rev. Lett.*, 83:2058, 1999.

[40] J.Y. Gu, C.-Y. You, J. S. Jiang, J. Pearson, Ya. B. Bazaliy, and S. D. Bader. Magnetization-Orientation Dependence of the Superconducting Transition Temperature in the Ferromagnet-Superconductor-Ferromagnet System: CuNi/Nb/CuNi. *Phys. Rev. Lett.*, 89:267001, 2002.

[41] F. S. Bergeret, A. F. Volkov, and K. B. Efetov. Odd triplet superconductivity and related phenomena in superconductor-ferromagnet structures. *Rev. Mod. Phys.*, 77:1321, 2005.

[42] Y. Otani, B. Pannetier, J.P. Nozièresc, and D. Givordc. Magnetostatic interactions between magnetic arrays and superconducting thin films. *J. Magn. Magn. Mater.*, 126:622, 1993.

[43] O. Geoffroya, D. Givord, Y. Otania, B. Pannetier, and F. Ossart. Magnetic and transport properties of ferromagnetic particulate arrays fabricated on superconducting thin films. *J. Magn. Magn. Mater.*, 121:223, 1993.

[44] Z. Yang, K. Vervaeke, and V. V. Moshchalkov. Modulation of superconductivity by a magnetic template in $Nb/BaFe_{12}O_{19}$ hybrids. *Phys. Rev. B*, 73:224509, 2006.

[45] Z. Yang, J. V. de Vondel, W. Gillijns, W. Vinckx, V. V. Moshchalkov, and R. Szymczak. Effect of reversed magnetic domains on superconductivity in $Pb/BaFe_{12}O_{19}$ hybrids . *Appl. Phys. Lett.*, 88:232505, 2006.

[46] W. Gillijns, A. Yu. Aladyshkin, M. Lange, M. J. Van Bael, and V. V. Moshchalkov. Domain-Wall Guided Nucleation of Superconductivity in Hybrid Ferromagnet-Superconductor-Ferromagnet Layered Structures. *Phys. Rev. Lett.*, 95:227003, 2005.

[47] A. Yu. Aladyshkin, A. I. Buzdin, A. A. Fraerman, A. S. Mel'nikov, D. A. Ryzhov, and A. V. Sokolov. Domain-Wall Superconductivity in Hybrid Superconductor-Ferromagnet Structures. *Phys. Rev. B*, 68:184508, 2003.

[48] Martin Lange, Margriet J. Van Bael, Yvan Bruynseraede, and Victor V. Moshchalkov. Nanoengineered Magnetic-Field-Induced Superconductivity. *Phys. Rev. Lett.*, 90:197006, 2003.

[49] I. F. Lyuksyutov and V. L. Pokrovsky. Ferromagnet-Superconductor Hybrids. *Adv. Phys.*, 54:67, 2005.

[50] A. Yu. Aladyshkin, A. V. Silhanek, W. Gillijns, and V. V. Moshchalkov. Nucleation of Superconductivity and Vortex Matter in Superconductor-Ferromagnet Hybrids. *Supercond. Sci. Technol.*, 22:053001, 2009.

[51] M. Tinkham. *Introduction to superconductivity.* McGraw-Hill Inc., second edition, 1996.

[52] Zhaorong Yang, Joris Van de Vondel, Werner Gillijns, Wim Vinckx, Victor V. Moshchalkov, and Ritta Szymczak. Effect of reversed magnetic domains on superconductivity in Pb/$BaFe_{12}O_{19}$ hybrids. *Appl. Phys. Lett.*, 88:232505, 2006.

[53] A. Yu. Aladyshkin, J. Fritzsche, and V. V. Moshchalkov. Planar superconductor/ferromagnet hybrids: Anisotropy of resistivity induced by magnetic templates. *Appl. Phys. Lett.*, 94:222503, 2009.

[54] I. Tamm. *Physik. Zeits. Sowjetunion*, 1:733, 1932.

[55] W. Shockley. On the Surface States Associated with a Periodic Potential. *Phys. Rev*, 56:317, 1939.

[56] D. Saint-James and P. G. de Gennes. Onset of superconductivity in decreasing fields. *Phys. Lett.*, 7:306, 1963.

[57] D. Saint-James, G. Sarma, and E. J. Thomas. *Type–II superconductivity.* Pergamon Press, 1969.

[58] C. F. Hempstead and Y. B. Kim. Resistive transitions and surface effects in type-II superconductors. *Phys. Rev. Lett.*, 12:145, 1963.

[59] Frank T. J. Smith and Harry C. Gatos. Surface Superconductivity in Tantalum . *J. Appl. Phys.*, 39:3793, 1968.

[60] A. Rothwarf, J. I. Gittleman, and Bruce Rosenblum. Surface impedance in the surface superconducting state. *Phys. Rev.*, 155:370, 1967.

[61] J. Kirschenbaum. Superconducting critical fields in niobium and niobium containing oxygen. *Phys. Rev. B*, 12:3690, 1975.

[62] M. Strongin, A. Paskin, D. G. Schweitzer, O. F. Kammerer, and P. P. Craig. Surface superconductivity in Type I and type II superconductors. *Phys. Rev. Lett.*, 12:442, 1964.

[63] Francisco de la Cruz, M. David Maloney, and Manuel Cardona. Variation of the Ratio H_{c3}/H_{c2} in the Immediate Vicinity of T_c. *Phys. Rev.*, 187:766, 1969.

[64] R. W. Rollins, R. L. Cappelletti, and J. H. Fearday. Anomalous H_{c3}/H_{c2} near T_c in Pb-In and Critical Phenomena in the Superconducting Sheath. *Phys. Rev. B*, 2:105, 1970.

[65] J. R. Hopkins and D. K. Finnemore. Surface superconductivity in niobium and niobium-tantalum alloys. *Phys. Rev. B*, 9:108, 1974.

[66] D. G. Schweitzer and B. Bertman. Experimental Evidence for a Surface Mechanism for Hysteresis in Low-κ Type-II Superconductors. *Phys. Rev.*, 152:293, 1966.

[67] J. P. McEvoy, D. P. Jones, and J. G. Park. Nucleation of Superconductivity in Tantalum in a Decreasing Magnetic Field. *Phys. Rev. Lett.*, 22:229, 1969.

[68] Y. Brunet, P. Monceau, and G. Waysand. Dynamical properties of type-II superconductors: An experimental study. *Phys. Rev. B*, 10:1927, 1974.

[69] M. Strongin, A. Paskin, O. F. Kammerer, and M. Garber. Superconducting Tunneling at High Magnetic Fields and Possible Evidence for Ginzburg Surface Superconductivity. *Phys. Rev. Lett.*, 10:362, 1965.

[70] A. A. Abrikosov. Concerning surface superconductivity in strong magnetic fields. *Soviet Phys. JETP*, 20:480, 1965.

[71] R. V. Bellau. Influence of surface condition on the critical currents above H_{c2} in a superconducting Tantalum-Niobium alloy. *Physics Letter*, 21:13, 1966.

[72] R. V. Bellau. Critical surface currents and the angular dependence of the surface critical field of a type I1 superconductor. *Proc. Phys. Soc.*, 91:144, 1967.

[73] J. Lowell. Contribution of the surface to the current-carrying capacity of type I1 superconductors in the mixed state. *J. Phys. C: Solid State Phys.*, 2:372, 1969.

[74] J. G. Park. Asymmetry in the critical surface current of type-2 superconductors. *Phys. Rev. Lett.*, 15:352, 1965.

[75] R. H. White. Fluxoid Quantization and Critical Fields in Small Superconducting Samples. *Phys. Rev.*, 142:241, 1966.

[76] A. Bezryadin and B. Pannetier. Nucleation of Superconductivity in a Thin Film with a Lattice of Circular Holes. *J. Low Temp. Phys.*, 98:251, 1995.

[77] A. Bezryadin and B. Pannetier. Edge Superconducting States. *Physica Scripta*, T66:225, 1996.

[78] J. Berger and J. Rubinstein. *Connectivity and Superconductivity.* Springer Verlag, 2000.

[79] L. F. Chibotaru, A. Ceulemans, M. Morelle, G. Teniers, C. Carballeira, and V. V. Moshchalkov. Ginzburg landau description of confinement and quantization effects in mesoscopic superconductors. *J. Math. Phys.*, 46:095108, 2005.

[80] A. Yu. Aladyshkin, D. A. Ryzhov, A. V. Samokhvalov, D. A. Savinov, A. S. Mel'nikov, and V. V. Moshchalkov. Localized superconductivity and Little-Parks effect in superconductor/ferromagnet hybrids. *Phys. Rev. B*, 75:184519, 2007.

[81] J. Kirschenbaum and Y.-H. Kao. Temperature Dependence of the Surface-Sheath Nucleation Field in Strong-Coupling Superconductors. *Phys. Rev. Lett.*, 22:1177, 1969.

[82] M. I. Tsindlekht, G. I. Leviev, V. M. Genkin, I.Felner, P. Mikheenko, and J. Stuart Abell. Surface superconducting states in a polycrystalline MgB_2 sample. *Phys. Rev. B*, 74:132506, 2006.

[83] G. Fischer. Surface Nucleation Field H_{c3} of Pure Lead. *Phys. Rev. Lett.*, 20:268, 1968.

[84] N. Keller, J. L. Tholence, A. Huxley, and J. Flouquet. Surface superconductivity in the heavy-fermion superconductor UPt_3. *Phys. Rev. B*, 54:13188, 1996.

[85] G. D'Anna, P. L. Gammel, A. P. Ramirez, U. Yaron, C. S. Oglesby, E. Bucher, and D. J. Bishop. Evidence of surface superconductivity in 2H-$NbSe_2$ single crystals. *Phys. Rev. B*, 54:6583, 1996.

[86] D. Stamopoulos, M. Pissas, V. Karanasos, D. Niarchos, and I. Panagiotopoulos. Influence of randomly distributed magnetic nanoparticles on surface superconductivity in Nb films. *Phys. Rev. B*, 70:054512, 2004.

[87] J. Scola, A. Pautrat, C. Goupil, L. Méchin, V. Hardy, and Ch. Simon. Voltage noise and surface current fluctuations in the superconducting surface sheath. *Phys. Rev. B*, 72:012507, 2005.

[88] Y. X. Ning, C. L. Song, Z. L. Guan, X. C. Ma, Xi Chen, J. F. Jia, and Q. K. Xue. Observation of surface superconductivity and direct vortex imaging of a Pb thin island with a scanning tunneling microscope. *Europhys. Lett.*, 85:27004, 2009.

[89] H. B. Wang, S. Guénon, J. Yuan, A. Iishi, S. Arisawa, T. Hatano, T. Yamashita, D. Koelle, and R. Kleiner. Hot Spots and Waves in $Bi_2Sr_2CaCu_2O_8$ Intrinsic Josephson Junction Stacks – a Study by Low Temperature Scanning Laser Microscopy. *Phys. Rev. Lett.*, 102:017006, 2009.

[90] R. Werner, A. Yu. Aladyshkin, S. Guénon, J. Fritzsche, I. M. Nefedov, V. V. Moshchalkov, R. Kleiner, and D. Koelle. Domain-wall and reverse-domain superconducting states of a Pb thin-film bridge on a ferromagnetic $BaFe_12O_19$ single crystal. *Phys. Rev. B*, 84:020505(R), 2011.

[91] R. Werner, M. Weiler, A. Yu. Petrov, B. A. Davidson, R. Gross, R. Kleiner, S. T. B. Goennenwein, and D. Koelle. Local tunneling magnetoresistance probed by low-temperature scanning laser microscopy. *Appl. Phys. Lett.*, 99:182513, 2011.

[92] F. S. Bergeret, A. F. Volkov, and K. B. Efetov. Induced ferromagnetism due to superconductivity in superconductor-ferromagnet structures. *Phys. Rev. B*, 69:174504, 2004.

[93] Guy Deutscher. Andreev–Saint-James reflections: A probe of cuprate superconductors . *Rev. Mod. Phys.*, 77:109, 2005.

[94] H.-U. Habermeier, G. Cristiani, R.K. Kremer, O. Lebedev, and G. van Tendeloo. Cuprate/manganite superlattices: A model system for a bulk ferromagnetic superconductor. *Physica C*, 364:298, 2001.

[95] M. Varela, A. R. Lupini, Stephen J. Pennycook, Z. Sefrioui, and J. Santamaria. Nanoscale analysis of $YBa_2Cu_3O_{7-x}/La_{0.67}Ca_{0.33}MnO_3$ interfaces. *Solid State Electron.*, 47:2245, 2003.

[96] Z. L. Zhang, U. Kaiser, S. Soltan, H.-U. Habermeier, and B. Keimer. Magnetic properties and atomic structure of $La_{2/3}Ca_{1/3}$-$MnO_3YBa_2Cu_3O_7$ heterointerfaces . *Appl. Phys. Lett.*, 95:242505, 2009.

[97] V. Peña, Z. Sefrioui, D. Arias, C. Leon, and J. Santamaria. Giant Magnetoresistance in Ferromagnet/Superconductor Superlattices. *Phys. Rev. Lett.*, 94:057002, 2005.

[98] J. Stöhr. Exploring the microscopic origin of magnetic anisotropies with X-ray magnetic circular dichroism (XMCD) spectroscopy. *J. Magn. Magn. Mater.*, 200:470, 1999.

[99] G. Binasch, P. Grünberg, F. Saurenbach, and W. Zinn. Enhanced magnetoresistance in layered magnetic structures with antiferromagnetic interlayer exchange. *Phys. Rev. B*, 39:4828, 1988.

[100] M. N. Baibich, J. M. Broto, A. Fert, F. Nguyen Van Dau, and F. Petroff. Giant Magnetoresistance of (001)Fe/(001)Cr Magnetic Superlattices. *Phys. Rev. Lett.*, 61:2472, 1988.

[101] *http* : *//www.nobelprize.org/nobel*$_p$*rizes/physics/laureates/*2007.

[102] I. Zŭtić, J. Fabian, and S. Das Sarma. Spintronics: Fundamentals and applications. *Rev. Mod. Phys.*, 76:323, 2004.

[103] G.-X. Miao, M. Münzenberg, and J. S Moodera. Tunneling path toward spintronics. *Rep. Prog. Phys,*, 74:036501, 2011.

[104] P. M. Tedrow and R. Meservey. Spin-Dependent Tunneling into Ferromagnetic Nickel. *Phys. Rev. Lett.*, 26:192, 1971.

[105] J. C. Slonczewski. Conductance and exchange coupling of two ferromagnets seperated by a tunneling barrier. *Phys. Rev. B*, 39:6995, 1989.

[106] A. Fert. Nobel Lecture: Origin, development, and future of spintronics. *Rev. Mod. Phys.*, 80:1517, 2008.

[107] J. S. Moodera, L. R. Kinder, T. M. Wong, and R. Meservey. Large Magnetoresistance at room temperature in ferromagnetic thin film tunnel junctions. *Phys. Rev. Lett.*, 74(16), 1995.

[108] T. Miyazaki and N. Tezuka. Giant magnetic tunneling effect in Fe/Al_2O_3/Fe junction. *J. Magn. Magn. Mater.*, 139:L231, 1995.

[109] D. Wang, C. Nordman, J. M. Daughton, Q. Zhenghong, and J. Fink. 70% TMR at room temperature for SDT sandwich junctions with CoFeB as free and reference Layers. *IEEE Trans. Magn.*, 40:2269, 2004.

[110] Stuart S. P. Parkin, Christian Kaiser, Alex Panchula, Philip M. Rice, Brian Hughes, Mahesh Samant, and See-Hun Yang. Giant tunnelling magnetoresistance at room temperature with MgO (100) tunnel barriers. *Nature Materials*, 3:862, 2004.

[111] Shinji Yuasa, Taro Nagahama, Akio Fukushima, Yoshishige Suzuki, , and Koji Ando. Giant room-temperature magnetoresistance in single-crystal Fe/MgO/Fe magnetic tunnel junctions. *Nature Materials*, 3:868, 2004.

[112] Y. M. Lee, J. Hayakawa, S. Ikeda, F. Matsukura, and H. Ohnoa. Effect of electrode composition on the tunnel magnetoresistance of pseudo-spin-valve magnetic tunnel junction with a MgO tunnel barrier. *Appl. Phys. Lett.*, 90:212507, 2007.

[113] W. H. Butler, X.-G. Zhang, T. C. Schulthess, and J. M. MacLaren. Spin-dependent tunneling conductance of Fe/MgO/Fe sandwiches. *Phys. Rev. B*, 63:054416, 2001.

[114] J. Mathon and A. Umerski. Theory of tunneling magnetoresistance of an epitaxial Fe/MgO/Fe(001) junction. *Phys. Rev. B*, 63:220403(R), 2001.

[115] Ze Zhang and Sashi Satpathy. Electron states, magnetism, and the Verwey transition in magnetite. *Phys. Rev. B*, 44:13319, 1991.

[116] Steven P. Lewis, Philip B. Allen, and Taizo Sasaki. Band structure and transport properties of CrO_2. *Phys. Rev. B*, 55:10253, 1997.

[117] R. A. de Groot, F. M. Mueller, P. G. van Engen, and K. H. J. Buschow. New Class of Materials: Half-Metallic Ferromagnets. *Phys. Rev. Lett.*, 50:2024, 1983.

[118] Warren E. Pickett and David J. Singh. Electronic structure and half-metallic transport in the $La_{1-x}Ca_xMnO_3$ system. *Phys. Rev. B*, 53:1146, 1996.

[119] M. Bowen, M. Bibes, A. Barthélémy, J.-P. Contour, A. Anane, Y. Lemaître, and A. Fert. Nearly total spin polarization in $La_{2/3}Sr_{1/3}MnO_3$ from tunneling experiments. *Appl. Phys. Lett.*, 82:233, 2003.

[120] J. Z. Sun, D. W. Abraham, R. A. Rao, and C. B. Eom. Thickness-dependent magnetotransport in ultrathin manganite films. *Appl. Phys. Lett.*, 74:3017, 1999.

[121] M. Bibes, Ll. Balcells, S. Valencia, J. Fontcuberta, M. Wojcik, E. Jedryka, and S. Nadolski. Nanoscale multiphase separation at $La_{2/3}Ca_{1/3}MnO_3/SrTiO_3$ Interfaces. *Phys. Rev. Lett.*, 87:067210, 2001.

[122] A. Tebano, C. Aruta, S. Sanna, P. G. Medaglia, G. Balestrino, A. A. Sidorenko, R. De Renzi, G. Ghiringhelli, L. Braicovich, V. Bisogni, and N. B. Brookes. Evidence of Orbital Reconstruction at Interfaces La[sub 0.67]Ca[sub 0.33]mno[sub 3] films. *Phys. Rev. Lett.*, 100:137401, 2008.

[123] A. Verna, B. A. Davidson, Y. Szeto, A. Y. Petrov, A. Mirone, A. Giglia, N. Mahne, and S. Nannarone. 2010.

[124] J. M. Haeni, C. D. Theis, and D. G. Schlom. RHEED Intensity Oscillations for the Stoichiometric Growth of $SrTiO_3$ Thin Films by Reactive Molecular Beam Epitaxy. *J. Electrocer*, 4:385, 2000.

[125] M. Viret, M. Drouet, J. Nassar, J. P. Contour, C. Fermon, and A. Fert. Low-feld colossal magnetoresistance in manganite tunnel spin valves. *Europhys. Lett.*, 39:545, 1997.

[126] M.-H. Jo, N. D. Mathur, N. K. Todd, and M. G. Blamire. Very large magnetoresistance and coherent switching in half-metallic manganite tunnel junctions. *Phys. Rev. B*, 61:R14905, 2000.

[127] J. O'Donnell, A. E. Andrus, S. Oh, E. V. Colla, and J. N. Eckstein. Colossal magnetoresistance magnetic tunnel junctions grown by molecular-beam epitaxy. *Appl. Phys. Lett.*, 76:1914, 2000.

[128] I. K. Schuller. Unusual phenomena in exchange-biased nanostructures. *Mater. Res. Bull.*, 29:642, 2004.

[129] J. S. Moodera, J. Nassar, and George Mathon. Spin-Tunneling in ferromagnetic junctions. *Annu. Rev. Mater. Sci.*, 29:381, 1999.

[130] M. Bowen, J.-L. Maurice, A. Barthélémy, M. Bibes, D. Imhoff, V. Bellini, R. Bertacco, D. Wortmann, P. Seneor, E. Jacquet, A. Vaurès, J. Humbert, J.-P. Contour, C. Colliex, S. Bl'ugel, and P. H. Dederichs. Using half-metallic manganite interfaces to reveal insights into spintronics. *j. Phys.: Condens. Matter*, 19:315208, 2007.

[131] M. R. Freeman and B. C. Choi. Advances in Magnetic Microscopy. *Science*, 294:1484, 2001.

[132] I. Schmid, M. A. Marioni, P. Kappenberger, S. Romer, M. Parlinska-Wojtan, H. J. Hug, O. Hellwig, M. J. Carey, and E. E. Fullerton. Exchange Bias and Domain Evolution at 10 nm Scales. *Phys. Rev. Lett.*, 105:197201, 2010.

[133] J. Huang, C. Hyun, T.-M. Chuang, J. Kim, J. B. Goodenough amd J.-S. Zhou, J. F. Mitchell, and A. de Lozanne. Magnetic state of $La_{1.36}Sr_{1.64}Mn_2O_7$ probed by magnetic force microscopy. *Phys. Rev. B*, 77:024405, 2008.

[134] R. Wiesendanger. Spin mapping at the nanoscale and atomic scale. *Rev. Mod. Phys.*, 81:1495, 2009.

[135] M. Konoto, T. Kohashi, K. Koike, T. Arima, Y. Kaneko, T. Kimura, and Y. Tokura. Direct Imaging of Temperature-Dependent Layered Antiferromagnetism of a Magnetic Oxide. *Phys. Rev. Lett.*, 93:107201, 2004.

[136] M. Kubota, T. Taniuchi, R. Yasuhara, H. Kumigashira, M. Oshima, K. Ono, H. Okazaki, T. Wakita, T. Yokoya, H. Akinaga, M. Lippmaa, M. Kawasaki, and H. Koinuma. Magnetic domain structure of a technically patterned ferromagnetic $La_{0.6}Sr_{0.4}MnO_3$ thin film. *Appl. Phys. Lett.*, 91:182503, 2007.

[137] M. Veis, Š. Višňovský, Ph. Lecoeur, A.-M. Haghiri-Gosnet, J.-P. Renard, P. Beauvillain, W. Prellier, B. Mercey, J. Mistrík, and T. Yamaguchi. Magneto-optic spectroscopy of $La_{2/3}Sr_{1/3}MnO_3$ films on $SrTiO_3$ (100) and (110) substrates. *J. Phys. D*, 42:195002, 2009.

Appended publications

Reprints of the publications are made with permission of the corresponding journals.

Publication I

Crossover between different regimes of inhomogeneous superconductivity in planar superconductor-ferromagnet hybrids

A. Yu. Aladyshkin,[1,2] J. Fritzsche,[1] R. Werner,[3] R. B. G. Kramer,[1,4] S. Guénon,[3] R. Kleiner,[3] D. Koelle,[3] and V. V. Moshchalkov[1]

[1]*INPAC–Institute for Nanoscale Physics and Chemistry, K.U. Leuven, Celestijnenlaan 200D, B-3001 Leuven, Belgium*

[2]*Institute for Physics of Microstructures RAS, 603950, Nizhny Novgorod, GSP-105, Russia*

[3]*Physikalisches Institut–Experimentalphysik II, Universität Tübingen, Auf der Morgenstelle 14, D-72076 Tübingen, Germany*

[4]*Institut Néel, CNRS–Université Joseph Fourier, BP 166, F-38042 Grenoble Cedex 9, France*

(Received 8 March 2011; revised manuscript received 5 May 2011; published 23 September 2011)

We studied experimentally the effect of a stripelike domain structure in a ferromagnetic $BaFe_{12}O_{19}$ substrate on the magnetoresistance of a superconducting Pb microbridge. The system was designed in such a way that the bridge is oriented perpendicular to the domain walls. It is demonstrated that depending on the ratio between the amplitude of the nonuniform magnetic field B_0, induced by the ferromagnet, and the upper critical field H_{c2} of the superconducting material, the regions of the reverse-domain superconductivity in the H-T plane can be isolated or can overlap (H is the external magnetic field, T is temperature). The latter case corresponds to the condition $B_0/H_{c2} < 1$ and results in the formation of superconductivity above the magnetic domains of both polarities. We discovered the regime of edge-assisted reverse-domain superconductivity, corresponding to localized superconductivity near the edges of the bridge above the compensated magnetic domains. Direct verification of the formation of inhomogeneous superconducting states and external-field-controlled switching between the normal state and inhomogeneous superconductivity were obtained by low-temperature scanning laser microscopy.

DOI: 10.1103/PhysRevB.84.094523 PACS number(s): 74.25.F−, 74.25.Sv, 74.25.Op, 74.78.−w

I. INTRODUCTION

Recent advances in fabrication technology have made it possible to realize superconductor-ferromagnet (S/F) hybrid structures with a controlled arrangement of the ferromagnetic layers or elements. These flux-coupled and exchange-coupled S/F hybrids[1–4] are of fundamental interest for investigations of the nontrivial interaction between superconductivity and a nonuniform distribution of a local magnetic field (or magnetization). Furthermore, S/F hybrids seem to be potential candidates for the development of tunable elements of superconducting electronics.[4] In this paper we focus only on the planar S/F structures, consisting of a low-T_c superconducting film and a ferromagnetic layer with a domain structure with a dominant magnetostatic interaction between superconducting and ferromagnetic films.[5–30]

The nonuniform component of the magnetic field, induced by a ferromagnet, can modify the conditions for the appearance of superconductivity in thin superconducting films due to the effect of field compensation. The formation of localized superconductivity in the areas of compensated magnetic field[31–34] results in an exotic dependence of the superconducting critical temperature T_c on the external magnetic field H, applied perpendicular to the thin film plane. This phase transition line T_c vs H for planar S/F hybrids becomes nonmonotonous[5–17,32–36] and thus it differs significantly from the standard linear dependence of the upper critical field H_{c2} on temperature T, which can be written as

$$1 - \frac{T_c}{T_{c0}} = \frac{|H|}{H_{c2}^{(0)}}. \tag{1}$$

Here T_{c0} is the critical temperature of the superconducting transition at zero magnetic field, $H_{c2}^{(0)} = \Phi_0/(2\pi\xi_0^2)$ and ξ_0 are upper critical field and coherence length at $T = 0$, respectively, and $\Phi_0 = \pi\hbar c/e$ is the magnetic flux quantum. Such dependence given by Eq. (1) is inherent for plain superconducting films in a uniform magnetic field H and shown by the dashed line in Fig. 1.

Considering qualitatively the effect of an inhomogeneous magnetic field, which varies periodically from $+B_0$ (above positive magnetic domains) to $-B_0$ (above negative domains) and remains constant inside the domains, one can expect two different phase transition lines

$$1 - \frac{T_c^{(+)}}{T_{c0}} = \frac{|H + B_0|}{H_{c2}^{(0)}} \quad \text{(positive domains)}, \tag{2}$$

$$1 - \frac{T_c^{(-)}}{T_{c0}} = \frac{|H - B_0|}{H_{c2}^{(0)}} \quad \text{(negative domains)}. \tag{3}$$

These two different transition lines correspond to the formation of superconductivity in the areas where the perpendicular z component of the nonuniform magnetic field is positive, Eq. (2), or negative, Eq. (3). The phase diagram H-T, composed according to Eqs. (2) and (3), is shown in Fig. 1. An inhomogeneous superconducting state, trapped only within the areas above the domains of the opposite polarity with respect to the sign of H, is commonly referred to as reverse-domain superconductivity (RDS).[8–12,35] In order to guarantee the formation of such RDS exclusively above either positive domains (at $H < 0$) or above negative domains (at $H > 0$), one should satisfy $B_0/H_{c2} > 1$ (i.e., at high temperatures and/or large B_0 values). Such separated regions of RDS above the domains of different signs were observed experimentally[10–14,18] for $Pb/BaFe_{12}O_{19}$, $Nb/BaFe_{12}O_{19}$, and $Al/BaFe_{12}O_{19}$ hybrid structures. Upon decreasing T and/or B_0, inhomogeneous

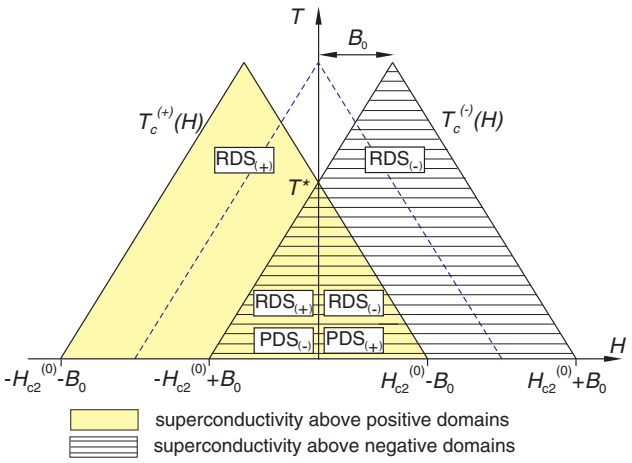

FIG. 1. (Color online) Transformation of the phase diagram "external magnetic field (H)-temperature (T)" in the presence of a nonuniform magnetic field (B_0 is the amplitude of the z component of the stray field). The dashed line is plotted according to Eq. (1). The filled (shaded) area corresponds to inhomogeneous superconductivity above positive and negative magnetic domains, respectively, see Eqs. (2) and (3). Here we use the following notations: $\mathrm{RDS}_{(\pm)}$—reverse-domain superconductivity localized above positive $(+)$ domains at $H < 0$ and above negative $(-)$ domains at $H > 0$; $\mathrm{PDS}_{(\pm)}$—parallel-domain superconductivity localized above positive $(+)$ domains at $H > 0$ and above negative $(-)$ domains at $H < 0$.

superconductivity above magnetic domains of both polarities (i.e., parallel and antiparallel) can coexist (cf. Fig. 1), since both criteria for the formation of inhomogeneous superconductivity above both magnetic domains $|H - B_0| < H_{c2}$ and $|H + B_0| < H_{c2}$ can be fulfilled simultaneously, provided

$$-\left(1-\frac{B_0}{H_{c2}}\right) < \frac{H}{H_{c2}} < \left(1-\frac{B_0}{H_{c2}}\right). \tag{4}$$

The threshold temperature T^* of the crossover from simple RDS to a complex state consisting of RDS in the compensated regions and parallel domain superconductivity (PDS) in the regions with enhanced magnetic field corresponds to the intersection point of the dependencies $T_c^{(+)}(H)$ and $T_c^{(-)}(H)$ at $H = 0$ and can be estimated as $T^* = T_{c0}(1 - B_0/H_{c2})$. Such an inhomogeneous superconducting state, potentially observed in the H range described by Eq. (4) and characterized by a development of superconductivity above magnetic domains of both polarities, can be also called complete superconductivity (CS).

For superconducting samples of finite lateral dimensions one can expect the appearance of surface superconductivity,[37,38] i.e., superconductivity localized near the sample edges even in the presence of a nonuniform magnetic field. In the first approximation, the phase transition line for such anticipated edge-assisted (EA) superconductivity can be described by the shifted H_{c3} dependencies

$$1-\frac{T_c^{(\pm)}}{T_{c0}} = 0.59\,\frac{|H \pm B_0|}{H_{c2}^{(0)}}, \tag{5}$$

where the signs $+(-)$ correspond to edge-assisted superconductivity above positive (negative) magnetic domains, respectively. This means that superconductivity near the sample's edges will survive until the local field exceeds the critical field of surface superconductivity $H_{c3} = 1.69\,H_{c2}$. Furthermore, the presence of the domain walls stimulates the formation of domain-wall superconductivity (DWS) for moderate fields $|H| \leqslant B_0$.[33,36] It has been shown that for thin superconducting films [in the (x,y) plane] in a perpendicular magnetic field $B_z = H + b_z(x)$ with a steplike component $b_z(x) = B_0\,\mathrm{sign}(x)$ induced by a domain wall, nucleation of the superconducting order parameter along the domain wall (at $x = 0$) becomes possible below the phase transition line[39]

$$1-\frac{T_c^{\mathrm{DWS}}}{T_{c0}} \simeq \frac{B_0}{H_{c2}^{(0)}}\left\{0.59 - 0.70\left(\frac{H}{B_0}\right)^2 + 0.09\left(\frac{H}{B_0}\right)^4\right\}.$$

Thus, the set of possible nonuniform superconducting solutions in flux-coupled S/F hybrids has to include the following states: domain-wall superconductivity (DWS), "bulk" RDS and PDS above either positive or negative domains, edge-assisted RDS and PDS above either positive or negative domains, and CS above the domains of both polarities.

In this paper we present an experimental study of the temperature- and field-induced crossover between the different regimes of bulk and localized superconductivity in S/F hybrid structures, consisting of a thin superconducting Pb film on top of a bulk ferromagnetic $BaFe_{12}O_{19}$ single crystal with a well-defined stripelike domain structure. In order to exclude percolation effects and electrical shunting arising from different superconducting states, we prepared the hybrid S/F structure such that the domain walls are oriented *across* the superconducting microbridge. As a result, the current density is distributed over the entire cross section of the microbridge, which allows us to detect variations of the voltage drop associated with the appearance and/or destruction of inhomogeneous superconductivity of various types.

II. MAGNETIC PROPERTIES OF THE FERROMAGNETIC SUBSTRATE

For the creation of a static nonuniform magnetic field with a well-defined domain structure, we used bulk ferromagnetic crystals $BaFe_{12}O_{19}$ (BFO). When cut along the proper crystallographic direction, these BFO crystals exhibit a stripe-type domain structure with dominant in-plane magnetization and a relatively small out-of-plane component of magnetization.[12–14,18]

Measurements with a vibrating sample magnetometer revealed that at low temperatures the magnetization of the used crystal depends almost linearly on the applied perpendicular magnetic field, and that it saturates at $H \simeq 17$ kOe (see Fig. 2). This means that external magnetic field $|H| \leqslant 1.5$ kOe, which corresponds to the range of the H sweeps in our measurements, can only be of minor influence on the domain structure, since the variation of magnetization of the substrate is expected to be not more than 9% of the saturated magnetization.

The spatial two-dimensional (2D) distribution of the perpendicular z component of the magnetic field b_z, induced by the laminar domain structure, was imaged with a scanning Hall probe microscope[40] (Fig. 3). By analyzing the two-dimensional (2D) patterns of $b_z(x,y)$, which corresponds to the difference between the locally measured field $B_z(x,y)$ of

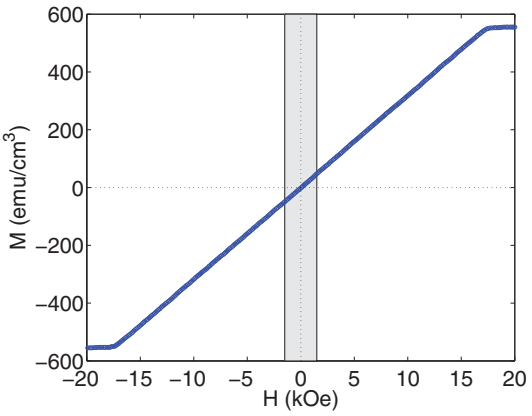

FIG. 2. (Color online) Magnetization curve M vs H, obtained with a vibrating sample magnetometer at $T = 5$ K. The shaded area indicates the range of H in our experiment.

the crystals and the external magnetic field H [Figs. 3(a) and 3(b)], we come to the following conclusions: (i) The domain walls remain rectilinear even in the presence of an external field; and (ii) the effect of the external field is limited mainly to a small displacement of the domain walls as H varies, leading to a broadening of the positive magnetic domains at $H > 0$ at the expense of the negative magnetic domains, and vice versa.

The one-dimensional (1D) profile of the stray field b_z along a line perpendicular to the domain walls is shown in Fig. 3(c). We find that an external field of the order of 1 kOe shifts the points $b_z \simeq 0$ at maximum 3 μm, which is much less than the equilibrium domain width of 30 μm, without substantial changes in both the shape of the domain wall and the amplitude of the built-in magnetic field. This allows us to consider the field pattern as almost independent on H.

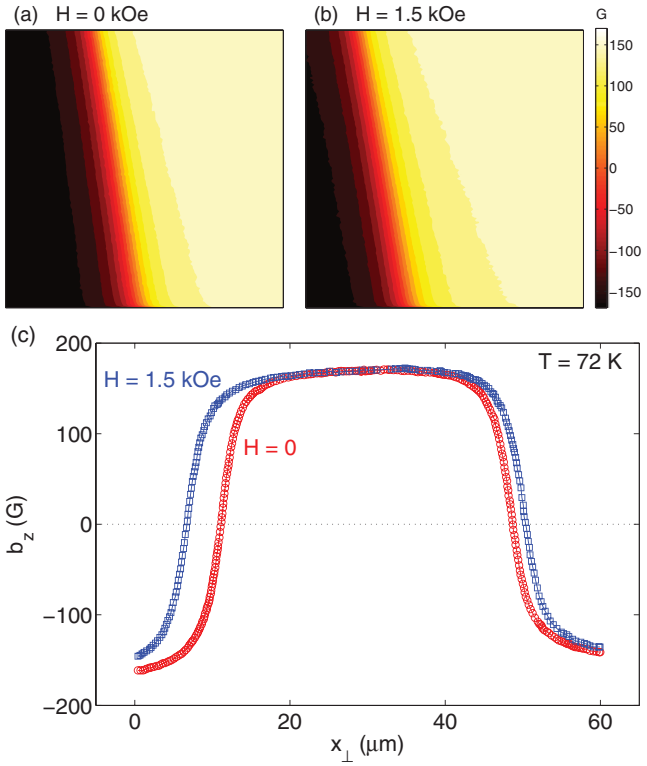

FIG. 3. (Color online) (a), (b) Two-dimensional distribution of the z component of the nonuniform magnetic field $b_z(x,y) = B_z(x,y) - H$ measured near a domain wall by a scanning Hall probe microscope at the distance 400 nm above the ferromagnetic crystal at the external magnetic field $H = 0$ (a) and $H = 1.5$ kOe (b) at $T = 72$ K. The scanning area is 35 μm $\times$ 35 μm. (c) One-dimensional profile of the nonuniform magnetic field $b_z(x_\perp) = B_z(x_\perp) - H$ along the direction perpendicular to two domain walls, measured by a scanning Hall probe microscope for the same conditions: $H = 0$ (red circles) and $H = 1.5$ kOe (blue squares).

III. SUPERCONDUCTING PROPERTIES OF THE S/F BILAYER

A. Sample preparation

After polishing the cut surfaces of the BFO crystals, we prepared lithographically an array of metallic Au markers (2×2 μm in size) on top of the ferromagnetic template. The location of the domain walls with respect to the periodically positioned Au markers was determined with a magnetic force microscope (MFM) at room temperature. A thin insulating Ge layer (4 nm thick) was evaporated in order to prevent exchange interaction and proximity effect between the superconducting and ferromagnetic layers. Finally, two Pb bridges oriented *across* the domain walls were fabricated by means of e-beam lithography, molecular beam epitaxy, and lift-off technique in a single run on the same substrate. These superconducting bridges have the same width (30 μm) and thickness (40 nm) and differ only by their lengths: 100 μm for the short bridge and 700 μm for the long bridge, resulting in different numbers of domain walls (4 and 24, respectively) in the narrow part of the bridges. A combination of an optical and a MFM image of the short Pb bridge is presented in Fig. 4.

B. Magnetoresistive curves $R(H)$

Measurements of the dc electrical resistance R of both the short and the long superconducting Pb bridges, as functions of temperature T, H (applied perpendicularly to the plane of the structures), and the bias current I, were carried out in a commercial Oxford Instruments cryostat using a conventional four-terminal configuration.

Typical $R(H)$ curves measured at $I = 100$ μA are shown in Fig. 5(a). The appearance of two symmetrical minima in $R(H)$ at $T = 7.20$ K corresponds to RDS above the domains of opposite polarity. Taking the positions of the R minima, one can estimate the amplitude of the nonuniform magnetic field B_0 inside the superconducting bridge to 480 Oe. The observed linear increase in the width of the R minima with decreasing temperature (compare the curves from $T = 7.20$ K, and to 6.50 K) allows us to prove the usual relationship $H_{c2} = H_{c2}^{(0)}(1 - T/T_{c0})$ [Eq. (1)] and to estimate both the maximal critical temperature $T_{c0} = 7.25$ K and $H_{c2}^{(0)} \simeq 2.25 \times 10^3$ Oe. Contrary to the previously studied hybrid Al/$BaFe_{12}O_{19}$ bilayers,[12–14] the estimated $H_{c2}^{(0)}$ value for Pb is substantially higher than B_0 at low temperatures.

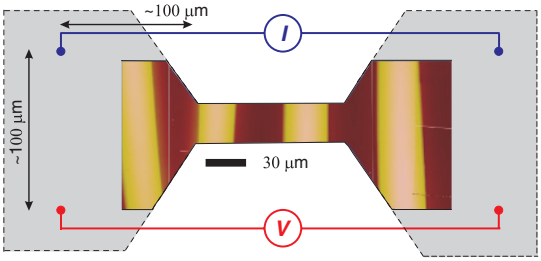

FIG. 4. (Color online) Combined MFM and optical image of the short Pb thin-film bridge fabricated on top of the BFO single crystal. The alternating dark and bright stripes, corresponding to the magnetic domains with different orientations of the magnetic moment, are shown only within the superconducting bridge. All elements of the electrical circuit as well as the geometry of the contact pads (gray areas) are shown schematically.

The ratio $B_0/H_{c2}^{(0)} \simeq 0.2$ gives us the temperature of the anticipated crossover $T^* = 5.70$ K between RDS and CS. The $R(H)$ at $T = 5.70$ K confirms this simple estimate since the sample resistance vanishes for $T < 5.70$ K at $H = 0$, which indicates CS.

Considering the $R(H)$ curves at rather low temperatures ($T < T^*$), one can see that the transition from the superconducting to the normal state upon increasing $|H|$ from zero occurs in two stages. The first stage and an appearance of nonzero resistance can be attributed to the suppression of bulk PDS above the parallel domains since the position of this anomaly corresponds to Eqs. (2) and (3). However, due to the presence of a continuous superconducting path along the sample edges attributed to edge-assisted superconductivity (PDS), the resistance increases slowly as H increases. The exclusive survival of RDS above opposite domains at larger H explains the rise in the total sample's resistance R up to 50%–60% from the normal-state resistance R_n (curves 4.50, 4.90, 5.30, and 5.70 K). Indeed, for the considered topology of the magnetic field, the superconducting and normal regions are connected in series and therefore R should reflect the ratio between the volume of the bridge in the normal state and the total volume of the bridge. We observe that in the developed RDS state R is not constant but slightly increases with $|H|$. This finding can be attributed to the external-field-induced shrinkage of the reverse domains. However, even when bulk RDS is suppressed, the resistance is still lower than the normal resistance. Such a resistive state observed at low temperature and high field can be attributed to the formation of compensated superconductivity above magnetic domains of opposite polarity but localized near the edge of the sample. In the following, this state will be referred to as edge-assisted RDS. Apparently, such states can exist until the local magnetic field above the opposite domains $|H - B_0|$ exceeds the critical field of surface superconductivity $H_{c3} = 1.69H_{c2}$ at a given temperature.[37,38] The position of the critical fields $|H_{c2} + B_0|$ and $|H_{c3} + B_0|$, which determine the shape of the magnetoresistive curve, are shown in Fig. 5(b) for $T = 6.10$ K. For instance, the experimentally determined ratio H_{c3}/H_{c2} for $T = 6.10$ K is close to 1.77, supporting our interpretation.

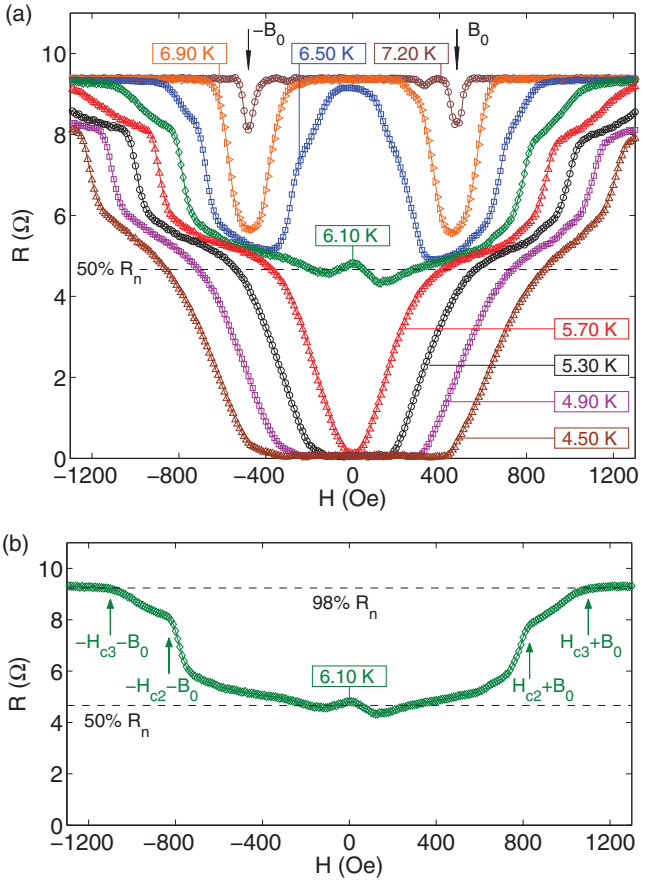

FIG. 5. (Color online) (a) Typical dependencies R vs H taken for the long Pb microbridge at a fixed bias current $I = 100$ μA and at different temperatures T. (b) A single resistive $R(H)$ curve at 6.10 K and the position of the critical fields $|H_{c2} + B_0|$ and $|H_{c3} + B_0|$, marked by arrows: $B_0 \simeq 480$ Oe, $H_{c2} \simeq 350$ Oe, $H_{c3} \simeq 620$ Oe. The two dashed horizontal lines show the levels $0.50R_n$ and $0.98R_n$, where $R_n \approx 9.55$ Ω.

C. *H*-*T* diagram

A full H-T diagram for the long bridge, composed from isothermal $R(H)$ measurements, is presented in Fig. 6(a). A similar diagram for the short bridge is not given since both S/F hybrid samples showed almost identical behavior. The interpretation of all distinctive regions of this diagram is given in Fig. 6(b).

We explain the initial deviation of the resistance from the normal value R_n by the formation of the edge-assisted RDS for large H. Such states I and II are shown schematically in Fig. 6(c). We note that, according to this schematic representation, one might expect that states I and II should yield 50%–60% of the normal-state resistance R_n. Instead, we observe a gradual increase, with increasing H from this value to up to R_n. This deviation can be explained by the bias-current-induced destruction of the superconducting shorts (i.e., quasi-1D) channels of width of the order of the superconducting coherence length) running along the edges. As the critical current for these 1D channels is expected to decrease with increasing H, one expects the observed increase of $R(H)$. For rather high T and moderate H, superconductivity

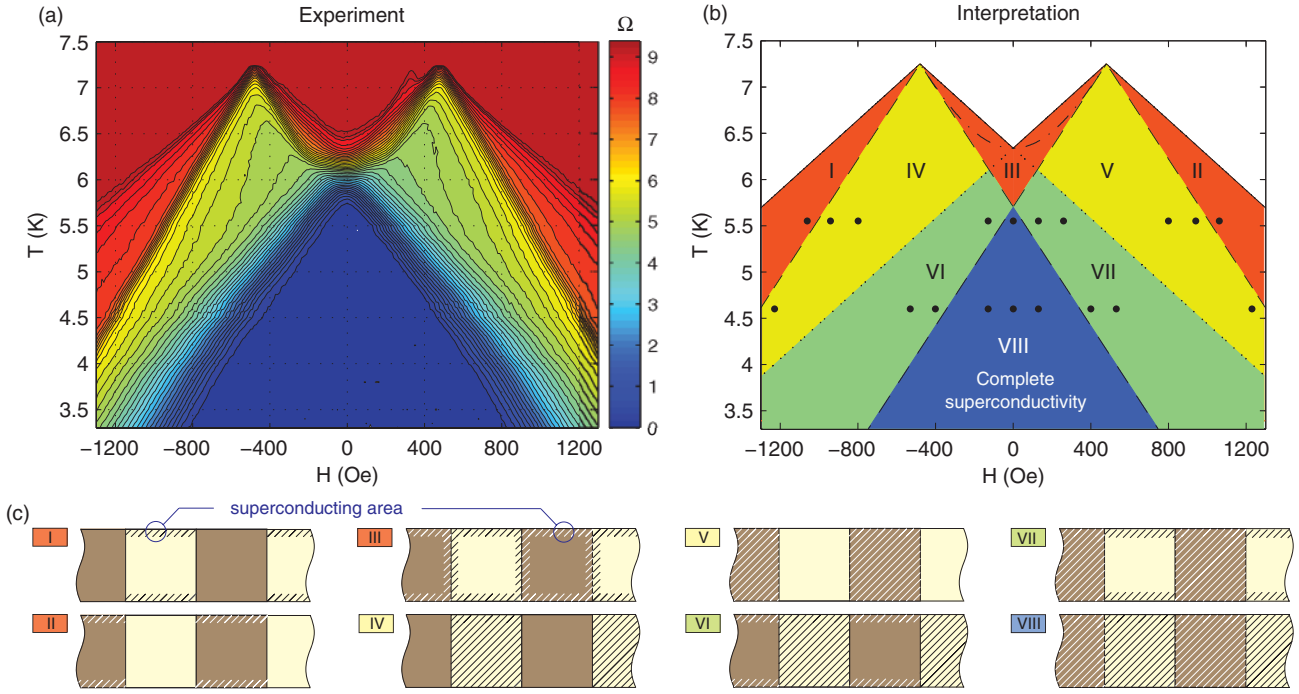

FIG. 6. (Color online) (a) dc resistance R of the superconducting Pb bridge fabricated on top of the BFO crystal as a function of the external magnetic field H and temperature T at $I = 100\ \mu$A. (b) Interpretation of the measured $R(H,T)$ dependence: Solid lines describe the appearance of the edge-assisted reverse-domain superconductivity (EA-RDS), Eq. (5); dashed lines correspond to the appearance of reverse-domain superconductivity (RDS) and parallel-domain superconductivity (PDS), Eqs. (2) and (3); dotted lines describe the formation of edge-assisted parallel-domain superconductivity (EA-PDS); while black dashed-dotted line describes the appearance of domain-wall superconductivity (DWS), Eq. (6). Here we used the following fitting parameters: $T_{c0} = 7.25$ K, $B_0 = 480$ Oe, and $H_{c2}^{(0)} = 2.25$ kOe. The black dots correspond to the low-temperature scanning laser microscopy images obtained at $T = 4.60$ and 5.70 K and which are presented in Figs. 10 and 11, respectively. (c) Schematic presentation of the different regimes of inhomogeneous superconductivity in the considered system. Bright and dark areas correspond to positive and negative magnetic domains respectively, shaded areas depict the expected superconducting regions: I and II—EA-RDS above positive and negative magnetic domains, respectively; III—complex state consisting of DWS and EA-RDS; IV and V—bulk RDS above positive and negative domains, respectively; VI and VII—complex states consisting of RDS and EA-PDS above positive and negative domains, respectively; VIII—complete superconductivity in the entire sample, consisting of RDS and PDS.

might appear in the form of a complex state consisting of edge-assisted superconductivity and DWS (pattern III). This prediction is also confirmed by numerical simulations based on the time-dependent Ginzburg-Landau model. According to our expectations, the localized superconductivity in this case ($|H| < B_0$) appears above the phase transition line depicted by Eq. (6), since the critical temperature for DWS induced by the domain walls of a finite width should be always higher than that for infinitely narrow domain walls. Interestingly, in the overcompensated regime ($|H| > B_0$), the position of the shifted H_{c3} line, Eq. (5), coincides with the level curve $R(H,T) = 0.98R_n$. The next stages of decreasing resistance with decreasing temperature at $|H| \sim B_0$ have to be associated with the appearance of bulk RDS in the compensated regions (patterns IV and V). The corresponding phase boundaries are given by Eqs. (2) and (3) and are shown by black dashed lines in Fig. 6(b). For temperatures below than the transition line given by Eq. (5), in addition to RDS, inhomogeneous superconductivity in the form of edge-assisted PDS also appears in the regions with enhanced magnetic field (patterns VI and VII). It should be mentioned that in our resistive measurements we did not find clear and unambiguous experimental evidences for the mentioned complex states involving DWS and PDS (regions III, VI, and VII in the H-T diagram), although these states are possible from a theoretical point of view. The fact that the resistance in the states III–VII differs from zero can be also attributed to the destruction of the edge-assisted quasi-1D superconducting channels by the finite bias current. Inside the region VIII in the H-T diagram, where areas of inhomogeneous superconductivity for the different domains start to overlap, the total absence of electrical resistance indicates the appearance of CS.[41]

Thus, in our transport measurements, we clearly observed the switching between different regimes of localized superconductivity upon variation of H and T, although the interpretation of the resistance data in regions I, II, III, VI, and VII, which involve the appearance of DWS and/or edge-assisted superconductivity is not straightforward, as these effects can be easily suppressed by the finite bias current.

D. Critical currents

A bias current I can suppress the different modes of nonuniform superconductivity in the considered S/F system in

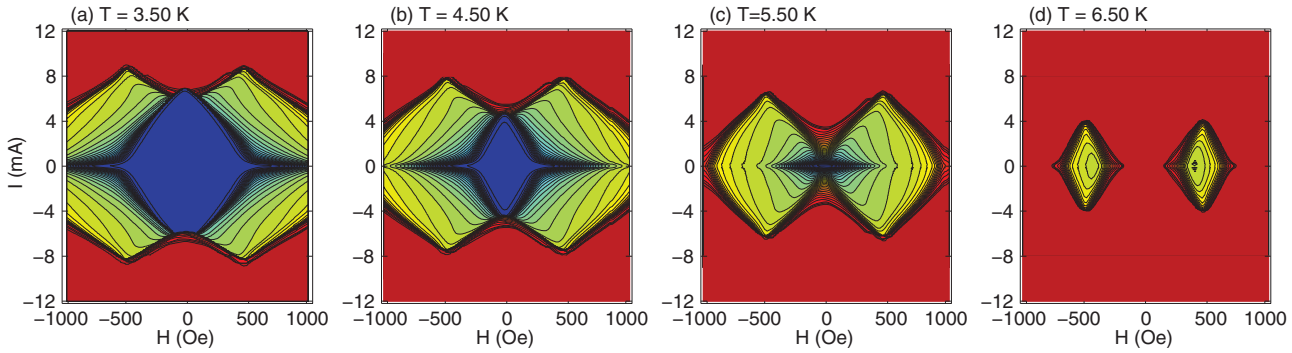

FIG. 7. (Color online) dc resistance $R = V/I$ dependence of the long superconducting Pb bridge on the external magnetic field H and the bias current I taken at different temperatures: $T = 3.50$ K (a), $T = 4.50$ K (b), $T = 5.50$ K (c), and $T = 6.50$ K (d). We use the same color scheme as in Fig. 6(a).

various ways. The effect of H and I on the current (I)-voltage (V) dependencies and on the dc resistance $R = V/I$ are illustrated in Figs. 7 and 8. We observed that the state of RDS is more robust with respect to current injection than the state of CS, since in the latter case the bias current can first destroy the weakly developed superconductivity above parallel magnetic domains (i.e., above positive domains at $H > 0$ and vice versa), where the local magnetic field is maximal.

In order to evaluate the critical current destroying CS and RDS, we consider the effect of T on the I-V dependencies (Fig. 8) measured at $H = 0$ and $|H| \simeq B_0$ (i.e., close to the compensation field). One can see that the state with zero resistance, which is inherent to CS, can be destroyed if I exceeds a threshold value I_c^{CS}. Taking the position of the jumps in the I-V curves at $H = 0$ or the maximal differential resistance dR/dH [Fig. 8(a)], we plotted the the temperature dependence of the critical current I_c^{CS}, corresponding to the destruction of the most developed CS state at $H = 0$. For a characterization of the critical current I_c^{RDS}, corresponding to the suppression of the developed RDS at the compensation field ($|H| \simeq B_0$), we traced the position of the jump on the I-V curves at $H = 480$ Oe upon increasing T [Fig. 8(a)]. Indeed, this estimate seems to be reasonable for the describing of the current-induced destruction of inhomogeneous superconductivity under the condition when the minimal resistance of the investigated sample in the superconducting state is finite (of the order of $50\% R_n$). The dependencies of the both estimated critical currents I_c^{RDS} and I_c^{RDS} as a function of T are presented in Fig. 9.

IV. VISUALIZATION OF NONUNIFORM SUPERCONDUCTING STATES BY SCANNING LASER MICROSCOPY

In order to image the inhomogeneous superconducting states trapped by the nonuniform magnetic field, we used low-temperature scanning laser microscopy (LTSLM).

The principle of operation of LTSLM can be introduced as follows.[9,42–45] The hybrid S/F samples were mounted on the cold finger of a helium gas flow cryostat, which is equipped with optical windows to enable laser irradiation. An amplitude modulated laser beam (wavelength 680 nm, modulation frequency 10 kHz) heats locally the superconducting sample within a spot with a diameter of 1.5–2 μm. This value is determined by the diameter of the focused incident beam and by the thermal conductivity of the tested bilayer sample.[43] The incident beam intensity power on the sample surface (up to $\sim$25 μW) appears to be high enough to provide a maximum beam-induced increase in temperature $\Delta T \sim 0.1$–0.2 K, leading to a local suppression of superconductivity within this

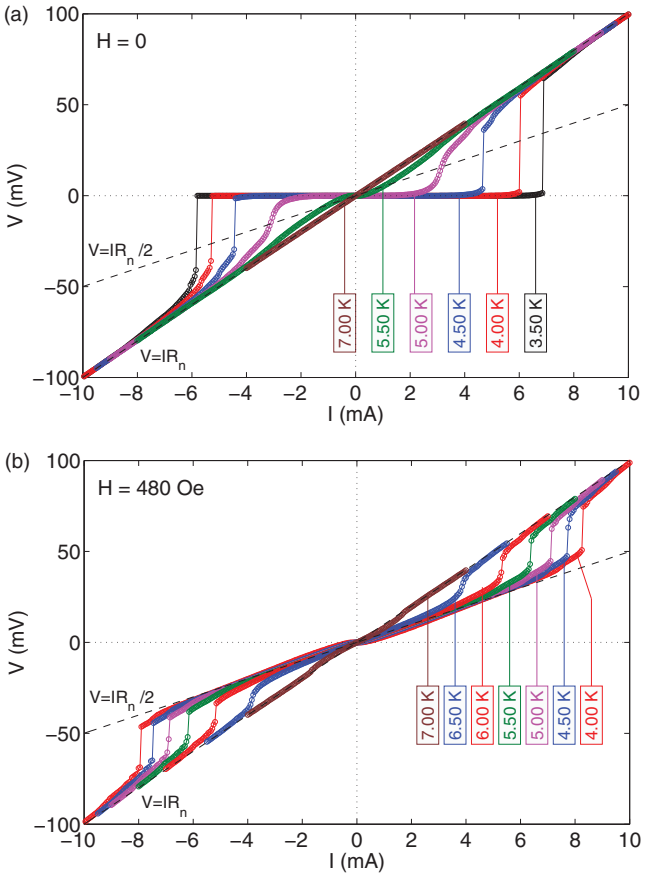

FIG. 8. (Color online) Typical I-V dependencies measured at $H = 0$ (a) and $H = 480$ Oe (b) for the long superconducting Pb bridge at different temperatures indicated in the plots. Two dashed lines correspond to the Ohmic-like behavior with the resistance $R = R_n/2$ and $R = R_n$.

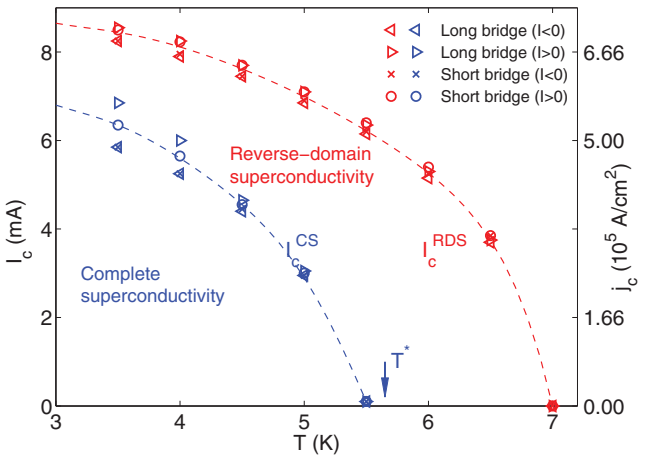

FIG. 9. (Color online) Temperature dependence of the critical currents I_c^{RDS} and I_c^{CS}, corresponding to the suppression of reverse-domain superconductivity (red/light gray symbols near the top line), and complete superconductivity (blue/gray squares near the bottom line), respectively. For the determination of I_c^{RDS} (I^{CS}) we plotted the positions of the maximal differential resistance on the I-V dependencies measured at $H = 480$ Oe ($H = 0$) both for the long and short bridges; $I < 0$ and $I > 0$ denote the negative and positive branches of the corresponding I-V curves (Fig. 8). The dashed lines are guides to the eyes.

hot spot. We assume that the effect of the laser irradiation should be uniform across the superconducting film thickness since the thickness of the Pb film (40 nm) is much smaller than the lateral spot size. In our LTSLM measurements we apply a constant bias current and measure the beam-induced voltage drop ΔV along the entire bridge by lock-in technique. A set of scanning mirrors allows us to control the position (x,y) of the spot and thus to obtain the position-dependent 2D map of the LTSLM signal: $\Delta V = \Delta V(x,y)$.

The LTSLM voltage signal can be interpreted as follows. If the laser spot heats an area of the bridge which is in the normal resistive state, the beam-induced perturbation of the local temperature causes only a very small change in the total resistance, since $\partial R_n/\partial T$ is very small. However, if the irradiated part of the bridge is in the superconducting state and it took part in the transfer of a substantial part of the supercurrents, the beam-induced suppression of superconductivity might switch the whole sample from a low-resistive state to a high-resistive state. In other words, the LTSLM technique makes it possible to map out the ability of the sample to carry supercurrents. Comparing the LTSLM responses upon varying H and T, one can trace the evolution of local superconducting properties in the investigated system.

For the observation of the different regimes of inhomogeneous superconductivity in the long Pb/BFO hybrid samples, we applied a constant current of $I = 300$ μA and the field was varied in the range between $H = \pm 1350$ Oe.

Figure 10 shows the LTSLM images obtained at $T = 4.60$ K, which is below the crossover temperature $T^* = 5.70$ K (see Fig. 11). For $|H| \leqslant 130$ Oe the measured responses have no detectable variations [see Figs. 10(a), 10(b1), and 10(b2)]. Apparently, at these points inside the

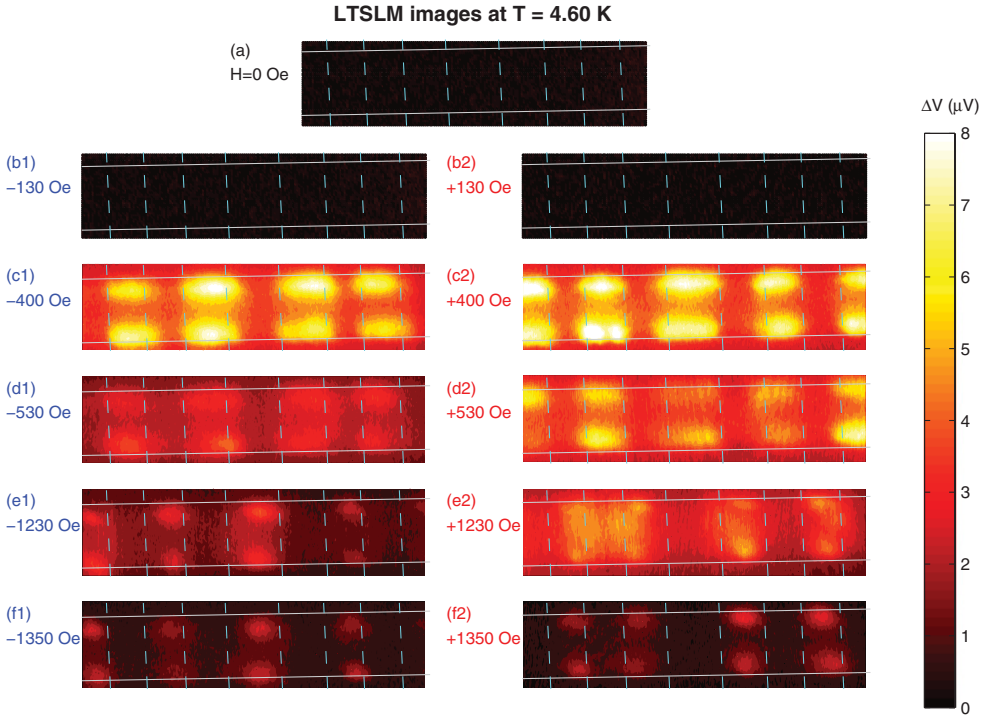

FIG. 10. (Color online) Low-temperature scanning laser microscopy (LTSLM) images obtained for the same area of the long Pb bridge at $T = 4.60$ K. The color scale indicates the change in the beam-induced voltage drop ΔV. The H values are indicated in the plots and the bias points for all presented images are also marked by black dots in the phase diagram in Fig. 6(b). The scanning area is $\sim$120 μm $\times$ 40 μm. Vertical dashed cyan (light gray) lines indicate the positions of the domain walls. The sample edges are marked by horizontal solid white lines.

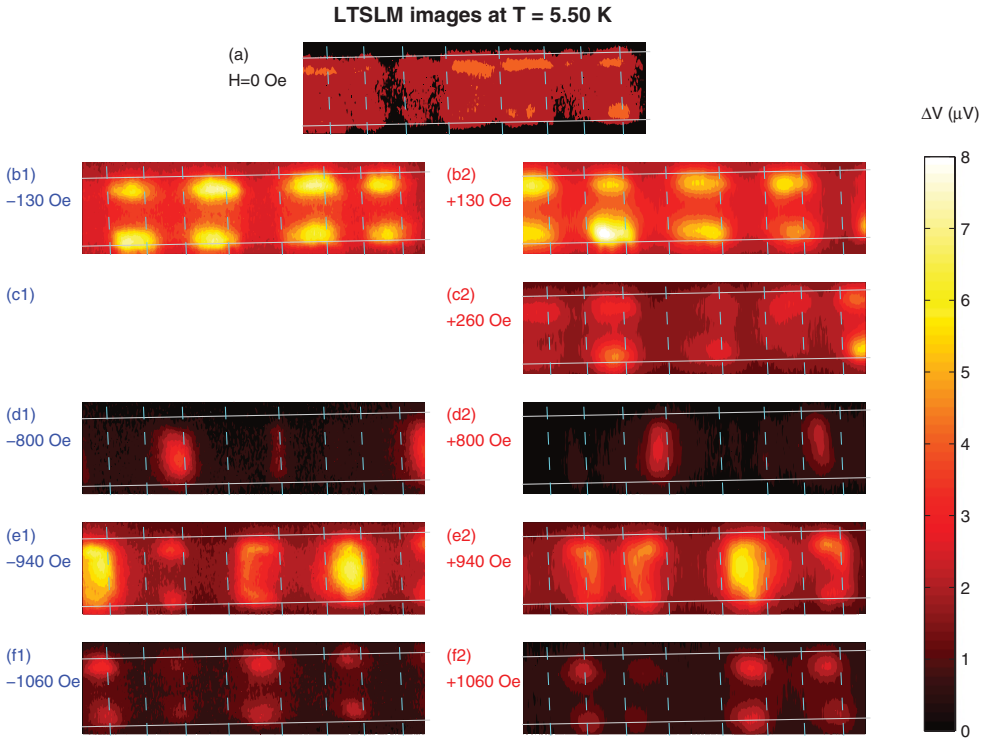

FIG. 11. (Color online) Low-temperature scanning laser microscopy (LTSLM) images obtained for the same area of the long Pb bridge at $T = 5.50$ K. All parameters and notations are the same as in Fig. 10. The LTSLM image at $H = -260$ Oe (c1) was recorded with technical problems and therefore we do not present this plot.

CS state in the H-T diagram, the intensity of the laser beam is insufficient for the destruction of the developed bulk superconductivity.

According to our estimates, at $T = 4.60$ K, the depletion of superconductivity above the parallel magnetic domains should occur at $|H| \gtrsim 350$ Oe. This means that near the "CS-RDS" transition line the areas above the parallel domains have to be in the *resistive* state, while the areas above the opposite domains are still in the superconducting state. As a result, the maxima in the LTSLM response at $H = 400$ Oe should be attributed solely to the nonsuperconducting regions above the positive domains [Figs. 10(c2) and 10(d2)]. Correspondingly, at $H = -400$ Oe the resistive areas above negative domains are responsible for the beam-induced voltage [Figs. 10(c1) and 10(d1)]. At higher H values (i.e., deeper in the RDS areas in the H-T diagram) superconductivity survives exclusively above the opposite domains and such compensated superconductivity is strong enough not to be destroyed by the laser beam of the given intensity. However, close to the transition line "RDS–edge-assisted RDS," describing the destruction of the bulk RDS, the bulk reverse-domain superconductivity becomes weaker and can be affected by the laser beam. Therefore, the bright areas in the corresponding LTSLM signal originate from the regions with the compensated magnetic field above the opposite domains. The inversion of the H sign immediately results in a switching between enhanced reverse-domain superconductivity and depleted parallel-domain superconductivity for the same areas of the superconducting bridge [Figs. 10(e1) and 10(e2) and Figs. 10(f1) and 10(f2)]. Thus, all findings concerning the migration of the maximal beam-induced voltage along the Pb bridge upon varying H are in agreement with our transport measurements.

We would like to note that the LTSLM images [Figs. 10(c1)–10(f1) and 10(c2)–10(f2)] reveal an inhomogeneity of the beam-induced voltage across the width of the bridge. Indeed, the ΔV maxima are always located near the edges of the bridge. At the present moment we have no reliable interpretation of this effect. Probably, it can be explained by the current enhancement near the sample edges, typical for plain superconducting bridges,[46,47] or by a suppression of the energy barrier for flux entry or exit for superconductors in the developed mixed state. Another possible explanation for the pronounced edge signal is the manifestation of edge-assisted PDS, since such edge-assisted PDS states seem to be the states with weakest superconductivity. Finally, the edge signal can be explained by a hampered heat diffusion and, correspondingly, a larger heating effect of the beam focused near the edges as compared to that in the interior of the bridge. Thus, at the current state of our LTSLM measurements we cannot unambiguously interpret the inhomogeneous LTSLM signal across the bridge as a clear evidence of the edge-assisted superconducting states. This issue requires a detailed theoretical treatment which is beyond the scope of the present work.

At $T = 5.50$ K, close to the crossover temperature, a voltage signal can be detected at $H = 0$. The amplitude of the built-in magnetic field is close to the corresponding upper critical field and therefore even a weak optical influence can substantially suppress bulk superconductivity equally above the domains of both polarities. Upon increasing $|H|$ we

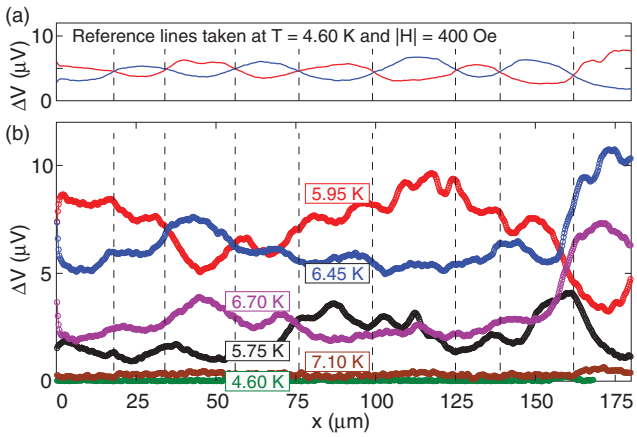

FIG. 12. (Color online) Line scans $\Delta V(x)$ obtained by the LTSLM method at different T along the line close to the lower edge of the Pb microbridge: (a) The reference signal $\Delta V(x)$ measured at $H = \pm 130$ Oe in order to detect the positions of the domain walls shown as vertical dashed lines. (b) The dependencies $\Delta V(x)$ measured at different temperatures (shown in the plot) and $H = 0$.

successively observe the responses from the parallel domains [Figs. 11(b1) and 11(b2)–11(c2)] and from the antiparallel domains [Figs. 11(d1)–11(f1) and 11(d2)–11(f2)], similar to that described above.

In principle, a further increase in temperature above the crossover temperature could allow us to detect the domain-wall superconductivity at $H = 0$, since the masking background signal from CS and the edge-assisted RDS are turned off. The evolution of the beam-induced voltage upon increasing T is presented in Fig. 12, where we show line scans $\Delta V(x)$ along the bridge, close to its bottom edge. However, we did not find any noticeable increase in the LTSLM response near the domain walls for the considered S/F system. Since the DWS state was already successfully observed for a similar Pb bridge oriented along the domain wall using the same LTSLM technique,[48] we believe that for the topology of our investigated sample with domain walls perpendicular to the bridge the LTSLM signal at the domain wall is simply below our detection limit.

V. CONCLUSION

We presented a detailed experimental study of the superconducting properties of thin-film superconducting Pb microbridges in the presence of a nonuniform magnetic field of the laminar domain structure in ferromagnetic $BaFe_{12}O_{19}$ crystals. Such ferromagnets generate rather strong stray fields and the parameters of this field (amplitude and period) are almost independent on the applied magnetic field H in the considered H range. We focused on the case when the domain walls are oriented perpendicular to the bridge in order to avoid electrical shunting and masking of less developed superconducting states by more favorable states during transport measurements. It was demonstrated that at high temperatures superconductivity appears in the form of reverse-domain superconductivity only above magnetic domains of opposite polarity with respect to the H sign. Below the crossover temperature T^*, defined as $H_{c2}(T^*) = B_0$, superconductivity can nucleate both above antiparallel and parallel magnetic domains [B_0 is the amplitude of the perpendicular component of the nonuniform field, $H_{c2} = H_{c2}^{(0)}(1 - T/T_{c0})$ is the temperature-dependent upper critical field]. Indeed, at $T < T^*$ the regions of inhomogeneous superconductivity above positive and negative domains overlap in the H-T plane, resulting in so-called complete (or global) superconductivity and in the vanishing total electrical resistance of the hybrid sample. We also found experimental evidences for the regimes of edge-assisted reverse-domain superconductivity and edge-assisted parallel-domain superconductivity, corresponding to localized superconductivity near the edges of the bridge above the regions with compensated and enhanced magnetic field, respectively. We experimentally determined the critical currents, corresponding to the suppression of the localized superconductivity above parallel and antiparallel magnetic domains in a broad temperature range. The technique of low-temperature scanning laser microscopy made it possible to directly visualize the temperature- and field-induced transitions from complete superconductivity to reverse-domain superconductivity and parallel-domain superconductivity and from these inhomogeneous superconducting states to the normal state. We clearly observed the migration of the maximum of the beam-induced response along the bridge between the domains of different polarity upon sweeping H. At the same time we cannot unambiguously interpret the inhomogeneity of the LTSLM response across the bridge and hope to address this point later on.

ACKNOWLEDGMENTS

This work was supported by the Methusalem Funding of the Flemish Government, the NES–ESF program, the Belgian IAP, the Fund for Scientific Research–Flanders (F.W.O.-Vlaanderen), the Russian Fund for Basic Research, RAS under the Program "Quantum physics of condensed matter," Russian Agency of Education under the Federal Target Program "Scientific and educational personnel of innovative Russia in 2009–2013," and Deutsche Forschungsgemeinschaft (DFG) via Grant No. KO 1303/8-1. R.W. acknowledges support by the Cusanuswerk, Bischöfliche Studienförderung.

[1] A. I. Buzdin, Rev. Mod. Phys. **77**, 935 (2005).
[2] I. F. Lyuksyutov and V. L. Pokrovsky, Adv. Phys. **54**, 67 (2005).
[3] M. Vélez, J. I. Martín, J. E. Villegas, A. Hoffmann, E. M. González, J. L. Vicent, and I. K. Schuller, J. Magn. Magn. Mater. **320**, 2547 (2008).
[4] A. Yu. Aladyshkin, A. V. Silhanek, W. Gillijns, and V. V. Moshchalkov, Supercond. Sci. Technol. **22**, 053001 (2009).
[5] W. Gillijns, A. Yu. Aladyshkin, M. Lange, M. J. Van Bael, and V. V. Moshchalkov, Phys. Rev. Lett. **95**, 227003 (2005).
[6] W. Gillijns, A. Yu. Aladyshkin, A. V. Silhanek, and V. V. Moshchalkov, Phys. Rev. B **76**, 060503(R) (2007).

[7] A. Yu. Aladyshkin, A. P. Volodin, V. V. Moshchalkov, J. Appl. Phys. **108**, 033911 (2010).
[8] Z. Yang, M. Lange, A. Volodin, R. Szymczak, and V. V. Moshchalkov, Nat. Mater. **3**, 793 (2004).
[9] J. Fritzsche, V. V. Moshchalkov, H. Eitel, D. Koelle, R. Kleiner, and R. Szymczak, Phys. Rev. Lett. **96**, 247003 (2006).
[10] Z. Yang, J. van de Vondel, W. Gillijns, W. Vinckx, V. V. Moshchalkov, and R. Szymczak, Appl. Phys. Lett. **88**, 232505 (2006).
[11] Z. Yang, K. Vervaeke, V. V. Moshchalkov, and R. Szymczak, Phys. Rev. B **73**, 224509 (2006).
[12] A. Yu. Aladyshkin, J. Fritzsche, and V. V. Moshchalkov, Appl. Phys. Lett. **94**, 222503 (2009).
[13] A. Yu. Aladyshkin, J. Fritzsche, and V. V. Moshchalkov, Physica C **470**, 883 (2010).
[14] A. Yu. Aladyshkin, D. Yu. Vodolazov, J. Fritzsche, R. B. G. Kramer, and V. V. Moshchalkov, Appl. Phys. Lett. **97**, 052501 (2010).
[15] L. Y. Zhu, T. Y. Chen, and C. L. Chien, Phys. Rev. Lett. **101**, 017004 (2008).
[16] L. Y. Zhu, Marta Z. Cieplak, and C. L. Chien, Phys. Rev. B **82**, 060503(R) (2010).
[17] S. Haindl, M. Weisheit, T. Thersleff, L. Schultz, and B. Holzapfel, Supercond. Sci. Technol. **21**, 045017 (2008).
[18] J. Fritzsche, R. B. G. Kramer, and V. V. Moshchalkov, Phys. Rev. B **80**, 094514 (2009).
[19] V. K. Vlasko-Vlasov, U. Welp, A. Imre, D. Rosenmann, J. Pearson, and W. K. Kwok, Phys. Rev. B **78**, 214511 (2008).
[20] V. Vlasko-Vlasov, U. Welp, G. Karapetrov, V. Novosad, D. Rosenmann, M. Iavarone, A. Belkin, and W.-K. Kwok, Phys. Rev. B **77**, 134518 (2008).
[21] V. Vlasko-Vlasov, U. Welp, W. Kwok, D. Rosenmann, H. Claus, A. A. Buzdin, and A. Melnikov, Phys. Rev. B **82**, 100502(R) (2010).
[22] C. Bell, S. Tursucu, and J. Aarts, Phys. Rev. B **74**, 214520 (2006).
[23] R. K. Rakshit, R. C. Budhani, T. Bhuvana, V. N. Kulkarni, and G. U. Kulkarni, Phys. Rev. B **77**, 052509 (2008).
[24] R. K. Rakshit, S. K. Bose, R. Sharma, N. K. Pandey, and R. C. Budhani, Phys. Rev. B **77**, 094505 (2008).
[25] A. Belkin, V. Novosad, M. Iavarone, J. Fedor, J. E. Pearson, A. Petrean-Troncalli, and G. Karapetrov, Appl. Phys. Lett. **93**, 072510 (2008).
[26] A. Belkin, V. Novosad, M. Iavarone, J. Pearson, and G. Karapetrov, Phys. Rev. B **77**, 180506 (2008).
[27] G. Karapetrov, M. V. Miloševiċ, M. Iavarone, J. Fedor, A. Belkin, V. Novosad, and F. M. Peeters, Phys. Rev. B **80**, 180506 (2009).
[28] A. Belkin, V. Novosad, M. Iavarone, R. Divan, J. Hiller, T. Proslier, J. E. Pearson, and G. Karapetrov, Appl. Phys. Lett. **96**, 092513 (2010).
[29] C. Visani, N. M. Nemes, M. Rocci, Z. Sefrioui, C. Leon, S. G. E. te Velthuis, A. Hoffmann, M. R. Fitzsimmons, F. Simon, T. Feher, M. Garcia-Hernandez, and J. Santamaria, Phys. Rev. B **81**, 094512 (2010).
[30] T. Tamegai, Y. Nakao, S. Mohan, and Y. Nakajima, Supercond. Sci. Technol. **24**, 024015 (2011).
[31] B. Pannetier, S. Rodts, J. L. Genicon, Y. Otani, and J. P. Nozieres, in *Macroscopic Quantum Phenomena and Coherence in Superconducting Networks*, edited by C. Giovannella and M. Tinkham (World Scientific, Singapore, 1995), pp. 17–24.
[32] M. Lange, M. J. Van Bael, Y. Bruynseraede, and V. V. Moshchalkov, Phys. Rev. Lett. **90**, 197006 (2003).
[33] A. Yu. Aladyshkin, A. I. Buzdin, A. A. Fraerman, A. S. Mel'nikov, D. A. Ryzhov, and A. V. Sokolov, Phys. Rev. B **68**, 184508 (2003).
[34] M. V. Milošević, G. R. Berdiyorov, and F. M. Peeters, Phys. Rev. Lett. **95**, 147004 (2005).
[35] A. Yu. Aladyshkin and V. V. Moshchalkov, Phys. Rev. B **74**, 064503 (2006).
[36] A. I. Buzdin and A. S. Mel'nikov, Phys. Rev. B **67**, 020503(R) (2003).
[37] D. Saint-James, G. Sarma, and E. J. Thomas, *Type II Superconductivity* (Pergamon, Oxford, UK, 1969).
[38] M. Tinkham, *Introduction to Superconductivity*, 2nd ed. (McGraw-Hill, New York, 1996).
[39] Equation (6) may be considered as an ultimate estimate of DWS, since the critical temperature of the solution, localized in vicinity of the domain walls of the finite width, will be always higher than that given by Eq. (6).
[40] S. J. Bending, Adv. Phys. **48**, 449 (1999).
[41] Since these tested S/F samples were degraded after the experimental LTSLM session, we were unable to complete our study by another series of transport measurements and/or LTSLM images for the same samples, i.e., in order to show the effect of the bias current on the measured characteristics.
[42] L. R. Testardi, Phys. Rev. B **4**, 2189 (1971).
[43] J. Fritzsche, Ph.D. thesis, Katholieke Universiteit Leuven, 2008.
[44] M. Wagenknecht, H. Eitel, T. Nachtrab, J. B. Philipp, R. Gross, R. Kleiner, and D. Koelle, Phys. Rev. Lett. **96**, 047203 (2006).
[45] H. B. Wang, S. Guénon, J. Yuan, A. Iishi, S. Arisawa, T. Hatano, T. Yamashita, D. Koelle, and R. Kleiner, Phys. Rev. Lett. **102**, 017006 (2009).
[46] M. Yu. Kupriyanov and K. K. Likharev, Fiz. Tverd. Tela **16**, 2829 (1974) [Sov. Phys. Solid State **16**, 1835 (1975)].
[47] A. A. Elistratov, D. Yu. Vodolazov, I. L. Maksimov, and J. R. Clem, Phys. Rev. B **66**, 220506 (2002).
[48] R. Werner, A. Yu. Aladyshkin, S. Guénon, J. Fritzsche, I. M. Nefedov, V. V. Moshchalkov, R. Kleiner, and D. Koelle, Phys. Rev. B **84**, 020505(R) (2011).

Publication II

PHYSICAL REVIEW B **84**, 020505(R) (2011)

Domain-wall and reverse-domain superconducting states of a Pb thin-film bridge on a ferromagnetic $BaFe_{12}O_{19}$ single crystal

R. Werner,[1] A. Yu. Aladyshkin,[2,3] S. Guénon,[1] J. Fritzsche,[2] I. M. Nefedov,[3] V. V. Moshchalkov,[2] R. Kleiner,[1] and D. Koelle[1,*]

[1]*Physikalisches Institut–Experimentalphysik II and Center for Collective Quantum Phenomena in LISA$^+$, Universität Tübingen, Auf der Morgenstelle 14, D-72076 Tübingen, Germany*

[2]*INPAC–Institute for Nanoscale Physics and Chemistry, K.U. Leuven, Celestijnenlaan 200D, B-3001 Leuven, Belgium*

[3]*Institute for Physics of Microstructures RAS, 603950 Nizhny Novgorod, GSP-105, Russia*

(Received 14 February 2011; revised manuscript received 13 May 2011; published 20 July 2011)

We report on imaging of the nonuniform superconducting states in a Pb thin-film bridge on top of a ferromagnetic $BaFe_{12}O_{19}$ single crystal with a single straight domain wall along the center of the bridge by low-temperature scanning laser microscopy. We have visualized domain-wall superconductivity (DWS) close to the critical temperature of Pb, when the Pb film above the domain wall acts as a superconducting path for the current. The evolution of the DWS signal with temperature and the external-field-driven transition from DWS to reverse-domain superconductivity was visualized.

DOI: 10.1103/PhysRevB.84.020505 PACS number(s): 74.78.Na, 74.25.Op, 75.47.−m

It is well known that so-called surface or bound states can be generated by the presence of boundaries in a material. For example, the formation of surface states for a single electron wave function in a semi-infinite crystalline lattice due to the modification of the boundary conditions was described by Tamm[1] and by Shockley.[2] Other examples of bound states are surface plasmons, propagating along the interface between a dielectric and a metal,[3–5] and surface acoustic waves traveling along the surface of a material exhibiting elasticity.[6,7] In both latter cases these waves are confined in the direction perpendicular to the wave vector, i.e., their amplitudes decay exponentially far from the interface or surface. The formation of surface bound states for the superconducting order-parameter wave function Ψ was considered by Saint-James and de Gennes.[8,9] They showed that localized superconductivity at a superconductor (S)/vacuum or S/insulator interface can appear at an applied magnetic field $H_{\rm ext}$ above the upper critical field H_{c2} for bulk superconductivity. Similarly to this surface superconductivity, localized superconductivity can also nucleate near the sample edge in a thin semi-infinite superconducting film[10] or in a thin superconducting disk of very large diameter[11] in a *perpendicular* magnetic field. Such so-called edge superconductivity (ES), with transition temperature $T_c^{\rm ES}$, has the same phase-transition line as surface superconductivity,[12] given by $1-T_c^{\rm ES}/T_{c0}\simeq 0.59\,|H_{\rm ext}|/H_{c2}^{(0)}$. Here, T_{c0} is the superconducting transition temperature in zero magnetic field, $H_{c2}^{(0)}=\Phi_0/(2\pi\xi_0^2)$ and ξ_0 are the upper critical field and coherence length at temperature $T=0$, respectively, and $\Phi_0=\pi\hbar c/e$ is the magnetic-flux quantum. This means that ES will survive up to the critical field $H_{c3}=1.69H_{c2}$, while above $H_{c2}=H_{c2}^{(0)}(1-T/T_{c0})$ bulk superconductivity is totally suppressed.

An alternative way to prepare localized states in superconducting films is to confine the order-parameter wave function by a nonuniform magnetic field in hybrid S/ferromagnet (F) structures (see, e.g., Ref. 13 and references therein). Buzdin and Mel'nikov[14] considered a steplike distribution $b_z(x)=B_0\,\mathrm{sgn}(x)$ of the perpendicular component of the magnetic field, $B_z=H_{\rm ext}+b_z$, induced by domain walls in the ferromagnet (with the z axis perpendicular to the film surface). They demonstrated that superconductivity will survive in vicinity along the step, even if the amplitude of the nonuniform magnetic $B_0>H_{c2}$. The dependence of the transition temperature $T_c^{\rm DWS}(H_{\rm ext})$ for *domain-wall superconductivity* (DWS) in a plain superconducting film (i.e., infinite in lateral direction) can be estimated as $1-T_c^{\rm DWS}/T_{c0}\simeq\{0.59-0.70(H_{\rm ext}/B_0)^2+0.09(H_{\rm ext}/B_0)^4\}B_0/H_{c2}^{(0)}$.[15]

For flux-coupled S/F structures of finite lateral size the localized states of ES and DWS may compete as illustrated in Fig. 1 for the case of a thin-film S strip of finite width above a F substrate with a domain wall along the center of the bridge, for $H_{c2}<B_0<H_{c3}$. For a domain structure with steplike $b_z(x)$ profile and $H_{\rm ext}=0$, ES and DWS nucleate simultaneously in the S strip as shown in Fig. 1(a). Figure 1(b) shows the case of a domain wall with finite width and $H_{\rm ext}=0$. Here, DWS becomes energetically more favorable compared to ES and only DWS nucleates.[16] For $H_{\rm ext}\neq 0$, the local field is compensated above the domain with magnetization direction opposite to $H_{\rm ext}$. If $||H_{\rm ext}|-B_0|<H_{c2}$ superconductivity is turned on above this reverse domain while it is still suppressed above the parallel domain [cf. Fig. 1(c)]. This effect is termed *reverse-domain superconductivity* (RDS).[17,18] We note that when H_{c2} becomes larger than $|H_{\rm ext}|+B_0$ (e.g., upon cooling) above the parallel domain, superconductivity may also nucleate there and the entire strip will be in the superconducting state, which we call *complete superconductivity* (CS).

Fingerprints of RDS and DWS have been found by electric transport measurements on S/F hybrids with a rather complex domain structure in $BaFe_{12}O_{19}$ (BFO) crystals[17] and multilayered CoPt films[19] with perpendicular magnetic anisotropy. Using low-temperature scanning laser microscopy (LTSLM), RDS has been visualized in a hybrid $Nb/PbFe_{12}O_{19}$ system.[18] However, due to the complex domain structure and relatively small domain size, visualization of DWS was not possible. Recently, significant improvements have been achieved, regarding the fabrication of specially polished BFO crystals, characterized by a well defined and stable domain structure with straight domain walls separated by typically 30 μm.[20,21] Here we report on the direct imaging of the development of DWS and RDS in a hybrid S/F

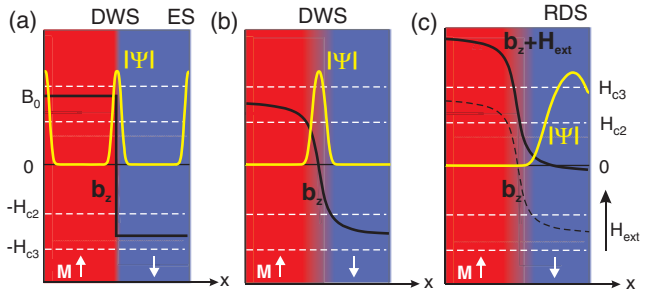

FIG. 1. (Color online) Illustration of DWS, ES, and RDS across a thin-film S strip on top of a F substrate with two domains with perpendicular magnetization $\boldsymbol{M}$. Magnetic-field profiles $B_z(x) = H_{\rm ext} + b_z(x)$ inside the S strip generated by the domains underneath and modulus of superconducting order parameter $|\Psi(x)|$ are shown for (a) steplike $b_z(x)$ for $H_{\rm ext} = 0$, (b) field profile with finite width for $H_{\rm ext} = 0$, and (c) finite $H_{\rm ext} \approx B_0$. White dashed lines indicate upper critical fields $\pm H_{c2}$ and $\pm H_{c3}$.

structure, consisting of a superconducting Pb film on top of a ferromagnetic BFO crystal by means of LTSLM.[18,22–25]

We prepared a 40-nm-thick and 30-μm-wide Pb microbridge on top of a BFO substrate, so that only a single domain wall is running along the center of the Pb bridge parallel to the current flow. The BFO substrate and the Pb thin film were separated by a 4-nm-thick insulating Ge layer so that the system is only flux coupled. From resistance R vs $H_{\rm ext}$ measurements at variable T of a reference sample with several domain walls oriented perpendicular to the long side of the bridge,[26] we compose the $H_{\rm ext}$-T phase diagram shown in Fig. 2(b).

For imaging by LTSLM, the sample was mounted on the cold finger of a helium gas flow cryostat, with an optical window to enable irradiation of the sample surface in the (x,y) plane by a focused laser beam with beam spot diameter $\sim$1.5–2 μm.[24,25] The amplitude modulated laser beam (at frequency $f \approx 10$ kHz) induces a local increase of temperature $\delta T(x - x_0, y - y_0)$ centered at the beam spot position (x_0, y_0) on the sample surface. During imaging, the Pb bridge is biased at a constant current I, and the beam-induced change of voltage $\Delta V(x_0, y_0)$ is recorded with lock-in technique. The LTSLM voltage signal can be interpreted as follows: If the irradiated part of the sample was in the normal state with resistivity ρ_n, the laser beam induces a very small voltage signal $\Delta V \propto \partial \rho_n / \partial T$. However, if the irradiated region took part in the transfer of a substantial part of the supercurrents, the beam-induced suppression of superconductivity might switch the sample from a low-resistive state to a high-resistive state. This effect should be maximal if I is close to the overall critical current $I_c = I_c(T, H_{\rm ext})$ of the sample. In this case LTSLM allows one to map out the ability of the sample to carry supercurrents.

In order to trace out the evolution of DWS with temperature, we recorded a series of LTSLM voltage images $\Delta V(x,y)$ at $H_{\rm ext} = 0$ and different T across the resistive transition of the Pb bridge. Figure 2(a) shows the $R(T)$ curve of the Pb/BFO microbridge; the labels 1–8 indicate the bias points for which LTSLM images and line scans are shown in Figs. 2(d) and 2(c), respectively. The dots in the $H_{\rm ext}$-T phase diagram shown in Fig. 2(b) indicate the bias points for which LTSLM data are shown. LTSLM voltage images 1–8 in Fig. 2(d) show the evolution of the superconducting properties of the Pb/BFO bridge upon cooling through T_c (from left to right) at $H_{\rm ext} = 0$;

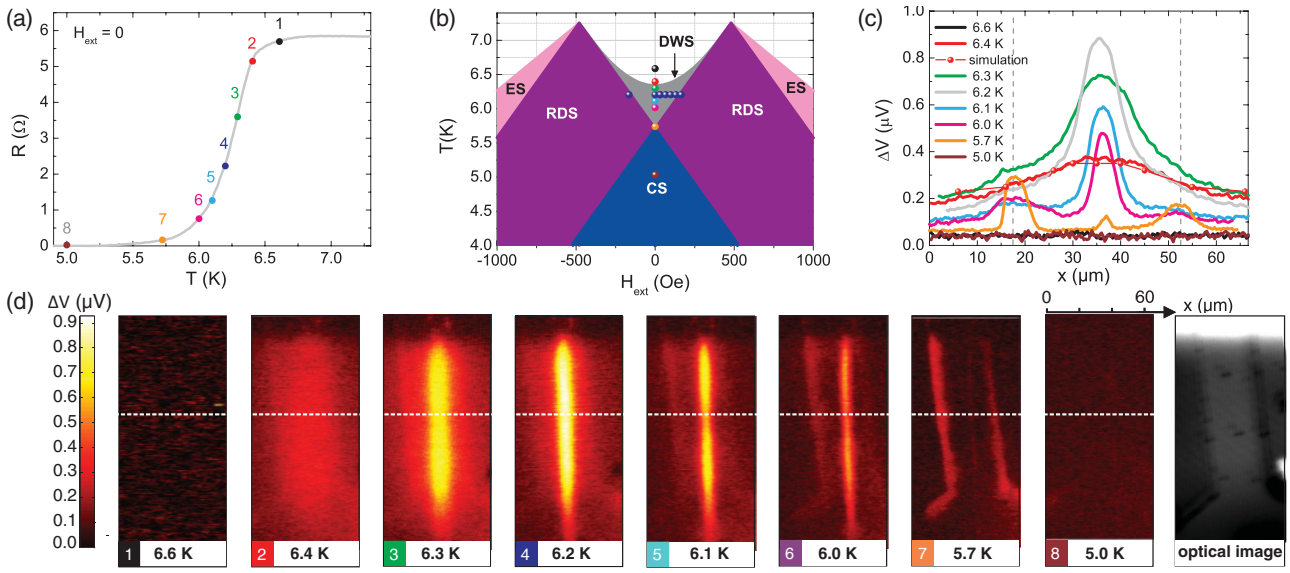

FIG. 2. (Color) Evolution of DWS upon cooling through T_c and $H_{\rm ext}$-T phase diagram. (a) $R(T)$ curve ($I = 100$ μA); dots indicate bias points of LTSLM voltage images 1–8 in (d) and corresponding line scans in (c). (b) $H_{\rm ext}$-T phase diagram, constructed from experimentally determined values $T_{c0} = 7.25$ K, $B_0 = 480$ G, and $H_{c2}^{(0)} = 2.25$ kOe. The phase diagram contains separate regions of DWS, ES, RDS, and CS. Dots label bias points for LTSLM data shown in (c), (d), and Fig. 3. (c) Line scans $\Delta V(x)$ across the bridge for different T, taken from voltage images in (d). Red dots show simulation results for $T = 6.4$ K. The position of the edges of the bridge is indicated by dashed gray lines. (d) Series of LTSLM voltage images $\Delta V(x,y)$ (1–8 from left to right) taken at different T during cooling the Pb bridge through its resistive transition ($I = 10$ μA). White dashed lines indicate the position of line scans in (c). The graph on the right shows a corresponding optical LTSLM image.

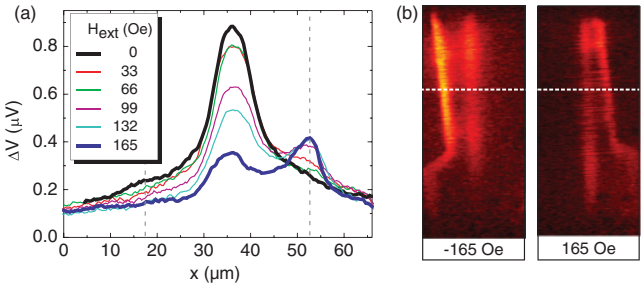

FIG. 3. (Color online) Switching from DWS to RDS: variable $H_{\rm ext}$ at $T = 6.2$ K. (a) Line scans $\Delta V(x)$ along white dashed line in (b) for different $H_{\rm ext} \gtrless 0$; dashed gray lines indicate edges of the bridge. (b) LTSLM images for maximal $|H_{\rm ext}|$.

according to Fig. 2(b), these should cover the transitions from the normal state to DWS and finally to CS. The graph on the right shows an optical LTSLM image, in order to indicate size and position of the bridge in the voltage images.[27] For a more quantitative analysis, in Fig. 2(c) we show line scans $\Delta V(x)$ across the bridge [along the white dashed lines in Fig. 2(d)].

Starting with the highest temperature $T = 6.6$ K, the voltage image in Fig. 2(d) and the corresponding line scan (black line) in Fig. 2(c) shows no signal, as the bridge is in the normal state. Lowering T to 6.4 K [entering the resistive transition shown in Fig. 2(a)], the voltage image gives a small homogeneous signal with a broad maximum centered above the bridge [red line in Fig. 2(c)]. For a (still) resistive Pb bridge with homogeneous conductivity but finite $\partial R/\partial T$, this behavior can be simply explained by the finite width of the beam-induced $\delta T(x,y)$ profile, i.e., its tails will induce a voltage signal, even if the beam spot is positioned outside the bridge. This is confirmed by numerical simulations [cf. red data points in Fig. 2(c)], which solve the heat diffusion equation for an absorbed laser power of 25 μW, a beam spot diameter of 2 μm and thermal conductivity of the BFO substrate of 0.8 W cm^{-1} K^{-1}. These simulations yield a maximum increase in beam-induced temperature $\Delta T = 0.14$ K.

Upon further cooling (see voltage images and corresponding line scans for $T = 6.3$ K and $T = 6.2$ K), a clear LTSLM signal develops, running along the domain wall [green and blue lines, respectively, in Fig. 2(c)]. This observation can be interpreted as an evidence that a channel above the domain wall with higher conductivity than the regions above the domains has formed, and therefore the current density $j(x)$ has a maximum above the domain wall. We note that, although according to the $H_{\rm ext}$-T phase diagram the sample should be in the the DWS state, the overall resistance of the bridge is close to the full normal resistance. This is consistent with numerical simulations based on the time-dependent Ginzburg-Landau equations, which indicate that for our experimental situation the critical current density $j_{\rm c,DWS}$ along the domain-wall channel is too small, i.e., the bias current might be above the critical current of this channel. This also explains why, upon decreasing T, the LTSLM signal at the domain wall increases, as $j_{\rm c,DWS}$ increases, and the peak in $\Delta V(x)$ becomes sharper (see below). We did not find a similar enhancement of the LTSLM voltage signal at the edges of the bridge, i.e., we do not find any signature of ES. We attribute this to the finite width of the domain wall, which stabilizes DWS compared to ES.

For $T < 6.2$ K the amplitude of the peak of the LTSLM response at the domain wall decreases as T decreases, and the maximum of the LTSLM signal shifts toward the edges of the bridge; see magenta and orange lines in Fig. 2(c) for $T = 6.0$ K and $T = 5.7$ K, respectively, and the corresponding voltage images in Fig. 2(d). We interpret this observation as the transition from DWS to CS, which is consistent with the phase diagram shown in Fig. 2(b). At this transition, CS spreading over the whole sample becomes favorable and the sample is turned into the mixed state. The onset of CS can explain the appearance of two pronounced maxima in $\Delta V(x)$ at the sample edges: In the mixed state the current distribution depends on the edge energy barrier for vortex entry. Upon laser irradiation, the edge energy barrier is locally suppressed, which in turn opens a gate for vortex entry/exit. Hence one can expect that irradiation at the edges of the bridge should strongly affect the vortex pattern and the resulting current distribution. In contrast, laser irradiation of the interior of the bridge does not change the existing energy barrier, and the modification of the current pattern is probably less pronounced, and therefore the beam-induced voltage change is much smaller. Finally, at $T = 5.0$ K the LTSLM signal is zero [cf. Fig. 2(d) and brown line in Fig. 2(c)], which indicates that the bridge is in the CS state and the beam-induced perturbation is not strong enough to suppress superconductivity and induce a voltage signal.

Finally, we investigated the effect of finite perpendicular field $|H_{\rm ext}| \leqslant 165$ Oe on superconductivity in our system. The measurements were carried out at $T = 6.2$ K, which corresponds to the most pronounced LTSLM signal above the domain wall at $H_{\rm ext} = 0$. Figure 3(a) shows the evolution of the LTSLM voltage signal $\Delta V(x)$ with increasing external field for positive polarity. For $H_{\rm ext} = 0$ the DWS signal is clearly visible as described above. With increasing $H_{\rm ext}$ the amplitude of the domain-wall signal decreases monotonously while its width stays roughly constant. Simultaneously a signal above the reverse (right) domain appears. In the RDS state, for $H_{\rm ext} \gtrsim 70$ Oe, the voltage signal shows a peak at the right edge of the bridge, which can be explained in the same way as for the edge signal discussed in the context of the T series shown in Fig. 2. Figure 3(b) shows LTSLM voltage images taken at $H_{\rm ext} = -165$ Oe (left image) and $H_{\rm ext} = +165$ Oe (right image), which clearly demonstrate switching between the RDS states above the two domains upon reversing the polarity of the external field.

In conclusion, we have clearly identified the formation of the spatially inhomogeneous superconducting state in a superconducting Pb thin film induced by the stray field of the domains in the ferromagnetic substrate BFO underneath. The crucial feature of the investigated system is that the superconducting Pb bridge was fabricated exactly above a single straight domain wall, which is running along the center of the bridge. Such a well-defined geometry of the hybrid Pb/BFO sample makes it possible to directly visualize the localized and delocalized superconductivity by means of low-temperature scanning laser microscopy. We imaged the evolution of DWS with decreasing temperature. Using the external field as a control parameter, we demonstrated that superconductivity in

a wide superconducting bridge can be switched from the DWS to RDS state. This opens up interesting perspectives for the creation of spatially nonuniform superconducting states and for their manipulation by external and "internal" magnetic fields.

This work was funded by DFG via Grant No. KO 1303/8-1, the Methusalem Funding of the Flemish Government, the NES-ESF program, the Belgian IAP, the Fund for Scientific Research–Flanders (F.W.O.-Vlaanderen), the RFBR, RAS under the Program "Quantum physics of condensed matter," and FTP "Scientific and educational personnel of innovative Russia in 2009–2013." R.W. gratefully acknowledges support by the Cusanuswerk, Bischöfliche Studienförderung.

*koelle@uni-tuebingen.de

[1] I. Tamm, Phys. Z. Sowjetunion **1**, 733 (1932).

[2] W. Shockley, Phys. Rev. **56**, 317 (1939).

[3] R. H. Ritchie, Phys. Rev. **106**, 874 (1957).

[4] L. D. Landau and E. M. Lifshitz, *Electrodynamics of Continuous Media*, 2nd ed. (Pergamon, New York, 1984).

[5] S. A. Maier, *Plasmonics: Fundamentals and Applications* (Springer, New York, 2007).

[6] Lord Rayleigh, in Proc. London Math. Soc. **17**, 4 (1885).

[7] *Acoustic Surface Waves*, Topics in Applied Physics Vol. 24, edited by A. A. Oliner (Springer-Verlag, Berlin, 1978).

[8] D. Saint-James and P. G. de Gennes, Phys. Lett. **7**, 306 (1963).

[9] D. Saint-James, G. Sarma, and E. J. Thomas, *Type II Superconductivity* (Pergamon, New York, 1969).

[10] R. H. White, Phys. Rev. **142**, 241 (1966).

[11] A. Y. Aladyshkin, D. A. Ryzhov, A. V. Samokhvalov, D. A. Savinov, A. S. Melnikov, and V. V. Moshchalkov, Phys. Rev. B **75**, 184519 (2007).

[12] M. Tinkham, *Introduction to Superconductivity*, 2nd ed. (McGraw-Hill, New York, 1996).

[13] A. Y. Aladyshkin, A. V. Silhanek, W. Gillijns, and V. V. Moshchalkov, Supercond. Sci. Technol. **22**, 053001 (2009).

[14] A. I. Buzdin and A. S. Mel'nikov, Phys. Rev. B **67**, 020503(R) (2003).

[15] A. Y. Aladyshkin, A. I. Buzdin, A. A. Fraerman, A. S. Mel'nikov, D. A. Ryzhov, and A. V. Sokolov, Phys. Rev. B **68**, 184508 (2003).

[16] We calculate $|\Psi(x)|$ by solving numerically the linearized Ginzburg-Landau equation for a thin superconducting bridge of finite width in the presence of the nonuniform field $B_z(x) = H_{\rm ext} + (2B_0/\pi)\arctan(x/L)$, following the approach of Ref. 15. The case $L \to 0$ corresponds to a steplike field profile, and any (even very small but) finite L gives a finite transient region for the stray magnetic field near the domain wall. I.e., for the system investigated here, with typical width 5–10 nm of the domain walls in the $BaFe_{12}O_{19}$ substrate, ES will be suppressed.

[17] Z. R. Yang, M. Lange, A. Volodin, R. Szymczak, and V. V. Moshchalkov, Nat. Mater. **3**, 793 (2004).

[18] J. Fritzsche, V. V. Moshchalkov, H. Eitel, D. Koelle, R. Kleiner, and R. Szymczak, Phys. Rev. Lett. **96**, 247003 (2006).

[19] A. Y. Aladyshkin, A. P. Volodin, and V. V. Moshchalkov, J. Appl. Phys. **108**, 033911 (2010).

[20] J. Fritzsche, R. B. G. Kramer, and V. V. Moshchalkov, Phys. Rev. B **80**, 094514 (2009).

[21] A. Y. Aladyshkin, J. Fritzsche, and V. V. Moshchalkov, Appl. Phys. Lett. **94**, 222503 (2009).

[22] A. P. Zhuravel, A. G. Sivakov, O. G. Turutanov, A. N. Omelyanchouk, S. M. Anlage, A. Lukashenko, A. V. Ustinov, and D. Abraimov, Low Temp. Phys. **32**, 592 (2006).

[23] A. Lukashenko, A. V. Ustinov, A. P. Zhuravel, E. Hollmann, and R. Wördenweber, J. Appl. Phys. **100**, 023913 (2006).

[24] M. Wagenknecht, H. Eitel, T. Nachtrab, J. B. Philipp, R. Gross, R. Kleiner, and D. Koelle, Phys. Rev. Lett. **96**, 047203 (2006).

[25] H. B. Wang, S. Guénon, J. Yuan, A. Iishi, S. Arisawa, T. Hatano, T. Yamashita, D. Koelle, and R. Kleiner, Phys. Rev. Lett. **102**, 017006 (2009).

[26] A. Yu. Aladyshkin, J. Fritzsche, R. Werner, R. B. G. Kramer, S. Guenon, R. Kleiner, D. Koelle, and V. V. Moshchalkov, e-print arXiv:1105.1596 (to be published).

[27] The bright area in the upper part of the optical image is due to an Au contact layer on top of the Pb film, which gives a strongly enhanced reflected laser signal and due to reduced absorbtion a reduction of the LTSLM signal, which can be clearly seen in images 2–7 in Fig. 2(d).

Publication III

Edge superconductivity in Nb thin film microbridges revealed by integral and spatially resolved electric transport

R. Werner,[1] A. Yu. Aladyshkin,[2] I. M. Nefedov,[2] A. V. Putilov,[2] M. Kemmler,[1]
D. Bothner,[1] A. Loerincz,[3] K. Ilin,[3] M. Siegel,[3] R. Kleiner,[1] and D. Koelle[1]

[1] *Physikalisches Institut – Experimentalphysik II and Center for Collective Quantum Phenomena in LISA$^+$, Universität Tübingen, Auf der Morgenstelle 14, 72076 Tübingen, Germany*
[2] *Institute for Physics of Microstructures RAS, 603950, Nizhny Novgorod, GSP-105, Russia*
[3] *Institut für Mikro- und Nanoelektronische Systeme, Karlsruher Institut für Technologie, Hertzstraße 16, D-76187 Karlsruhe, Germany*

(Dated: December 13, 2011)

The resistance R vs perpendicular external magnetic field H was measured for superconducting Nb thin–film microbridges with and without microholes [antidots (ADs)]. Well below the transition temperature, integral $R(H)$ measurements of the resistive transition to the normal state on the plain bridge show two distinct regions, which can be identified as bulk and edge superconductivity, respectively. The latter case appears when bulk superconductivity becomes suppressed at the upper critical field H_{c2} and below the critical field of edge superconductivity $H_{c3} \approx 1.7\,H_{c2}$. The presence of additional edges in the AD bridge leads to a different shape of the $R(H)$ curves. We used low-temperature scanning laser microscopy (LTSLM) to visualize the current distribution in the plain and AD bridge upon sweeping H. While the plain bridge shows a dominant LTSLM signal at its edges for $H > H_{c2}$ the AD bridge also gives a signal from the inner parts of the bridge due to the additional edge states around the ADs. LTSLM reveals an asymmetry in the current distribution between left and right edges, which confirms theoretical predictions. Furthermore, the experimental results are in good agreement with our numerical simulations (based on the time-dependent Ginzburg–Landau model) yielding the spatial distribution of the order parameter and current density for different bias currents and H values.

PACS numbers: 74.25.F-, 74.25.Op, 74.25.Dw

I. INTRODUCTION

The concept of localized superconductivity in bulk superconductors was introduced in 1963 by Saint-James and de Gennes[1]. They demonstrated that superconductivity in a semi–infinite sample with an ideal flat surface in the presence of an external magnetic field $\boldsymbol{H}$ (with amplitude H) parallel to its surface can survive in a thin surface layer, even above the upper critical field H_{c2}, when bulk superconductivity is completely suppressed. Based on the phenomenological Ginzburg–Landau theory, the critical field H_{c3} for surface superconductivity, localized near superconductor/vacuum or superconductor/insulator interfaces, can be calculated as[2,3]

$$1.695\,H_{c2} \simeq H_{c3} = H_{c3}^{(0)}\,(1 - T/T_{c0})\,, \qquad (1)$$

where $H_{c3}^{(0)}$ is the upper critical field for surface superconductivity at temperature $T = 0$, and T_{c0} is the superconducting critical temperature for $H = 0$. This theory predicts that in the regime of the surface superconductivity the order parameter wave function Ψ decays exponentially with increasing distance from the surface on the length scale of the coherence length ξ.

Experimental evidence for surface superconductivity has been found by dc transport[4–7] or inductive measurements[8] shortly after the theoretical prediction.[1] Later on, other methods such as ac-susceptibility and permeability measurements,[8–11] magnetization measurements,[12,13] surface impedance measurements[14] and tunneling spectroscopy[15] confirmed the existence of surface superconductivity when $\boldsymbol{H}$ was applied parallel to the surface. The evolution of the resistance R vs H, depending on the orientation of $\boldsymbol{H}$ relative to the surface was also investigated.[4] While two different regions for bulk and surface superconductivity were clearly observed for fields parallel to the surface, no signature for surface superconductivity was observed when $\boldsymbol{H}$ was applied perpendicularly. The in-plane-field dependence of the critical current $I_c(H)$ in the regime of surface superconductivity for $\boldsymbol{H}$ parallel to the bias current was described by Abrikosov[16] and studied experimentally.[17–19] Park described theoretically the evolution of $I_c(H)$ in the state of surface superconductivity when the in-plane field $\boldsymbol{H}$ is applied perpendicular to the bias current flow[20]. He predicted an asymmetry in the critical surface current, resulting from the superposition of surface screening currents and external currents. Such an asymmetry has not been observed experimentally yet.

Similar to surface superconductivity, localized superconductivity can also nucleate near the sample edge in a thin semi-infinite superconducting film, in a thin superconducting disk of very large diameter or around holes in a perpendicular magnetic field.[21–26] It should be mentioned, that surface super-

conductivity and localized states at the sample edges in perpendicular field [called edge superconductivity (ES)] are qualitatively and quantitatively the same. While surface superconductivity has been investigated in several compounds like Pb-based alloys[8,12,27], Nb and Nb-based alloys,[7,11,12,14] polycrystalline MgB_2[28], Pb[8,15,29], UPt_3 whiskers[30], $NbSe_2$[31], experimental studies on ES in thin film structures are rare[32,33]. Recently, the first real space observation of ES was obtained by scanning tunneling microscopy on Pb thin film islands[34].

Localized states do not only occur at sample boundaries but can also be induced by an inhomogeneous magnetic field as it appears e.g. above domain walls in superconductor/ferromagnet hybrids. This localized state is therefore called domain wall superconductivity (DWS)[35–37]. Recently, a $Pb/BaFe_{12}O_{19}$ superconductor/ferromagnet hybrid has been investigated by low-temperature scanning laser microscopy (LTSLM) and the inhomogeneous current distribution of the sample in the DWS state has been visualized.[38] LTSLM is therefore a valuable tool to visualize the redistribution of the current in the crossover from bulk to edge superconductivity.

In this paper we present our investigations on the evolution of edge superconductivity in plain and antidot Nb microbridges in perpendicular magnetic field. Measurements of $R(H)$ were performed to compose an experimental phase diagram and to identify the regions of bulk and edge superconductivity. Then we use LTSLM to visualize the current distribution at the transition from the superconducting to the normal state in both bridges. In addition, we used a time–dependent Ginzburg–Landau model to compare our experimental findings with theoretical predictions.

II. SAMPLE FABRICATION AND EXPERIMENTAL DETAILS

A Nb thin film with thickness $d = 60\,\mathrm{nm}$ was deposited on a single crystal Al_2O_3 substrate (r-cut sapphire) at $T \approx 800^\circ\,\mathrm{C}$ using magnetron sputtering. Two Nb bridges with width $W = 40\,\mu\mathrm{m}$ and length $L = 660\,\mu\mathrm{m}$ were patterned by e-beam lithography and reactive ion etching into a bridge geometry as shown in Fig. 1. One of these bridges was patterned with circular microholes [antidots (ADs) with 580 nm diameter] in a triangular lattice with a period of $1.5\,\mu\mathrm{m}$.

The samples were electrically characterized in a Helium cryostat at $4.2\,\mathrm{K} \leq T \leq 10\,\mathrm{K}$ and $|H| \leq 20\,\mathrm{kOe}$ using a conventional four-terminal scheme (cf. Fig. 1). For both investigated Nb microbridges we found $T_{c0} = 8.5\,\mathrm{K}$. $\boldsymbol{H}$ was always applied along the z-direction, i.e. $\boldsymbol{H} = H\hat{\boldsymbol{e}}_z$ was perpendicular to the thin film surface and the applied bias current I. We performed isothermal measurements of voltage $V(I)$ characteristics for different T and H values out of which we determined the dependence of the dc resistance $R = V/I$ on H. The data presented below were obtained with I=1 mA, unless stated otherwise. This corresponds to a bias current density $J \equiv I/dW \approx 40\,\mathrm{kA/cm^2}$.

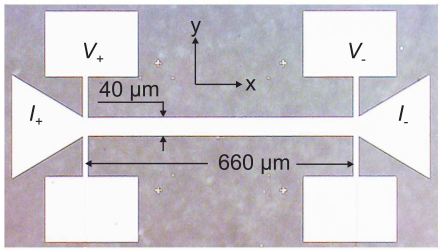

FIG. 1: Optical image of the plain 40 μm wide Nb bridge. The contact pads used for I and V are indicated.

To visualize the current distribution for different bias points in the $T - H$ phase diagram, we used LTSLM.[38–41] For imaging by LTSLM, the sample was mounted on a cold finger of a Helium flow cryostat, which is equipped with an optical window to enable irradiation of the sample in the (x, y) plane by a focused laser beam with beam spot diameter $\sim 1.5-2\,\mu\mathrm{m}$.[39,40] The amplitude modulated laser beam (at frequency $f \approx 10\,\mathrm{kHz}$) induces a local increase of temperature centered at the beam spot position (x_0, y_0) in the sample. During imaging, the Nb bridge is biased at a constant I, and the beam-induced change of voltage $\Delta V(x_0, y_0)$ is recorded by lock-in technique as a function of the beam coordinates (x_0, y_0). The LTSLM voltage signal can be interpreted as follows: If the irradiated part of the sample was in the normal state with resistivity ρ_n, the laser beam induces a very small voltage signal $\Delta V \propto \partial\rho_n/\partial T$. However, if the irradiated part of the bridge took part in the transfer of a substantial part of the superconducting currents, the beam-induced suppression of superconductivity might switch the whole sample from a low-resistive state to a high-resistive state. Details of the LTSLM signal interpretation can be found in Refs. [38–41].

III. RESULTS AND DISCUSSION

A. Magnetoresistance data and Ginzburg-Landau simulations

Figure 2 shows $R(H)$ measurements of the resistive transition at T=4.2 K for different values of I for the plain [Fig. 2(a)] and the AD bridge [Fig. 2(b)]. All curves are normalized to the normal state resistance R_n at H=9.0 kOe. Except for the AD bridge at the highest current value of 10 mA, all $R(H)$ curves reach R_n at the same field value $|H| \approx 8\,\mathrm{kOe}$. However, we observe a pronounced dependence of the shape of the

$R(H)$ curves on I, which we describe and discuss in the following.

For the plain bridge [cf. Fig. 2(a)], at the highest current value of 10 mA, we observe with increasing $|H|$ an onset of dissipation (appearance of a finite R) at ∼3 kOe. Upon further increasing $|H|$, the slope $dR/d|H|$ steadily increases, yielding a rather steep $R(|H|)$ transition curve up to $\sim 0.9R_n$. At $\sim 0.9R_n$ ($|H| \sim$4.4 kOe) a kink in $R(|H|)$ appears, i.e. with further increasing $|H|$, the slope $dR/d|H|$ is significantly reduced. Upon reducing I, the field value where the kink appears stays almost constant; however, the resistance at the kink steadily decreases, and becomes zero for $I <$0.5 mA, i.e. the kink disappears. Similar shapes of the $R(H)$ curves (including the above described kink) and their current dependence as shown in Fig. 2(a) for the plain bridge have been found in [4,7] when $\boldsymbol{H}$ was applied parallel to the sample surface.

The $R(H)$ measurements of the AD bridge [cf. Fig. 2(b)] show similar behavior upon variation of I as compared to the plain bridge in the following sense: Within the same range of (high) bias currents, the onset of dissipation appears almost at the same H value (for the same value of I) as for the plain bridge. Upon further increasing $|H|$, a similar steep transition (with slightly smaller slope as for the plain bridge) appears, up to the kink in $R(|H|)$, which is also present for the AD bridge within the same range of (high) bias currents.

However, we also observe distinct differences by comparing the AD and plain bridge: The resistance at the kink is lower for the AD bridge. This deviation increases with increasing bias current. Furthermore, for the two highest I values the AD bridge shows a second kink in the $R(H)$ curve where the slope $dR/d|H|$ suddenly increases again with increasing H; this feature is absent at smaller I and is not seen for the plain bridge for all values of I. Finally, for the two lowest I values, the onset of dissipation (upon increasing $|H|$) is shifted to larger $|H|$ values for the AD bridge, as compared to the plain bridge.

In the following, we present an interpretation of the $R(H)$ curves described above, starting with the discussion of the results obtained for the plain bridge. At the highest I=10 mA, upon increasing the external magnetic field from $H = 0$, vortices will enter the sample when H is larger than the field of first vortex entry, which is rather small for thin-film structures in perpendicular magnetic field. The onset of energy dissipation can then be attributed to the onset of motion of vortices, when the bias current density J exceeds the depinning current density J_{dpin} at a given T and H. In this case, upon further increasing H, the flux flow resistance will strongly increase, i.e. , the rather large slope dR/dH should correspond to the bias-current-stimulated motion of the vortex lattice in the presence of a strong pinning potential. The kink in the $R(H)$

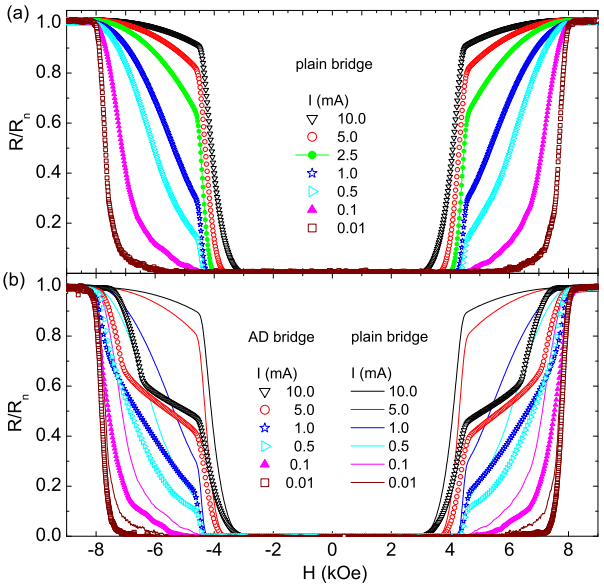

FIG. 2: (Color online) $R(H)$ curves (normalized to normal state resistance R_n) measured at T=4.2 K with different bias currents I=0.01–10 mA for (a) the plain and (b) the AD bridge. To facilitate the comparison, in (b) the data from (a) are shown again as thin lines.

curve where the slope dR/dH substantially decreases (upon increasing H), can be assigned to the transition from the resistive flux-flow regime to a resistive regime with fully suppressed bulk superconductivity and surviving ES at H_{c2} (and above). This interpretation is the same as given in [7] (for surface superconductivity with $\boldsymbol{H}$ parallel to the sample surface). However, in contrast to our observation, a more gradual transition to R_n already at H_{c2} without any kinks and no signature of ES was observed in [4,7] when $\boldsymbol{H}$ was applied perpendicular to the sample surface.

We would like to emphasize that the position of the kink should be close to the upper critical field H_{c2} but not identical to it, since the destruction of bulk superconductivity is a thermodynamical property of a material, but the kink can be observed only under strong non-equilibrium conditions upon the bias current injection. Still, below we use the field value where the kink appears as the experimentally determined H_{c2} value.

Obviously, in our case the edge states form continuous channels with enhanced conductivity, which reduce the overall resistance to a value below R_n. The observed reduction of the resistance at the kink feature in $R(H)$ with decreasing I can be explained by the strengthening of ES upon decreasing I, until at small enough currents the injected bias current flows entirely as a dissipationless supercurrent along the edge channels at $H = H_{c2}$, leading to a disappearance of the kink feature.

As described above, the full normal resistance R_n

is reached (for all I values) at the same field, which we now associate with the upper critical field $H_{c3} \approx 1.7H_{c2}$ for ES. An analysis of the T dependence of H_{c2} and H_{c3} will be presented in Sec. III B.

In the AD bridge, the holes lead to additional "edges" in the sample interior, which results in a higher volume fraction of ES and more effective pinning. This explains the lower R value (as compared to the plain bridge) at the kink when bulk superconductivity becomes suppressed at H_{c2}. The origin of the second kink at $H_{c2}<|H|<H_{c3}$, developing at rather large bias current [Fig. 2(b)], might be associated with a slightly reduced H_{c3} value at the AD edges, as compared to the edges of the bridge, due to the different edge geometry. However, further investigations are required to provide a more conclusive explanation on this feature. Similarly, we cannot yet provide an explanation for the observed shift of the onset of dissipation to larger H, for the AD bridge (as compared to the plain bridge) for the lowest values of I.

To compare the experimental results with theoretical calculations based on the Ginzburg-Landau (GL) model described in the Appendix, we calculated for a rectangular plain superconducting thin film ($W = 30\,\xi_0$, $L = 60\,\xi_0$; ξ_0 is the GL coherence length at $T = 0$) the spatial distribution and time dependence of the normalized order parameter (OP) wave function $\psi(x, y, t)$ and the voltage drop $V(t)$ along the rectangle for different values of H and normalized bias current density j at a reduced temperature T/T_c=0.47 (corresponds to T=4.2 K for Nb with T_c=9 K). We want to note, that the real dimensions of the investigated sample exceed considerably the dimensions used in our modeling. Nevertheless, the model correctly captures the essential physics behind the discussed effects for $H > H_{c2}$. Figure 3(a) shows the spatial distribution $|\psi(x, y)|$ for a rather small value of j=5 × 10^{-4} for five different values of H/H_{c2} from 0.19 to 1.50. We note that the chosen value for j is several orders of magnitude below the GL depairing current density $j_{\rm GL}$=0.386 [cf. the appendix] at T=0. In all cases, the OP distributions are time-independent ("stationary case") corresponding to zero resistance. At $|H| < H_{c2}$, a regular vortex structure appears and the density of vortices increases with increasing H. However, even when bulk superconductivity is depleted at $|H| > H_{c2}$, superconducting channels with finite and time-independent $|\psi|$ running along the edges of the rectangle are still present and can provide a non-dissipative current transfer. If H is further increased, the superconductor turns to a non-stationary regime with finite resistance and reaches its normal value at the upper critical field for ES at $H = H_{c3}$. The calculated R/R_n vs H/H_{c2} curves for different j are shown in Fig. 3(b). The numerical simulations reproduce the shift of the curves to smaller H and the decrease of the slope dR/dH in the interval $H_{c2} < |H| < H_{c3}$ as j increases. This is

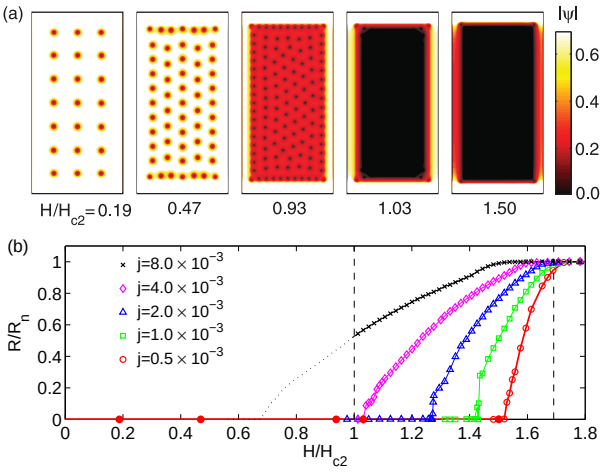

FIG. 3: (Color online) Numerical GL-simulation results for a superconducting rectangular thin film ($W = 30\,\xi_0$, $L = 60\,\xi_0$) biased at normalized current density j at variable magnetic field H and T/T_c=0.47. (a) Spatial distribution of the modulus of the normalized order parameter wave function $|\psi(x, y)|$ with j=0.5×10^{-3} [lowest value in (b)]. The five panels show simulation results for different values of H/H_{c2}; j is flowing from top to bottom. (b) R/R_n vs H/H_{c2} for different j. Two vertical dashed lines depict the upper critical field H_{c2} and the critical field of ES $H_{c3} = 1.695\,H_{c2}$.

qualitatively the same as observed experimentally in Fig. 2. However, for large enough j (finite R at H_{c2}) our model is unable to describe the kink in $R(H)$ close to H_{c2} and the disappearance of R for $H < H_{c2}$, since bulk pinning was not taken into account [cf. curve for $j = 8 \times 10^{-3}$ in Fig. 3(b)]).

B. Superconducting phase diagram for the plain bridge

Figure 4(a) shows the results of the $R(H)$ measurements for T=4.2–8.7 K. With increasing T, the deviation from $R = 0$ and the kink, both shift to smaller H values, and the resistance at the kink shifts to a higher R/R_n ratio, while the change in the slope dR/dH at the kink becomes less pronounced. In order to experimentally determine H_{c2} and H_{c3} we use the field value at the kink and a criterion of 0.98 R_n, respectively. The determined transition lines for $H_{c2}(T)$ and $H_{c3}(T)$ for the above mentioned criteria are shown in Fig. 4(b). The experimental transition line for $H_{c3}(T)$ can be fitted with Eq. (1) and $T_{c0} = 8.5$ K which extrapolates to $H_{c3}^{(0)}$=15.3 kOe. Plotting the transition line for $H_{c2}(T)$ with the relation $H_{c3}(T) = 1.695\,H_{c2}(T)$, we find that the experimentally determined H_{c2} values are close to the calculated transition line for bulk superconductivity. This result gives convincing evidence that depending on T, I and H (per-

pendicular to the sample surface), our sample can be either in the state with developed bulk superconductivity and pinned vortex lattice ($H < H_{c2}$), or in the resistive state, controlled by ES ($H_{c2} < H < H_{c3}$).

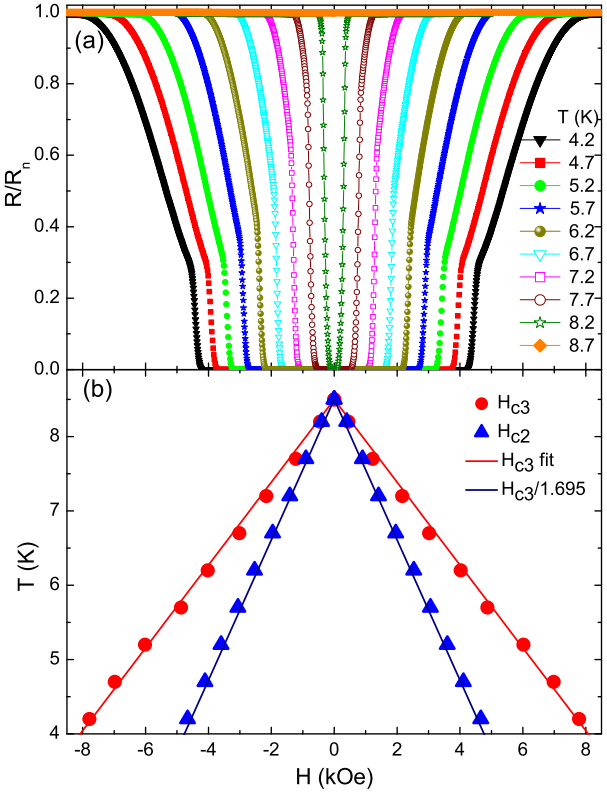

FIG. 4: (Color online) (a) $R(H)$ curves (normalized to normal state resistance R_n) of the plain bridge for T=4.2–8.7 K (from outside to inside). (b) $H-T$-phase diagram of the plain bridge. Data points for H_{c3} (dots) and H_{c2} (triangles) are deduced from $R(H)$ curves in (a). The lines are the transition lines for ES, which were fitted to the data points with Eq. (1) and $T_{c0} = 8.5$ K, and the calculated transition lines for H_{c2} using the relation $H_{c3} = 1.695\, H_{c2}$

C. Visualization of the current distribution by LTSLM

We used LTSLM to visualize the current distribution in the Nb bridges during the transition from bulk superconductivity to the normal state. As the maximum H was limited to $\sim$ 2 kOe in this setup, the LTSLM measurements were performed at rather high T values, $T = 7.0 - 7.5\,K$.

Figure 5(a) shows an H-series of beam-induced voltage images, $\Delta V(x, y)$, at T=7.5 K for various superconducting states of the plain Nb bridge, oriented vertically in all these images [cf. optical image (left panel) in Fig. 5(a)]. For a more quantitative analysis, we show an H-series of linescans, $\Delta V(y)$, across the bridge in Fig. 5(b) and (c). The insets in Fig. 5(b) and (c) show the corresponding $R(H)$ curve, from which we estimate H_{c2} ≈1.1 kOe and H_{c3} ≈1.8 kOe. At $H = 0.67$ kOe in Fig. 5(a), the LTSLM signal is zero, which means that the beam-induced perturbation is not strong enough to suppress superconductivity and to induce a voltage signal. Upon increasing H, the first signal appears at $H \approx 0.8$ kOe which corresponds to the onset of the resistive transition [see inset in Fig. 5(b)]. With further increasing H, the signal at the edges is enhanced, but also a signal from the inner part of the bridge appears. The latter can be attributed to the depletion of bulk superconductivity with increasing H (below H_{c2}), which leads to an increasing voltage response to the perturbation by the laser beam with a maximum beam-induced voltage signal at $H = 1.06$ kOe, which is very close to the estimated H_{c2} value. The pronounced edge signal below H_{c2} can be explained by the suppression of the edge barrier for vortex entry/exit by the laser spot. Hence one can expect that irradiation at the edges of the bridge should strongly affect the vortex pattern and the resulting current distribution. In contrast, laser irradiation of the interior of the bridge does not change the energy barrier and the modification is probably less pronounced and the signal in the interior is much smaller.

Fig. 5(c) shows linescans for $H \geq H_{c2}$. For fields larger than H_{c2}, the beam-induced voltage in the center of the bridge drops almost to zero while large peaks are still observed at the edges of the bridge. This apparently reflects the fact that above H_{c2}, the bulk is no longer superconducting and therefore does not lead to a voltage signal, while the edges still contribute to a strong LTSLM signal due to ES. The rather large width of these edge peaks in the state of ES can be explained by the fact that the edge states are not only perturbed when the laser beam spot is centered right at the edges, but also when the tail of the beam-induced heat distribution leads to a suppression of the edge states when the beam is centered slightly off the edges. A further increase in H leads to a gradual decrease of the edge peaks which finally disappear at $H = 1.76$ kOe which is close to H_{c3}. Above H_{c3}, the sample is completely in the normal state and the effect of the laser beam on the resistive state is negligible.

In summary, the linescan series in Fig. 5(c) indicate, that above H_{c2}, the dominant part of the current is flowing at the edges of the sample. Thus, LTSLM seems to be a capable to visualize the ES states and to identify the different regimes in the $R(H)$ curves for the plain bridge.

For comparison, we show a linescan series (variable H) for the plain [Fig. 6(a)] and AD bridge [Fig. 6(b)] at $T = 7.0$ K. The corresponding $R(H)$ curves with the bias points of the linescans are shown in Fig. 6(c). The H_{c2} value for this temperature is $\sim$ 1.6 kOe. We note, that the beam-induced signal of the AD

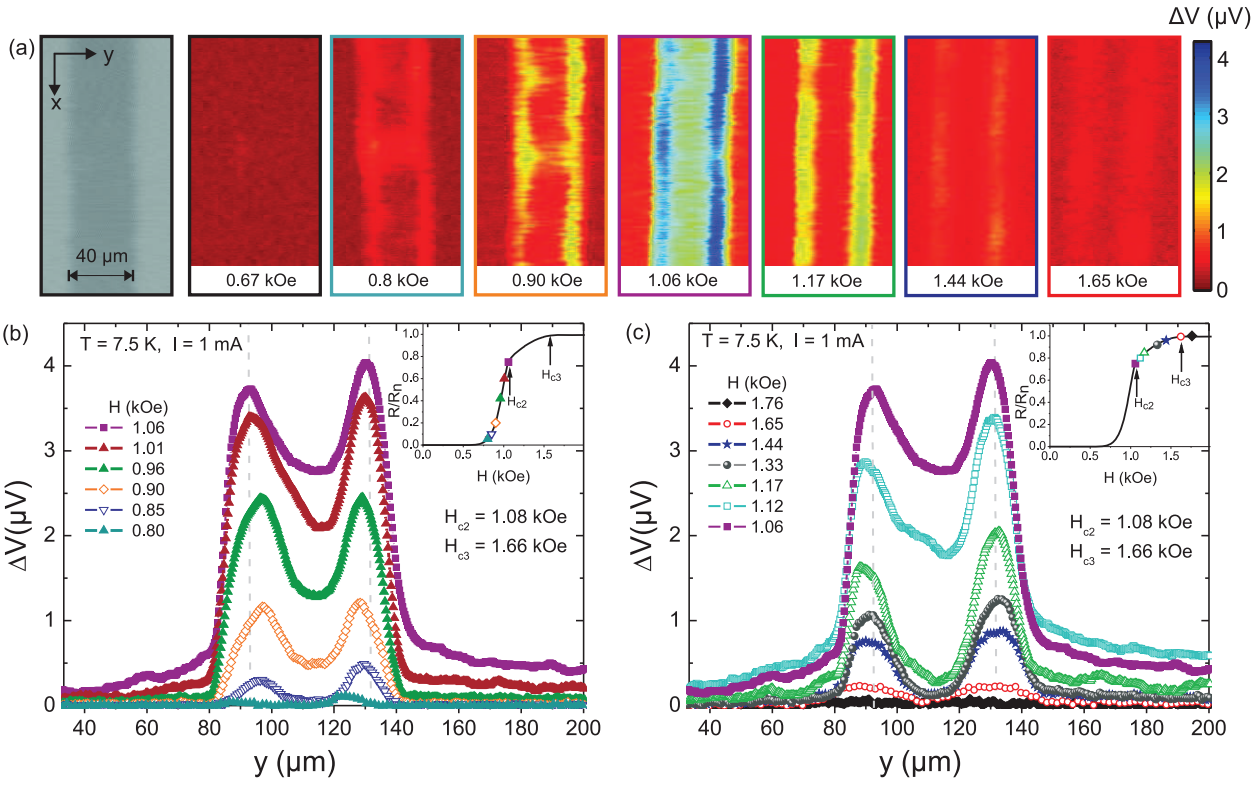

FIG. 5: (Color online) LTSLM signals from plain Nb bridge at T=7.5 K. (a) Optical image (left) and voltage images $\Delta V(x, y)$ for different H; (b) linescans $\Delta V(y)$ across the bridge for $H \leq H_{c2}$ and (c) for $H \geq H_{c2}$. The insets in (b) and (c) show the $R(H)$ curve with corresponding bias points for the linescans. Vertical dashed lines in (b) and (c) indicate position of the edges of the bridge

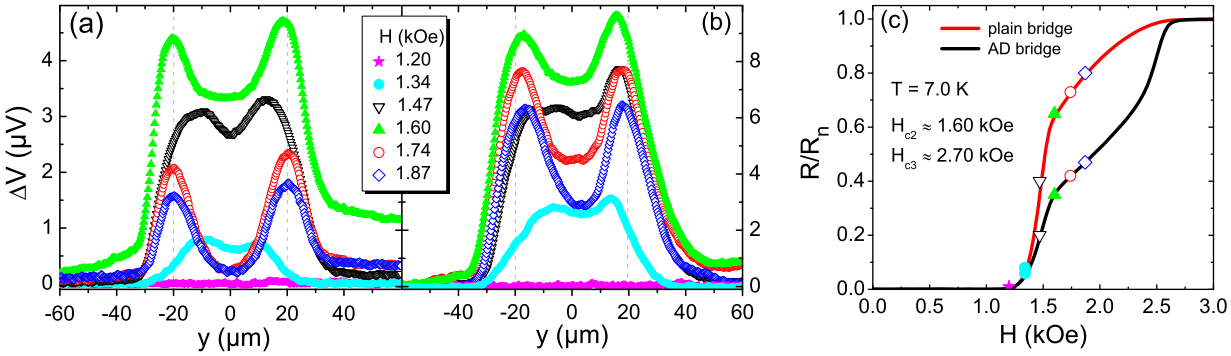

FIG. 6: (Color online) LTSLM linescans $\Delta V(y)$ for variable H at T=7.0 K across (a) the plain and (b) the AD bridge; note the different ΔV scale in (a) and (b). Vertical dashed lines indicate position of the edges of the bridge (c) Corresponding $R(H)$ curves with bias points for the linescans in (a,b).

bridge is higher than for the plain bridge, which we ascribe to the higher current density in the AD bridge due to its reduced cross section because of the holes. For the lowest field value, $H = 1.20$ kOe, the beam-induced heating of the laser has no effect, while at $H = 1.34$ kOe the whole cross section of both bridges leads to a LTSLM signal. As H increases further, the LTSLM signal from the edges becomes larger than the signal from the interior and the overall signal increases up to $H = H_{c2} = 1.60$ kOe. For the plain bridge the overall signal gets strongly reduced above H_{c2}, and the signal from the central part of the bridge almost vanishes. The key difference between the plain and AD bridge is that for the latter sample the voltage signal gets much less reduced and the whole cross section of the AD bridge gives a measurable signal. This

means that the current is distributed across the entire width of the bridge even for $H > H_{c2}$. This observation is consistent with the $R(H)$ measurements shown in Fig. 6(c), where the additional edges inside the AD bridge lead to a different shape in $R(H)$ and a lower R for any value of H within the interval $H_{c2} \lesssim H \lesssim H_{c3}$.

D. Bias-current-induced asymmetry: LTSLM response and Ginzburg-Landau simulations

According to Fig. 5(b,c), the LTSLM signal $\Delta V(y)$ is asymmetric with respect to the bridge center (axis y=0) for several H values around H_{c2}, i.e. the right maximum is slightly higher than the left one. This asymmetry in the beam-induced voltage response can be explained by an asymmetry in the supercurrent density distribution $j_{s,x}(y)$ close to the left and right edge. Based on the time dependent GL model[42], we calculate the time-averaged quantities for the OP distribution $\langle|\psi|^2\rangle(y)$ and the x–components of the superfluid current density $\langle j_{s,x}\rangle(y)$ and the normal current density $\langle j_{n,x}\rangle(y)$.

Figure 7 shows results of such calculations for $H = 1.3\,H_{c2}$ and T/T_{c0}=0.47, which were obtained for zero bias current density $j = j_{s,x} + j_{n,x}$ [Fig. 7(a)], for j close to the critical current density at $H = H_{c2}$ [Fig. 7(b)] and for j which is larger than the critical current density for ES within the entire field range $H_{c2} < H < H_{c3}$ [Fig. 7(c)].

According to our calculations, even in the resistive ES state, there is a finite superfluid flow localized within the ES channels. These supercurrents are circulating in opposite direction within each of the two edge channels, which is due to the applied magnetic field H.

For further analysis, we determined the net currents i_L, i_R and i_n. Here, i_L and i_R are the integrals of $j_{s,x}$ across the left and right edge channel, respectively (shaded areas in Fig. 7); i_n is the integral of $j_{n,x}$ across the entire width of the rectangular film. Hence, for the normalized bias current $i_b \equiv j\frac{W}{\xi_0}$ we have $i_b = i_L + i_R + i_n$.

For $j = 0$ ($i_b = 0$) [cf. Fig.7(a)], the net currents i_L and i_R in the right and left edge channel have the same finite amplitude, but differ in sign, and $i_n = 0$. For $j > 0$ ($i_b > 0$) [cf. Fig.7(b,c)] the steady-state distribution of the superconducting parameters differs from the case $j = 0$. Now, i_L and i_R do have the same (positive) sign, but different amplitudes. Thus, analyzing only the large-scale details in the supercurrent distribution (spatially averaged over length scales much larger than the coherence length ξ_0), one can think in terms of a combination of two parallel currents flowing along the sample edges with different amplitudes depending both on I and H direction. It should be noted that a very similar situation – the asymmetry of the critical current density – was described by Park [20] within a stationary Ginzburg-Landau model. Since the mentioned asymmetry results from the superposition of the bias current I and the currents induced by the applied H field, the asymmetry can therefore being changed either by changing the current direction or the sign of H.

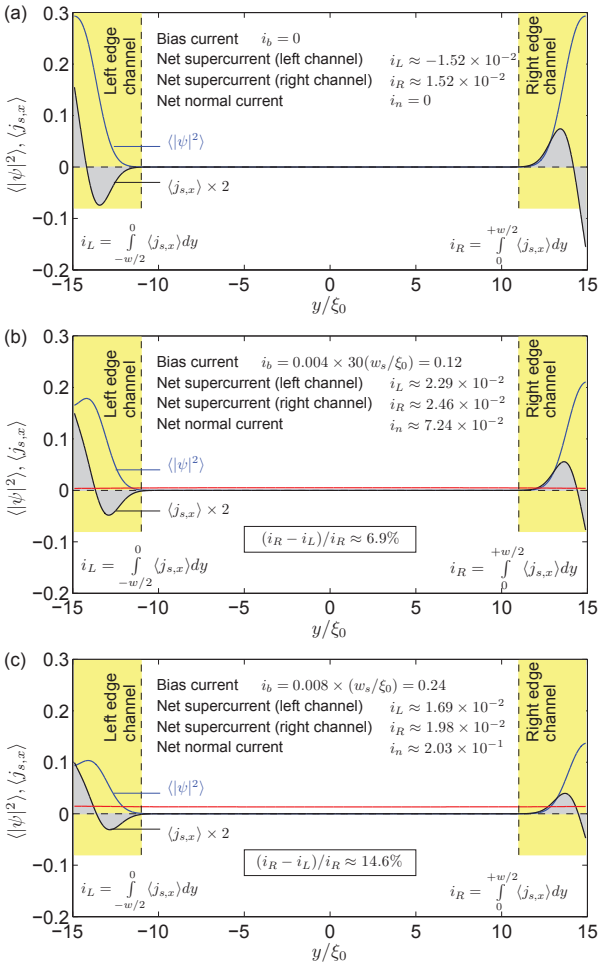

FIG. 7: (Color online) Time-averaged normalized OP wave function $\langle|\psi|^2\rangle(y/\xi_0)$ and x–components of the normalized superfluid current density $\langle j_{s,x}\rangle(y/\xi_0)$ and normalized normal current density $\langle j_{n,x}\rangle(y/\xi_0)$, calculated for a rectangular thin film ($W = 30\,\xi_0$, $L = 60\,\xi_0$; cf. Fig. 3) at T/T_c=0.47 and $H = 1.3H_{c2}$. The three graphs differ in the normalized bias current (a) i_b=0, (b) i_b=0.12 and (c) i_b=0.24. i_L and i_R denote the integrals of $\langle j_{s,x}\rangle$ (shaded areas) over the left and right edge channels, respectively.

In order to prove, whether the asymmetry of the LTSLM signal can be related to the bias-current-induced asymmetry, we calculated the normalized beam-induced voltage $\Delta v(y)$, i.e., linescans across a rectangular superconducting thin film with the geometry as in Fig. 3 and Fig. 7, biased at $j = 4\times10^{-3}$. Details of the calculation can be found in the Appendix. Assuming a Gaussian shape of the laser-beam-induced

increase in T with a maximum amplitude ΔT and a full width half maximum of $\sigma = 7\xi_0$, we obtain the linescan series for different values of H/H_{c2} shown in Fig. 8. These simulations clearly show that the voltage signal has maxima near the left and right edges, and that their amplitudes are different, with this asymmetry being most pronounced at $H = H_{c2}$. This is in nice agreement with experimental LTSLM results.

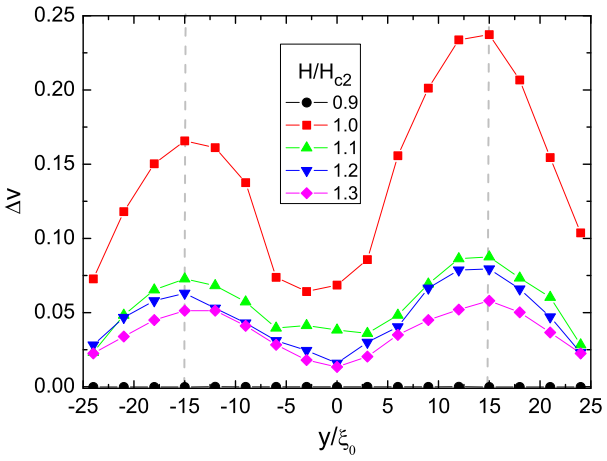

FIG. 8: (Color online) Calculated normalized LTSLM beam-induced voltage Δv=$\bar{v}_{\rm on}$-$\bar{v}_{\rm off}$ vs y/ξ_0 across a rectangular thin film ($W = 30\,\xi_0$, $L = 60\,\xi_0$; cf. Figs. 3 and 7) for different values of H/H_{c2} at T/T_c=0.47 and j=4×10^{-3}. The vertical dashed lines indicate the position of the edges.

To proof experimentally, that the asymmetry depends on sign of H and I, we performed a series of LTSLM linescans on the plain Nb bridge. The reversal of the asymmetry of the measured LTSLM signal upon the inversion of the I and H signs is illustrated in Fig. 9(a) and (b). We find that the right peak is larger for $I > 0$ while the left peak is larger for $I < 0$ and vice versa. The slightly larger amplitudes of the peaks in Fig. 9(b) are probably due to the residual field (in the 10 Oe range) in the cryostat at the sample position. To the best of our knowledge, this is the first direct experimental verification of an asymmetry in the current density in the ES state, as predicted by Park for surface superconductivity.

IV. CONCLUSION

In this paper we studied experimentally and numerically the peculiarities of the resistive transition in thin-film Nb microbridges with and without antidots (ADs) in perpendicular magnetic field H. From integral $R(H)$ measurements we find that the transition from bulk to edge superconductivity (ES), and finally to the full normal state, can be identified by a pronounced change in slope dR/dH, which however strongly depends on the applied bias current density.

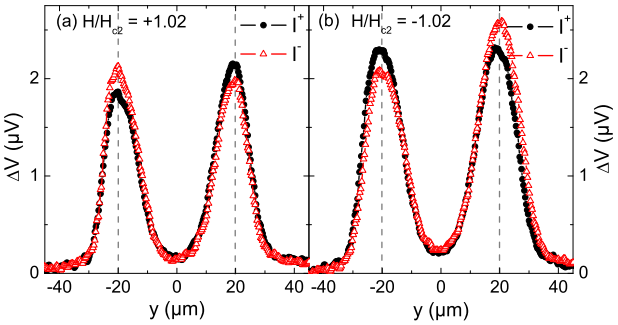

FIG. 9: (Color online) LTSLM linescans $\Delta V(y)$ across the plain Nb bridge (T=7.2 K, H_{c2}=1.37 kOe, $|H|$=1.40 kOe, $|I|$=1 mA) for different sign of I and (a) negative H and (b) positive H. Vertical dashed lines indicate position of the edges of the bridge

The additional edges induced by the holes in the AD bridge lead to a different shape of the $R(H)$ curves as compared to the plain bridge. The ES state as well as the evolution of superconductivity upon sweeping H was imaged by low-temperature scanning laser microscopy (LTSLM). For the ES state, LTSLM revealed an asymmetry in the currents flowing along the left and right edges, depending on the relative direction of applied current and external field, as proposed long time ago[20]. Our calculations based on the time–dependent Ginzburg–Landau theory confirm essential features of the experimental results.

V. ACKNOWLEDGMENT

This work was supported by the Russian Fund for Basic Research, RAS under the Program "Quantum physics of condensed matter", Russian Agency of Education under the Federal Target Program "Scientific and educational personnel of innovative Russia in 2009–2013", Deutsche Forschungsgemeinschaft (DFG) via grant no. KO 1303/8-1. R. Werner acknowledges support by the Cusanuswerk, Bischöfliche Studienförderung, D. Bothner acknowledges support by the Evangelisches Studienwerk Villigst e.V. and M. Kemmler acknowledges support by the Carl-Zeiss Stiftung. The authors thank A. I. Buzdin for valuable discussions.

VI. APPENDIX

In order to describe the general properties of the resistive state in a mesoscopic superconducting thin film sample and to compare them with experiment, we use a simple time–dependent Ginzburg–Landau (TDGL) model.[43] For simplicity we assume that the effect of the superfluid currents on the magnetic field distribution is negligible and consider the internal magnetic

field B equal to the external magnetic field H (perpendicular to the thin film plane). This assumptions seems to be valid for the following two cases; (i) for mesoscopic thin-film superconductors with lateral dimensions smaller than the effective magnetic penetration depth $\Lambda = \lambda^2/d$ (λ_L is the London penetration depth, d is the thickness); (ii) for superconductors for large H and/or T (i.e. close to the phase transition line), when the superfluid density tends to zero. Then the TDGL equations take the form

$$u\left(\frac{\partial}{\partial t}+i\varphi\right)\psi=\tau\left(\psi-|\psi|^2\psi\right)+\left(\nabla+i\mathbf{A}\right)^2\psi, \quad (2)$$

$$\tau=1-T(\mathbf{r})/T_{c0}, \quad (3)$$

$$\nabla^2\varphi=\mathrm{div}\,\boldsymbol{j}_s,\ \boldsymbol{j}_s=-\frac{i}{2}\tau\left\{\psi^*\left(\nabla+i\mathbf{A}\right)\psi-\mathrm{c.c.}\right\}, \quad (4)$$

where ψ is the normalized order parameter (OP), φ is the dimensionless electrical potential, $\boldsymbol{A}$ is the vector potential [$\mathrm{rot}\,\boldsymbol{A}=H\,\hat{\boldsymbol{e}}_z$], $T(\boldsymbol{r})$ is local temperature (potentially position–dependent), $\boldsymbol{j}_s$ is the density of the supercurrent, u is the rate of the OP relaxation, c.c. stands for complex conjugate. We use the following units: $m^*\sigma_n\beta/(2e^2\tilde{\alpha})$ for time, the coherence length ξ_0 at temperature $T=0$ for distances, $\Phi_0/(2\pi\xi_0)$ for the vector potential, $\hbar e|\tilde{\alpha}|/(m^*\sigma_n\beta)$ for the electrical potential, and $4e\tilde{\alpha}^2\xi_0/(\hbar\beta)$ for the current density, where $\alpha=-\tilde{\alpha}\,\tau$ and β are the conventional parameters of the GL expansion, e and m^* are charge and the effective mass of carriers, σ_n is the normal state conductivity. In these units the Ginzburg–Landau deparing current density at $T=0$ is equal to 0.386. We apply the boundary conditions in the following form

$$\left(\frac{\partial}{\partial\boldsymbol{n}}+iA_n\right)_\Gamma\psi=0,\quad\left(\frac{\partial\varphi}{\partial\boldsymbol{n}}\right)_\Gamma=j_{ext}, \quad (5)$$

where $\boldsymbol{n}$ is the normal vector to the sample's boundary Γ, j_{ext} is the normal component of the inward (outward) flow of the bias current density $\boldsymbol{j}$ (with $|\boldsymbol{j}|\equiv j$). We do not consider bulk pinning, since the number of additionally required parameters (describing the spatial distribution of pinning sites and their pinning strength) would be too large.

We calculate[42] the instant value of the normalized voltage drop $v(t)=\langle\varphi_1(t)\rangle-\langle\varphi_2(t)\rangle$ and analyze the dependence of $v(t)$ on H and j_{ext}. Here

$$\langle\varphi_i(t)\rangle=\frac{1}{S_i}\int\int_{S_i}\varphi_i(x,y,t)\,dxdy \quad (6)$$

is the time-dependent electrical potential averaged over the region S_i ("virtual electrodes", $i=\{1,2\}$). These regions have the same width as the sample width and they are shifted from the physical edges towards the sample interior (see Fig. 10) for eliminating the effect of the sample edges. In addition we formally consider an inhomogeneous sample, containing two areas at the left and right edges [cf. Fig. 10] with a critical temperature T_{c1} (at $H=0$) and upper critical field $H^0_{c2,1}$ (at $T=0$) exceeding considerably T_{c0} and H^0_{c2} in the rest of the sample. The reason for that is a pure technical one. This approach guarantees that the injected *normal* current i_b is fully converted into a supercurrent within these enhanced superconducting areas at any temperature and any value of H.

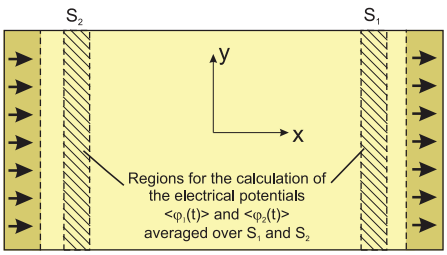

FIG. 10: (Color online) Schematic drawing (top view) of rectangular superconducting thin film bridge considered for GL simulations. Arrows indicate injection and extraction of the bias current. Shaded areas S_1 and S_2 are virtual electrodes.

For the stationary regime all the calculated parameters, after transient processes induced by changes in the external parameters, tend to their time–independent values, pointing out to the absence of energy dissipation for the established state and $R\to 0$. For larger T, H or i_b the relaxation to the stationary case becomes impossible and all parameters oscillate in time. Calculating the mean normalized voltage drop $\bar{v}$, averaged over a very large time interval (including up to 10^2 of the voltage oscillations), one can determine the normalized beam–induced LTSLM voltage signal $\Delta v=\bar{v}_{\mathrm{on}}-\bar{v}_{\mathrm{off}}$, where $\bar{v}_{\mathrm{on}}$ and $\bar{v}_{\mathrm{off}}$ are the time averaged normalized voltage signals if the laser beam is on or off, respectively.

The effect of the focused laser beam can be treated as a quasistatic perturbation of the superconducting properties of the bridge, since the time scales of this perturbation are much longer than the GL time constant. In the most simple form this perturbation can be modelled as a Gaussian–like increase in local temperature in Eq. (3):

$$T(\mathbf{r})=T_0+\Delta T\cdot e^{[-(x-x_0)^2-(y-y_0)^2]/\sigma^2}. \quad (7)$$

Here, T_0 is the sample temperature if the laser beam is off or far from the beam spot centered at (x_0,y_0), ΔT is the amplitude of the local heating, depending on the beam intensity and on the rate of heat dissipation due to the thermal conductivity of the superconducting film and the substrate and on the thermal boundary resistance between the film and the substrate; σ is the full width half maximum of the beam–induced temperature profile.[44]

[1] D. Saint-James and P. G. de Gennes, Phys. Lett. **7**, 306 (1963).
[2] A. A. Abrikosov, Fundamentals of the Theory of Metals (Elsevier Science Ltd, 1988).
[3] M. Tinkham, Introduction to superconductivity (McGraw-Hill Inc., 1996), 2nd ed.
[4] C. F. Hempstead and Y. B. Kim, Phys. Rev. Lett. **12**, 6 (1964).
[5] F. T. J. Smith and H. C. Gatos, J. Appl. Phys. **39**, 3793 (1968).
[6] A. Rothwarf, J. I. Gittleman, and B. Rosenblum, Phys. Rev. **155**, 370 (1967).
[7] J. Kirschenbaum, Phys. Rev. B **12**, 3690 (1975).
[8] M. Strongin, A. Paskin, D. G. Schweitzer, O. F. Kammerer, and P. P. Craig, Phys. Rev. Lett. **12**, 442 (1964).
[9] F. de la Cruz, M. D. Maloney, and M. Cardona, Phys. Rev. **187**, 766 (1969).
[10] R. W. Rollins, R. L. Cappelletti, and J. H. Fearday, Phys. Rev. B **2**, 105 (1970).
[11] J. R. Hopkins and D. K. Finnemore, Phys. Rev. B **9**, 108 (1974).
[12] D. G. Schweitzer and B. Bertman, Phys. Rev. **152**, 293 (1966).
[13] J. P. McEvoy, D. P. Jones, and J. G. Park, Phys. Rev. Lett. **22**, 229 (1969).
[14] Y. Brunet, P. Monceau, and G. Waysand, Phys. Rev. B **10**, 1927 (1974).
[15] M. Strongin, A. Paskin, O. F. Kammerer, and M. Garber, Phys. Rev. Lett. **14**, 362 (1965).
[16] A. A. Abrikosov, Soviet Phys. JETP **20**, 480 (1965).
[17] R. V. Bellau, Physics Letters **21**, 13 (1966).
[18] R. V. Bellau, Proc. Phys. Soc. **91**, 144 (1967).
[19] J. Lowell, J. Phys. C (Solid St. Phys.) **2**, 372 (1969).
[20] J. G. Park, Phys. Rev. Lett. **15**, 352 (1965).
[21] R. H. White, Phys. Rev. **142**, 241 (1966).
[22] A. Bezryadin and B. Pannetier, J. Low Temp. Phys. **98**, 251 (1995).
[23] A. Bezryadin and B. Pannetier, Physica Scripta **T66**, 225 (1996).
[24] J. Berger and J. Rubinstein, Connectivity and Superconductivity (Springer Verlag, 2000).
[25] L. F. Chibotaru, A. Ceulemans, M. Morelle, G. Teniers, C. Carballeira, and V. V. Moshchalkov, J. Math. Phys. **46**, 095108 (2005).
[26] A. Y. Aladyshkin, D. A. Ryzhov, A. V. Samokhvalov, D. A. Savinov, A. S. Melnikov, and V. V. Moshchalkov, Phys. Rev. B **75**, 184519 (2007).
[27] J. Kirschenbaum and Y.-H. Kao, Phys. Rev. Lett. **22**, 1177 (1969).
[28] M. I. Tsindlekht, G. I. Leviev, V. M. Genkin, I. Felner, P. Mikheenko, and J. S. Abell, Phys. Rev. B **74**, 132506 (2006).
[29] G. Fischer, Phys. Rev. Lett. **20**, 268 (1968).
[30] N. Keller, J. L. Tholence, A. Huxley, and J. Flouquet, Phys. Rev. B **54**, 13188 (1996).
[31] G. D'Anna, P. L. Gammel, A. P. Ramirez, U. Yaron, C. S. Oglesby, E. Bucher, and D. J. Bishop, Phys. Rev. B **54**, 6583 (1996).
[32] D. Stamopoulos, M. Pissas, V. Karanasos, D. Niarchos, and I. Panagiotopoulos, Phys. Rev. B **70**, 054512 (2004).
[33] J. Scola, A. Pautrat, C. Goupil, L. Méchin, V. Hardy, and C. Simon, Phys. Rev. B **72**, 012507 (2005).
[34] Y. X. Ning, C. L. Song, Z. L. Guan, X. C. Ma, X. Chen, J. F. Jia, and Q. K. Xue, Europhys. Lett. **85**, 27004 (2009).
[35] A. I. Buzdin and A. S. Mel'nikov, Phys. Rev. B **67**, 020503(R) (2003).
[36] A. Y. Aladyshkin, A. I. Buzdin, A. A. Fraerman, A. S. Mel'nikov, D. A. Ryzhov, and A. V. Sokolov, Phys. Rev. B **68**, 184508 (2003).
[37] Z. R. Yang, M. Lange, A. Volodin, R. Szymczak, and V. V. Moshchalkov, Nature Mater. **3**, 793 (2004).
[38] R. Werner, A. Y. Aladyshkin, S. Guénon, J. Fritzsche, I. M. Nefedov, V. V. Moshchalkov, R. Kleiner, and D. Koelle, Phys. Rev. B **84**, 020505(R) (2011).
[39] M. Wagenknecht, H. Eitel, T. Nachtrab, J. B. Philipp, R. Gross, R. Kleiner, and D. Koelle, Phys. Rev. Lett. **96**, 047203 (2006).
[40] H. B. Wang, S. Guénon, J. Yuan, A. Iishi, S. Arisawa, T. Hatano, T. Yamashita, D. Koelle, and R. Kleiner, Phys. Rev. Lett. **102**, 017006 (2009).
[41] A. Y. Aladyshkin, J. Fritzsche, R. Werner, R. B. G. Kramer, S. Guénon, R. Kleiner, D. Koelle, and V. V. Moshchalkov, Phys. Rev. B **84**, 094523 (2011).
[42] The described simulations were performed using the Windows–oriented solver GLDD, developed in the Institute for Physics of Microstructures RAS.
[43] B. I. Ivlev and N. B. Kopnin, Usp. Fiz. Nauk **142**, 435 (1984).
[44] R. Gross and D. Koelle, Rep. Prog. Phys. **57**, 651 (1994).

Publication IV

$YBa_2Cu_3O_7/La_{0.7}Ca_{0.3}MnO_3$ bilayers: Interface coupling and electric transport properties

R. Werner,[1] C. Raisch,[2] A. Ruosi,[3] B. A. Davidson,[4] P. Nagel,[5] M. Merz,[5] S. Schuppler,[5] M. Glaser,[2] J. Fujii,[4] T. Chassé,[2] R. Kleiner,[1] and D. Koelle[1,*]

[1]*Physikalisches Institut-Experimentalphysik II, Universität Tübingen, Auf der Morgenstelle 14, 72076 Tübingen, Germany*

[2]*Physikalische Chemie, Universität Tübingen, Auf der Morgenstelle 18, 72076 Tübingen, Germany*

[3]*Department of Physics, University of Naples Federico II, P.Tecchio 80, 80125 Naples, Italy*

[4]*CNR-IOM, TASC National Laboratory, S.S. 14 Km 163.5 in AREA Science Park, 34012 Basovizza, Trieste, Italy*

[5]*Institut für Festkörperphysik, Forschungszentrum Karlsruhe, D-76021 Karlsruhe, Germany*

(Received 10 September 2010; revised manuscript received 17 November 2010; published 10 December 2010)

Heteroepitaxially grown bilayers of ferromagnetic $La_{0.7}Ca_{0.3}MnO_3$ (LCMO) on top of superconducting $YBa_2Cu_3O_7$ (YBCO) thin films were investigated by focusing on electric transport properties as well as on magnetism and orbital occupation at the interface. Transport measurements on YBCO single layers and on YBCO/LCMO bilayers, with different YBCO thickness d_Y and constant LCMO thickness $d_L=50$ nm, show a significant reduction in the superconducting transition temperature T_c only for $d_Y<10$ nm, with only a slightly stronger T_c suppression in the bilayers, as compared to the single layers. X-ray magnetic circular dichroism measurements confirm recently published data of an induced magnetic moment on the interfacial Cu by the ferromagnetically ordered Mn ions, with antiparallel alignment between Cu and Mn moments. However, we observe a significantly larger Cu moment than previously reported, indicating stronger coupling between Cu and Mn at the interface. This in turn could result in an interface with lower transparency, and hence smaller spin-diffusion length, that would explain our electric transport data, i.e., smaller T_c suppression. Moreover, linear dichroism measurements did not show any evidence for orbital reconstruction at the interface, indicating that a large change in orbital occupancies through hybridization is not necessary to induce a measurable ferromagnetic moment on the Cu atoms.

DOI: 10.1103/PhysRevB.82.224509 PACS number(s): 78.70.Dm, 73.40.−c, 74.72.−h, 75.47.Lx

I. INTRODUCTION

Singlet superconductivity and ferromagnetism do not usually coexist in bulk compounds, as the exchange field in the ferromagnet favors an alignment of the conduction-electron spins in the same direction, preventing the pairing effect in Cooper pairs formed by electrons with antiparallel spin. However, the combination of superconducting (S) and ferromagnetic (F) materials in artificial thin layered systems, gives the unique opportunity to investigate the interplay between these two competing long-range order phenomena. In such SF hybrid devices, superconducting correlations may be established in the ferromagnet due to the proximity effect, allowing superconductivity and ferromagnetism to coexist within a short distance from the interface on the order of the induced superconducting correlation length, ξ_F.[1–3] Simultaneously, the exchange field causes pair breaking in the superconductor, weakening or even suppressing the superconducting order parameter, and inducing a local magnetic moment in the superconductor at a distance from the SF interface set by the superconducting coherence length ξ_S. Magnetic ordering is generally more robust than superconductivity (the exchange energy in ferromagnets is typically 1 eV while the Cooper pair formation energy is 0.01 eV), and for materials having a strong exchange field, magnetism may be unperturbed by the proximity of a superconductor.

While SF hybrid structures based on metallic ferromagnets and conventional superconductors have been investigated in detail,[1] there are much less studies on SF systems involving high-transition temperature cuprate superconductors characterized by a very short coherence length and an anisotropic superconducting gap. In this context, half metallic rare-earth manganites such as $La_{0.7}M_{0.3}MnO_3$ (M=Ca,Sr,Ba) are ideal ferromagnets, as they are nearly perfectly in-plane lattice matched with cuprates, which enables heteroepitaxial growth of cuprate/manganite SF bilayers (BLs) and superlattices with well-defined interfaces.[4,5] In particular, $YBa_2Cu_3O_7/La_{0.7}Ca_{0.3}MnO_3$ (YBCO/LCMO) superlattices have allowed the study of novel phenomena, such as a long-range proximity effect,[6,7] spin-polarized quasiparticle injection into the S layer within a spin-diffusion length ξ_{FM},[8] giant magnetoresistance,[9] and a giant modulation of the F-layer magnetization induced by superconductivity.[10]

Recently, interfacial properties in YBCO/LCMO superlattices were investigated by x-ray magnetic circular dichroism (XMCD) (Ref. 11) and x-ray linear dichroism (XLD).[12] These studies revealed an induced ferromagnetic moment on the interfacial Cu, oriented antiparallel to the adjacent Mn, whose temperature dependence follows that of the Mn moment. The authors suggest that Cu and Mn are coupled across the interface by covalent chemical bonding that results in strong hybridization and large rearrangements of the orbital occupancies (orbital "reconstruction"). Within this context, the Mn-O-Cu superexchange interaction explains the induced magnetic moment in the cuprate and the presence of a nonsuperconducting YBCO layer at the interface.

Here, we present a detailed investigation of YBCO/LCMO bilayers, focusing on the dependence of transport properties on the YBCO layer thickness as well as on the interface coupling on an atomic length scale. Transport measurements indicate high-quality bilayers, showing a reduction in the superconducting transition temperature T_c only

below a YBCO thickness of ≈10 unit cells (uc's). Dichroism measurements using synchrotron radiation have been used to probe magnetic order and orbital occupations on both sides of the YBCO/LCMO interface by tuning the photon energy to Cu or Mn absorption resonances. The XMCD measurements confirm the induction of a small net magnetic moment on Cu that vanishes near the Curie temperature of the LCMO. Dichroism measurements with linearly polarized light show no evidence of any significant difference between the 3*d* orbital occupations in the interfacial Cu as compared to the Cu in the bulk YBCO. This implies that an induced magnetic moment on Cu through hybridization at the interface with Mn can result *without* any accompanying "orbital reconstruction."

II. EXPERIMENTAL DETAILS

Commercially available stoichiometric polycrystalline YBCO and LCMO targets were used for epitaxial growth of YBCO and LCMO thin films (with thickness d_Y and d_L, respectively) and YBCO/LCMO bilayers by pulsed laser deposition on (001) $SrTiO_3$ (STO) substrates. The targets were ablated by using a KrF ($\lambda=248$ nm) excimer laser at a repetition rate of 2 Hz.[13] The substrate temperature T_s during deposition was 750 °C for all films for which data are presented below. The oxygen pressure p_{O_2} during thin-film growth was 20 Pa. After thin-film deposition, the chamber was immediately vented with oxygen, and the samples were cooled down to $T_s=550$ °C in $p_{O_2}\approx 1$ mbar and annealed for $t=1$ h to obtain fully oxidized films. The cooling process was started right after the deposition to minimize interdiffusion at the bilayer interfaces. For all bilayers shown here, YBCO was grown directly on STO and covered by LCMO.

In situ high-pressure reflection high-energy electron diffraction was used to monitor the growth mode and the exact number of deposited monolayers. The surface morphology was checked by atomic force microscopy (AFM) in contact mode and the crystal structure was characterized by x-ray diffraction (XRD). The thin-film resistance R was measured by a Van der Pauw method on unpatterned films in a temperature range of $T=10-300$ K in order to determine the superconducting transition temperature T_c of the YBCO films or the metal-to-insulator transition temperature T_{MI} of the LCMO films. Here, we define T_{MI} as the temperature for which $R(T)$ shows a maximum, which is typically within a few kelvins of the ferromagnetic transition temperature T_{Curie} in LCMO. A superconducting quantum interference device (SQUID) magnetometer was used to characterize the magnetic and superconducting properties of the samples by measuring magnetization $M(T)$ from $T=10$ to 250 K in order to obtain T_c of the YBCO films and T_{Curie} of the LCMO films.

In order to obtain site- and element-specific information regarding the local electronic structure (orbital occupation) and magnetic properties of YBCO/LCMO bilayers, we performed x-ray absorption spectroscopy (XAS), which is the absorption of an x-ray photon and the excitation of a core-level electron into an unoccupied state through the electric dipole transition. These experiments were performed at the high-energy branch of the advanced photoelectric effect (APE) beamline located at the ELETTRA storage ring in Trieste[14] and at the soft x-ray beamline WERA at the Angströmquelle Karlsruhe (ANKA). All XAS data shown below (Secs. V and VI) were obtained from the same YBCO/LCMO bilayer and are representative of all samples measured. This consists of a thin capping layer of 13 uc LCMO ($d_L\approx 5.2$ nm), which was grown on top of a thicker layer of YBCO of about 18 uc ($d_Y=20$ nm).

The XAS data were recorded in surface-sensitive total electron yield (TEY) mode and in bulk-sensitive fluorescent yield (FY) mode. In TEY mode, we probe predominantly interfacial Cu within the YBCO/LCMO bilayer. Due to the small electron escape depth at the Mn or Cu L edge energies (≈2 nm), most (>90%) of the signal comes from within 6–8 nm of the surface (and is dominated by the 5 nm overlayer of LCMO). Circularly polarized synchrotron radiation was used for measuring soft x-ray absorption spectra of the Cu and Mn $L_{2,3}$ ($2p\Rightarrow 3d$ transition) absorption edges in TEY mode on the YBCO/LCMO bilayer. At APE, a fixed photon-sample geometry was used (30° incident angle of light with respect to the film plane) and polarization (circular, linear) was changed at the undulator located in the storage ring. At WERA, the photon polarization was chosen by adjusting the exit slits after the bending magnet and was therefore fixed. For the linear dichroism measurements, the electric field vector was aligned in the film plane or along the surface normal by changing the orientation of the sample normal. The XAS spectra are normalized to equal step heights beyond ionization threshold. XMCD spectra have been corrected for the incomplete photon polarization (90%) and the 30° incident angle at APE. Geometrical corrections for LD spectra taken at WERA have been made. We define the XMCD signal (for a given energy) as the difference of the XAS signals (normalized to their average value) with incident light helicity oriented, respectively, parallel and antiparallel to the magnetization. The XMCD measurements at APE were always measured in remanence, after applying around ±60 mT in the film plane at 30° incidence angle with respect to the photon helicity. We further recorded XLD data in both TEY and FY mode (in plane or out of plane with respect to the sample surface). The XLD signal is defined as out-of-plane minus in-plane XAS normalized to in-plane XAS intensity.

III. THIN-FILM CHARACTERIZATION

Figure 1 shows typical AFM measurements for LCMO and YBCO films ($d_Y=d_L=50$ nm). In the case of LCMO [cf. Fig. 1(a)], the monolayer steps of the substrate are transmitted to the LCMO thin film. The films are atomically flat with a root-mean-square (rms) roughness of 0.2 nm, determined over the scan area 5×5 μm^2 shown in Fig. 1. The case of the YBCO [cf. Fig. 1(b)] is different, because YBCO grown on STO relaxes after a few monolayers, due to the larger lattice mismatch, and starts to grow in a three-dimensional mode. The rms roughness of the shown YBCO film is 0.8 nm.

Figure 2 shows XRD data [$\Theta-2\Theta$ scans in the main graph and ω scans (rocking curves) in the inset] of a single-

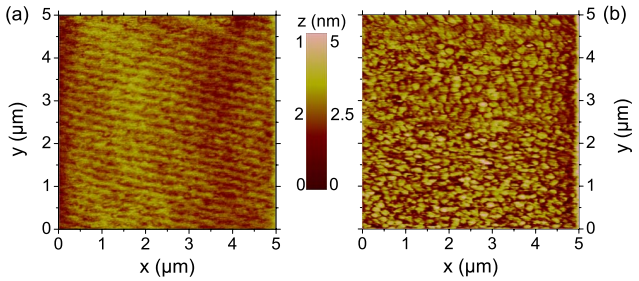

FIG. 1. (Color online) (a) AFM images of LCMO film surface (d_L=50 nm) with an rms roughness of 0.2 nm and (b) YBCO film surface (d_Y=50 nm) with an rms roughness of 0.8 nm. Numbers left and right from color bar refer to (a) and (b), respectively.

layer (SL) YBCO (d_Y=10 nm) and LCMO (d_L=50 nm) film and a YBCO/LCMO (20 nm/50 nm) bilayer. All samples are single phase and c axis oriented. Bulk YBCO has lattice constants a=3.817 Å, b=3.883 Å, and c=11.682 Å. YBCO films grown on STO under optimized conditions relax their in-plane lattice constants within the first unit cells to the bulk values. Bulk LCMO is orthorhombic, with pseudocubic lattice parameters a=3.868 Å, b=3.858 Å, and c=3.856 Å. LCMO thin films grown on STO substrates or YBCO films grow fully strained for thicknesses up to d_L =50 nm. For LCMO films grown on STO this strain is tensile so that the out-of-plane lattice constant of the LCMO is decreased while LCMO grown on YBCO is under slight compressive strain. Due to the different lattice mismatch between YBCO/LCMO and STO/LCMO, the LCMO (00ℓ) peaks for the bilayer are shifted to smaller angles, as compared to the LCMO single layer, depending on the transmitted strain. The low lattice mismatch between YBCO and LCMO (0.3% in plane), results in an excellent epitaxial growth of the bilayers. This is confirmed by rocking curves around the (002) peak of LCMO and the (005) peak of YBCO, which yield almost the same values for SL and BL films.

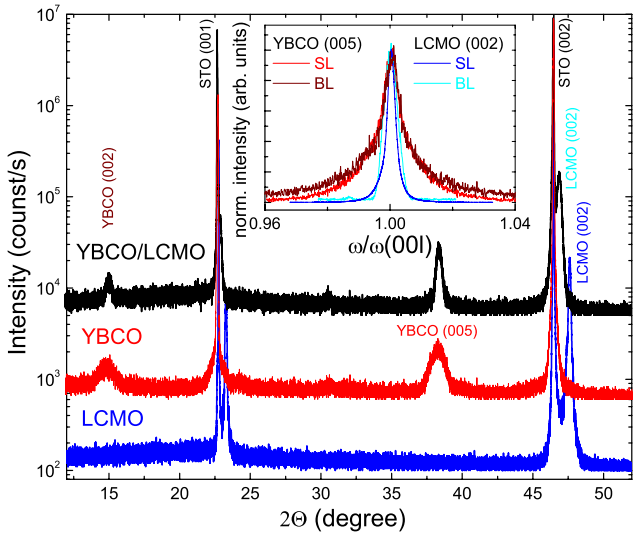

FIG. 2. (Color online) XRD data for a single layer YBCO (d_Y =10 nm) and LCMO (d_L=50 nm) film and for a YBCO/LCMO bilayer (d_Y=20 nm and d_L=50 nm). The main graph shows Θ −2Θ scans (for YBCO and YBCO/LCMO shifted vertically for clarity). The inset shows a comparison of rocking curves around the YBCO (005) and LCMO (002) peaks for the SLs and the BLs, with full width half maximum $\Delta\omega$=0.05° and 0.06° for LCMO in the SL and BL and 0.10° and 0.11° for YBCO in the SL and BL, respectively.

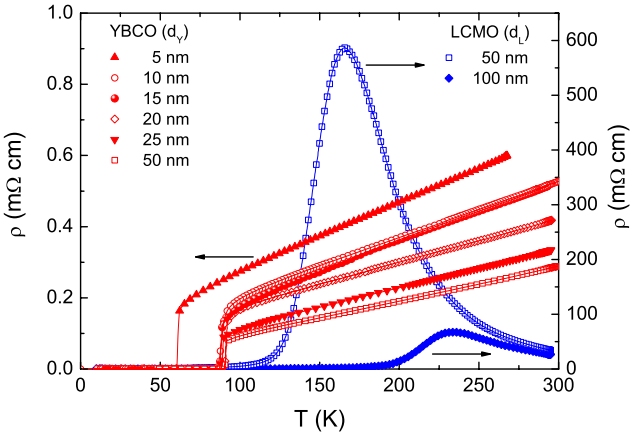

FIG. 3. (Color online) Resistivity ρ vs temperature T of YBCO and LCMO single-layer films with thicknesses d_Y and d_L, respectively.

IV. ELECTRIC TRANSPORT PROPERTIES

In this section, we present and discuss results obtained on electric transport properties of YBCO/LCMO bilayers and compare those with the properties of single layer YBCO and LCMO films.

A. YBCO and LCMO single layers

Figure 3 shows resistivity ρ vs temperature T for six YBCO single-layer films with d_Y=5–50 nm and for two LCMO single-layer films with d_L=50 and 100 nm. The metal-to-insulator transition temperature of the LCMO films is $T_{MI}\approx$166 K (for d_L=50 nm) and ≈235 K (for d_L =100 nm). The T_{MI} values depend on the oxygen content that influences the carrier density and on film strain that changes the strength of the double exchange interaction.[15] XRD reciprocal space mapping (not shown here) shows that the 50 nm LCMO film is coherently strained and therefore does not reach the bulk value of T_{Curie}=260 K while the 100 nm LCMO film is relaxed and shows a much larger T_{MI} and a much smaller $\rho(T=T_{MI})$. The superconducting transition temperature T_c of the YBCO thin films is $T_c\approx$85–90 K for all films, except for the thinnest one [for $T_c(d_Y)$ see Fig. 4(b)], and the normal-state resistivity ρ increases with decreasing d_Y. The room-temperature resistivity is ρ_L ≈30 mΩ cm and $\rho_Y\approx$0.3–0.6 mΩ cm for the LCMO and YBCO films, respectively, i.e., ρ differs by up to two orders of magnitude at room temperature.

B. YBCO/LCMO bilayers

We prepared bilayers with d_L=50 nm and d_Y =5–50 nm; in all bilayers, YBCO was grown first and cov-

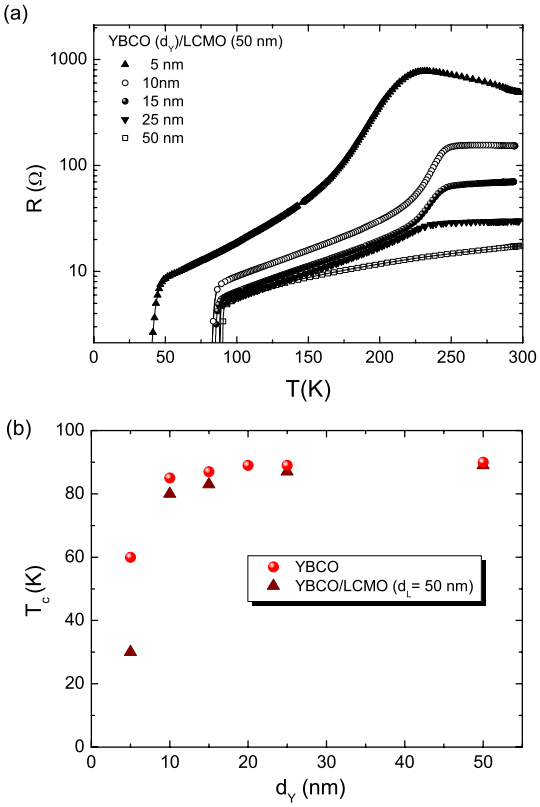

FIG. 4. (Color online) (a) Resistance R vs temperature T of YBCO/LCMO bilayers with d_L=50 nm thick LCMO and different YBCO thickness d_Y. (b) Superconducting transition temperature T_c vs YBCO thickness d_Y for YBCO single layers and for YBCO/LCMO bilayers obtained from the $R(T)$ data shown in (a) and in Fig. 3.

ered by LCMO. The $R(T)$ dependence of five YBCO/LCMO bilayers with fixed d_L=50 nm and variable d_Y is shown in Fig. 4(a). The signature of T_{MI} is visible for all bilayers shown here, except for the one with the thickest YBCO layer. While this is most clear for the sample with the thinnest YBCO layer, it gets less pronounced once d_Y is increased, due to decreasing YBCO resistance. We note that shunting of the LCMO resistance by the YBCO layer cannot account for a shift in position of the observed maximum or kinks in the bilayer $R(T)$ curves to higher temperatures, i.e., within the bilayers, T_{MI} of the LCMO film is significantly higher (around 230–240 K) as compared to the single layer LCMO film with same thickness d_L=50 nm (cf. Fig. 3). This can be attributed to the release of strain, either by exceeding the critical thickness (≈50 nm) of LCMO on STO or by growing on a YBCO template, which is known to increase T_{MI} and to reduce the resistivity of LCMO films.[16–19]

The suppression of T_c with decreasing d_Y is shown in Fig. 4(b), both for YBCO single layers and YBCO/LCMO bilayers. In both cases a significant suppression of T_c is only observed for d_Y=5 nm, and only for this smallest thickness we do observe a clear difference in T_c between single-layer and bilayer samples. We note that this observation is in contrast to Ref. 8, where a drop in $T_c(d_Y)$ of YBCO/LCMO bilayers was found for $d_Y \lesssim 30$ nm. The T_c suppression observed for only very small d_Y might indicate a smaller spin-diffusion length of spin-polarized electrons into YBCO as compared to the one derived from $T_c(d_Y)$ data in Ref. 8. One possible explanation for this is a stronger interaction between the Cu and Mn moments at the interface for our samples. The stronger hybridization could give rise to an electronically less-transparent interface (F/I/S, where I indicates insulating) that blocks injection of spin-polarized electrons. To our knowledge, there has been no theoretical study of the electronic structure of the ferromagnetic YBCO layers for different strengths of hybridization. In order to shed more light on this, we performed XAS measurements, which will be described below.

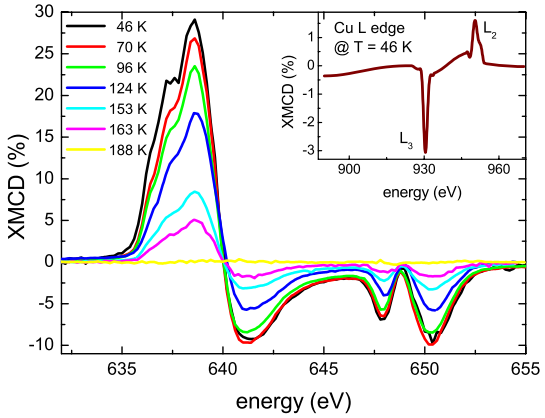

FIG. 5. (Color online) XMCD spectra at the Mn L_3 edge for different T from the YBCO/LCMO bilayer (d_Y=20 nm and d_L=5.2 nm). The maximum dichroic signal is 29% at low T and decreases as T approaches T_{Curie}. The inset shows the XMCD signal at the Cu L edge with a maximum of 3.0% at T=46 K, revealing antiferromagnetic coupling to the Mn magnetic moments. As the Cu XAS signal is one order of magnitude smaller than for Mn, and as Cu dichroism is another order of magnitude smaller, we had to average over many scans and do a careful smoothing of the data. Kinks in the signal arise from switching between different step sizes near the L_3 and L_2 edges.

V. INTERFACE SPECTROSCOPY AND PROXIMITY EFFECT

In the following two sections, we discuss XAS data obtained from the YBCO/LCMO bilayer with thicknesses d_Y=20 nm and d_L=5.2 nm. Magnetization measurements $M(T)$ for this sample yielded $T_c \approx 80$ K for the YBCO film and $T_{Curie} \approx 200$ K for the LCMO film within the bilayer. Figure 5 shows XMCD spectra at the manganese $L_{2,3}$ edge (≈640 eV) for different temperatures. The shape of the spectra is typical for manganese atoms in a mixed Mn^{3+}/Mn^{4+} oxidation state.[20] The strong multiplet broadening of the Mn L_3 peak is a consequence of the partial occupation of the five Mn d orbitals. The dichroism peak height at the L_3 edge (638 eV) at T=46 K is 29%. The inset shows the XMCD signal at the Cu L edge with the L_3 and L_2 peaks at 931 eV and 951 eV, respectively, at the same temperature. The nonzero XMCD signal indicates a ferromagnetic ordering of the Cu moments. In addition, the opposite sign of Mn

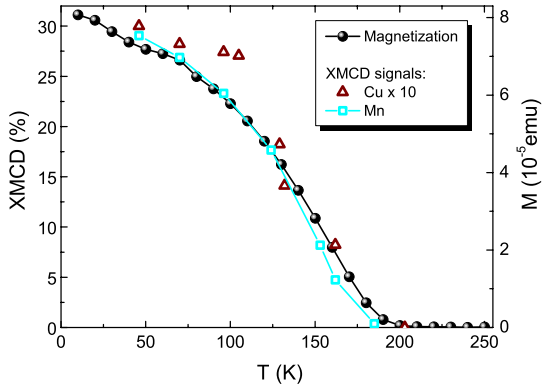

FIG. 6. (Color online) Evolution of magnetic moments with temperature for YBCO/LCMO bilayer. The comparison of XMCD signals (magnetic moments) at the Cu sites (open triangles) and the Mn sites (open squares) as well as bulk magnetization from SQUID measurements (black dots; field cooled in 10 mT) show the same behavior. The Cu dichroism signal is scaled by a factor of 10.

and Cu dichroism reveals an antiparallel coupling between LCMO and YBCO across the heterostructure interface.

The maximum magnitude of the dichroism at the Cu L_3 edge at $T=46$ K of about 3.0% is higher than the value of 1.4% reported in Ref. 11 at $T=30$ K. However, it is in good agreement with theory,[21] predicting 2.4% XMCD for $YBCO/La_{1-x}Ca_xMnO_3$ interfaces in which a single unit cell of YBCO is included in their model. This demonstrates that the proximity to ferromagnetically ordered Mn spins induces spin canting in the Cu atoms of YBCO. According to Ref. 21, the presence of the ferromagnet leads to exchange splitting of the Cu d shell, resulting in spin-polarized states. The hybridization at the interface of Cu d_{3z^2} with spin-split Mn d_{3z^2} states via O p_z in the BaO layer [for an interface formed by adjacent layers of BaO and MnO_2 (Refs. 4 and 5)] then creates a slightly larger amount of holes in the majority than in the minority spin Cu d_{3z^2} bands. This produces a small net moment on the Cu sites. Superexchange interactions determine the antiferromagnetic orientation of the Cu moment with respect to Mn. In this model, the number of excess d_{3z^2}-derived majority states from the hybridization is small, sufficient for producing a measurable interfacial Cu XMCD signal but not enough to modify the orbital occupancies that determine the experimentally measured linear dichroism. This is in agreement with the LD measurements on our samples (as discussed in Sec. VI).

Figure 6 shows a comparison of the temperature dependence of XMCD signals and bulk magnetization M obtained from SQUID measurements. XMCD measured at the Mn L_3 edge is in good agreement with $M(T)$ from SQUID measurements, which yields $T_{\mathrm{Curie}}=200$ K. The intensity of dichroism at the Cu L_3 edge (multiplied by a factor of 10) also decreases with increasing temperature until the signal becomes lower than a detectable threshold at $T=188$ K. The magnetic behavior of Cu closely follows the temperature dependence of the LCMO layer, persisting up to T_{Curie}. This supports the interpretation of induced ferromagnetism in YBCO across the YBCO/LCMO interface. From sum-rule calculations,[22] that relate the spin and orbital magnetic moments m_S and m_l, respectively, to the areas of the L_2 and L_3 peaks, at low temperature we find $m_S=0.1\ \mu_B/\mathrm{Cu}$ to within an error of 20%, and $m_l<0.03\ \mu_B/\mathrm{Cu}$ in remanence. If the Cu moment is concentrated at the interface, the actual moment on the Cu atoms near the interface would be higher. Depending on the assumed profile, this could imply an actual Cu moment higher by a factor of 2 or 3. For a single hole $3d$ ground state ($2p^6$-$3d^9$) and a closed $3d$ shell final state ($2p^5$-$3d^{10}$) system these sum-rule calculations are precise to within 5–10 %.[23] Strong multiplet effects at the Mn L edge prevent a detailed analysis of manganese spin and orbital moments for this mixed Mn^{3+}/Mn^{4+} system.

VI. ORBITAL OCCUPATION

In order to investigate the occupation of valence-electron orbitals on copper and manganese atoms we measured XLD in surface-sensitive TEY and bulk-sensitive FY detection mode on the YBCO/LCMO bilayer. We were specifically interested in the orbital reconstruction proposed in Ref. 12, where a large XLD signal in bulk YBCO but no XLD signal for YBCO in proximity to LCMO was reported. The authors proposed orbital reconstruction to explain the almost identical occupation of in-plane and out-of-plane d-band states at the YBCO/LCMO interface. However, in Ref. 21 it is noted that hybridization between Cu and Mn at the interface, responsible for a measurable XMCD on Cu, should not change the orbital occupations enough in either Cu (or Mn) interfacial layers to change the experimental XLD from their bulk values. For interfacial Cu, then, the number of holes created in the d_{3z^2} orbitals by hybridization is still much smaller than the number of holes in the $d_{x^2-y^2}$ orbital, leading to a strong negative XLD in the interfacial region as well as in the bulk.

In fact we found a strong XLD signal at the Cu L edge [see Fig. 7(a) and inset in Fig. 8] in TEY mode, 48% at $T=25$ K at ANKA and 40% at $T=46$ K at ELETTRA (not shown here). Moreover we do not observe any appreciable differences between bulk-sensitive FY detection [42% XLD signal at $T=100$ K, cf. Fig. 7(c)] and interface-sensitive TEY detection [cf. Figs. 7(b) and 7(c)], neither in shape nor in energy. The shift in the XA edge energy of 0.4 eV toward higher binding energy with increasing information depth, which was attributed to a charge-transfer effect in Ref. 12 could not be reproduced.

These results are evidence that it is possible to induce a sizeable magnetic moment on Cu across the interface without covalent bonding that drastically changes the orbital occupancies, as previously proposed. From our XLD data we can place an upper limit of $\leq 15\%$ on any changes in the orbital occupations relative to the bulk, if we assume that the ratio of the thickness of the "reconstructed" interfacial region to the probing depth in TEY mode is ≈ 0.4. This is reasonable if we assume that the interfacial region extends 1–2 unit cells into the YBCO, and the probing depth is between 2 and 5 nm.[24,25]

The third piece of information obtained from linear dichroism is the temperature independence of orbital occupation. Comparison between TEY data at $T=25$ K [Fig. 7(a)] and $T=200$ K [Fig. 7(b)] show no difference in XLD signal.

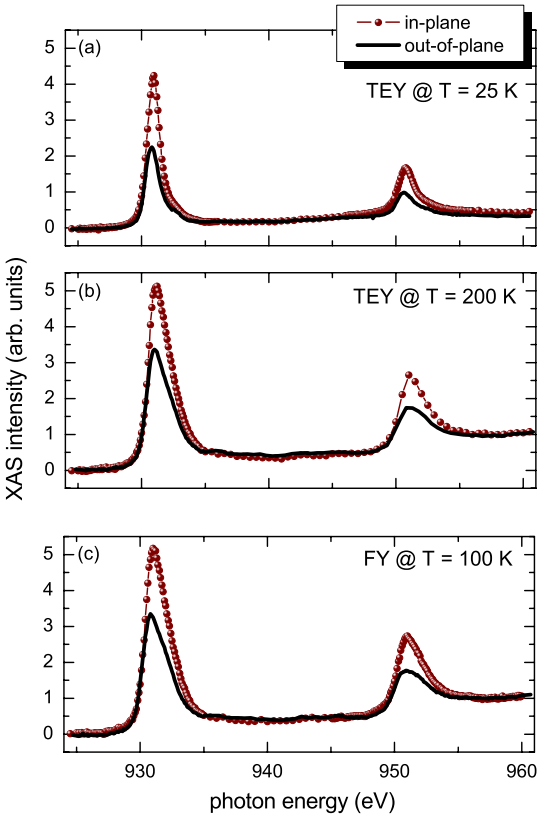

FIG. 7. (Color online) Comparison of Cu L edge XA spectra taken with in-plane and out-of-plane polarization. Shown are surface-sensitive TEY detection at (a) T=25 K and (b) 200 K and (c) bulk-sensitive FY detection. Data in (a) was taken at ANKA; (b) and (c) at ELETTRA.

This T independence is robust, as expected for an energy-level alignment by hybridization. The orbital occupation being independent of temperature also emphasizes the absence of any signature on the Mn XMCD related to an induced superconductivity on interfacial LCMO.

Figure 8 shows the XLD at the Mn L edge, which amounts to no more than 4.5% (at the Mn L_3 edge). The inset shows LD at the Cu L edge in interface-sensitive TEY mode at T=25 K [see Fig. 7(a)]. In contrast to Chakhalian *et al.*[12] who reported the absence of XLD at the Mn L edge, stemming from an equal occupation of Mn $d_{x^2-y^2}$ and Mn d_{3z^2} orbitals, we observe a (small) negative XLD signal. This is consistent with published reports of negative XLD of a few percent ($\leq$5%) in very thin $La_{0.7}Sr_{0.3}MnO_3$ films grown on a number of different substrates.[26] Since the oxygen octahedra around Mn are only weakly distorted (lattice mismatch $<$0.3%), most of the linear dichroism should arise from interfacial Mn atoms. Following the calculations of Ref. 21, linear dichroism at the Cu and the Mn L edge should have the same sign at the YBCO/LCMO interface because in both cases the density of unoccupied $d_{x^2-y^2}$ states is higher than for d_{3z^2} states at the Fermi level.

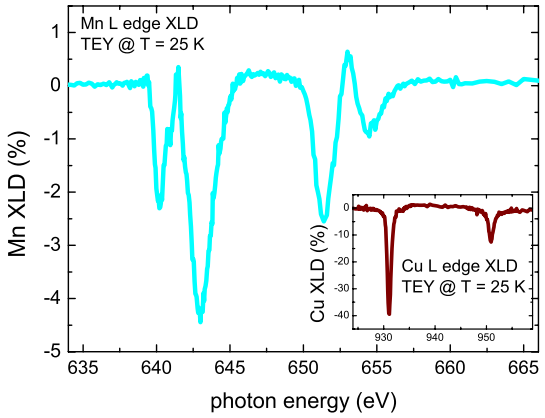

FIG. 8. (Color online) XLD signal of the YBCO/LCMO bilayer at the Mn L edge in TEY mode at T=25 K. The inset shows the corresponding LD at the Cu L edge.

VII. CONCLUSIONS

We examined bilayers of the high-temperature superconductor YBCO and the almost 100% spin-polarized ferromagnet LCMO by means of electric transport measurements and x-ray absorption spectroscopy. The observation of a significant T_c suppression only for very small YBCO thickness can be explained by the strong interaction between Mn and Cu moments at the interface, which we observed by XAS measurements. Our XMCD data clearly confirm the phenomenon of magnetic moments being induced on copper atoms at the LCMO/YBCO interface, with an even stronger interaction than found in the original report.[11] The effect is robust and closely follows the temperature dependence of magnetism in the manganite. From the analysis of linear dichroism data, we conclude that covalent bonding and the resulting "orbital reconstruction" are not necessary for the spin canting of Cu moments in proximity to Mn spins.

ACKNOWLEDGMENTS

R.W. gratefully acknowledges support by the Cusanuswerk, Bischöfliche Studienförderung. A.R. and B.A.D. would like to acknowledge useful discussions with A. Verna. B.A.D. acknowledges support by the FVG Regional project SPINOX funded by Legge Regionale 26/2005 and Decreto 2007/LAVFOR/1461. ANKA Angströmquelle Karlsruhe and ELETTRA Synchrotron Trieste are acknowledged for the provision of beamtime. This work was funded by the Deutsche Forschungsgemeinschaft (Project No. KL 930/11-2).

*koelle@uni-tuebingen.de

[1] A. I. Buzdin, Rev. Mod. Phys. **77**, 935 (2005).
[2] F. S. Bergeret, A. F. Volkov, and K. B. Efetov, Phys. Rev. B **69**, 174504 (2004).
[3] G. Deutscher, Rev. Mod. Phys. **77**, 109 (2005).
[4] M. Varela, A. R. Lupini, S. J. Pennycook, Z. Sefrioui, and J. Santamaria, Solid-State Electron. **47**, 2245 (2003).
[5] Z. L. Zhang, U. Kaiser, S. Soltan, H.-U. Habermeier, and B. Keimer, Appl. Phys. Lett. **95**, 242505 (2009).
[6] Z. Sefrioui, D. Arias, V. Peña, J. E. Villegas, M. Varela, P. Prieto, C. León, J. L. Martinez, and J. Santamaria, Phys. Rev. B **67**, 214511 (2003).
[7] V. Peña, Z. Sefrioui, D. Arias, C. Leon, J. Santamaria, M. Varela, S. J. Pennycook, and J. L. Martinez, Phys. Rev. B **69**, 224502 (2004).
[8] S. Soltan, J. Albrecht, and H.-U. Habermeier, Phys. Rev. B **70**, 144517 (2004).
[9] V. Peña, Z. Sefrioui, D. Arias, C. Leon, J. Santamaria, J. L. Martinez, S. G. E. te Velthuis, and A. Hoffmann, Phys. Rev. Lett. **94**, 057002 (2005).
[10] J. Hoppler, J. Stahn, C. Niedermayer, V. K. Malik, H. Bouyanfif, A. J. Drew, M. Rössle, A. Buzdin, G. Cristiani, H.-U. Habermeier, B. Keimer, and C. Bernhard, Nature Mater. **8**, 315 (2009).
[11] J. Chakhalian, J. W. Freeland, G. Srajer, J. Strempfer, G. Khaliullin, J. C. Cezar, T. Charlton, R. Dalgliesh, C. Bernhard, G. Cristiani, H.-U. Habermeier, and B. Keimer, Nat. Phys. **2**, 244 (2006).
[12] J. Chakhalian, J. W. Freeland, H.-U. Habermeier, G. Cristiani, G. Khaliullin, M. van Veenendaal, and B. Keimer, Science **318**, 1114 (2007).
[13] R. Werner, C. Raisch, V. Leca, V. Ion, S. Bals, G. Van Tendeloo, T. Chassé, R. Kleiner, and D. Koelle, Phys. Rev. B **79**, 054416 (2009).
[14] G. Panaccione, I. Vobornik, J. Fujii, D. Krizmancic, E. Annese, L. Giovanelli, F. Maccherozzi, F. Salvador, A. D. Luisa, D. Benedetti, A. Gruden, P. Bertoch, F. Polack, D. Cocco, G. Sostero, B. Diviacco, M. Hochstrasser, U. Maier, D. Pescia, C. H. Back, T. Greber, J. Osterwalder, M. Galaktionov, M. Sancrotti, and G. Rossi, Rev. Sci. Instrum. **80**, 043105 (2009).
[15] M. B. Salamon and M. Jaime, Rev. Mod. Phys. **73**, 583 (2001).
[16] Z. Q. Yang, R. Hendrikx, J. Aarts, Y. Qin, and H. W. Zandbergen, Phys. Rev. B **67**, 024408 (2003).
[17] B. Vengalis, A. Maneikis, F. Anisimovas, R. Butkutė, L. Dapkus, and A. Kindurys, J. Magn. Magn. Mater. **211**, 35 (2000).
[18] L. Abad, V. Laukhin, S. Valencia, A. Gaup, W. Gudat, L. Balcells, and B. Martínez, Adv. Funct. Mater. **17**, 3918 (2007).
[19] R. A. Rao, D. Lavric, T. K. Nath, C. B. Eom, L. Wu, and F. Tsui, Appl. Phys. Lett. **73**, 3294 (1998).
[20] M. Abbate, F. M. F. de Groot, J. C. Fuggle, A. Fujimori, O. Strebel, F. Lopez, M. Domke, G. Kaindl, G. A. Sawatzky, M. Takano, Y. Takeda, H. Eisaki, and S. Uchida, Phys. Rev. B **46**, 4511 (1992).
[21] X. Yang, A. Yaresko, V. Antonov, and O. Andersen, arXiv:0911.4349 (unpublished).
[22] C. T. Chen, Y. U. Idzerda, H.-J. Lin, N. V. Smith, G. Meigs, E. Chaban, G. H. Ho, E. Pellegrin, and F. Sette, Phys. Rev. Lett. **75**, 152 (1995).
[23] C. Piamonteze, P. Miedema, and F. M. F. de Groot, Phys. Rev. B **80**, 184410 (2009).
[24] J. Lüning, F. Nolting, A. Scholl, H. Ohldag, J. W. Seo, J. Fompeyrine, J.-P. Locquet, and J. Stöhr, Phys. Rev. B **67**, 214433 (2003).
[25] S. Gota, M. Gautier-Soyer, and M. Sacchi, Phys. Rev. B **62**, 4187 (2000).
[26] A. Tebano, C. Aruta, S. Sanna, P. G. Medaglia, G. Balestrino, A. A. Sidorenko, R. D. Renzi, G. Ghiringhelli, L. Braicovich, V. Bisogni, and N. B. Brookes, Phys. Rev. Lett. **100**, 137401 (2008).

Publication V

Improved tunneling magnetoresistance at low temperature in manganite junctions grown by molecular beam epitaxy

R. Werner,[1] A. Yu. Petrov,[2] L. Alvarez Miño,[3] R. Kleiner,[1] D. Koelle,[1] and B. A. Davidson[2,a)]
[1]*Physikalisches Institut–Experimentalphysik II, Universität Tübingen, Auf der Morgenstelle 14, 72076 Tübingen, Germany*
[2]*TASC National Laboratory, CNR-IOM, S.S. 14 Km 163.5 in AREA Science Park, 34012 Basovizza, Trieste, Italy*
[3]*Universidad Nacional de Colombia, Sede Manizales, Cra 27 # 64-60 Manizales, Colombia*

(Received 24 January 2011; accepted 31 March 2011; published online 20 April 2011)

We report resistance versus magnetic field measurements for a $La_{0.65}Sr_{0.35}MnO_3/SrTiO_3/La_{0.65}Sr_{0.35}MnO_3$ tunnel junction grown by molecular-beam epitaxy, that show a large field window of extremely high tunneling magnetoresistance (TMR) at low temperature. Scanning the in-plane applied field orientation through 360°, the TMR shows fourfold symmetry, i.e., biaxial anisotropy, aligned with the crystalline axis but not the junction geometrical long axis. The TMR reaches ~1900% at 4 K, corresponding to an interfacial spin polarization of >95% assuming identical interfaces. These results show that uniaxial anisotropy is not necessary for large TMR, and lay the groundwork for future improvements in TMR in manganite junctions. © *2011 American Institute of Physics*. [doi:10.1063/1.3581885]

The figure of merit for magnetic tunnel junctions (MTJs) is the tunneling magnetoresistance (TMR) ratio, which determines their performance in practical devices such as magnetic random access memories and low-field sensors.[1] An MTJ consists of two ferromagnetic electrodes separated by a thin insulating tunneling barrier. According to the Julliere model,[2] the TMR ratio is defined as $TMR_J=(R_{AP}-R_P)/R_P=2P_1P_2/(1-P_1P_2)$. Here P_1 and P_2 are the spin polarizations of the two electrodes and R_{AP} and R_P are the junction resistances with antiparallel and parallel orientation of magnetization M of the two electrodes, respectively. Accordingly, an MTJ made from half-metallic electrode materials, such as doped manganites,[3] should yield an infinite TMR ratio at temperature T well below the Curie temperature T_C. Noting that TMR is more precisely associated with the properties of the electrode/barrier interface,[4] this concept has been extended to also describe interfaces as half-metallic,[5] i.e., the TMR is determined by the spin-polarization of the local density of states at the two interfaces with the barrier. Ferromagnetic correlations at manganite surfaces and interfaces are known to be weaker than in bulk, causing a "dead layer."[6–8] For example, at the vacuum/$La_{1-x}Sr_xMnO_3$ (LSMO) interface the nonferromagnetic layer is about three unit cells (uc) thick at $T=200$ K,[9] well below the bulk $T_C\approx360$ K for ferromagnetic LSMO (F-LSMO) with optimal doping $x=0.35$. This and other effects have been discussed to explain the disappearance of the TMR well below the bulk T_C in manganite MTJs.[6,10–12] Attempts have been made to "engineer" the interfaces by creating a doping profile to overcome this problem, and even though the TMR ratio remained low,[13] spectroscopic characterization suggested this approach could improve the low-temperature TMR.[14]

To date, TMR at small dc voltage bias of MTJs based on nonoxide electrodes reached ≈1150% at $T=5$ K (Ref. 15) while the highest ratio was reported for manganite/titanate interfaces with a maximum value of about 1800% at 4 K in a very small window of applied in-plane magnetic field H.[16] Here, an antiferromagnetic CoO layer was used to pin the upper electrode via exchange bias[17] that can favor uniaxial anisotropy in the pinned electrode; such anisotropy was claimed necessary for the stabilization of well-defined antiparallel states and high TMR ratios.[11,16]

In this letter, we report on the TMR of MTJs based on F-LSMO with an antiferromagnetic $x=0.65$ LSMO (AF-LSMO) exchange bias layer and a $SrTiO_3$ (STO) barrier, grown by molecular beam epitaxy (MBE). We find a TMR ratio up to ~1900% at $T=4$ K, which decreases rapidly with increasing T, disappearing at ~280 K. Rotating the applied in-plane magnetic field, we find a fourfold symmetry of the TMR, indicating that uniaxial anisotropy in not required for high TMR ratios.

For sample fabrication, we developed atomic-layer control of LSMO and STO growth and their interfaces by combining reactive MBE (Ref. 18) with *in situ* reflection high-energy electron diffraction (RHEED) techniques, extending the work of Haeni *et al.*[19] These RHEED techniques permit us to adjust the surface termination at any point during deposition, including during interface growth.[20] LSMO/STO/LSMO trilayers were grown on (001)-oriented STO substrates at a typical substrate temperature $T_s=750$ °C and ozone pressure $p=10^{-6}$ mbar. The bottom and top F-LSMO electrode thicknesses were 50 uc, separated by a tunnel barrier of stoichiomsic STO, 5–6 uc thick. A 100 uc thick AF-LSMO layer was grown underneath the bottom electrode to increase and shift its coercive field H_c due to exchange bias. The resulting difference in H_c between the electrodes favors the establishment of fully antiparallel magnetization orientation of the two electrodes in a larger window of H (Ref. 17) in the resistance versus magnetic field $R(H)$ loops used to determine the TMR ratio. The effect of exchange bias on the junction TMR characteristics should only be seen below ~250 K, in agreement with exchange bias effects seen in the hysteresis loops of an AF-LSMO (100 uc)/F-LSMO (50

a)Electronic mail: davidson@tasc.infm.it.

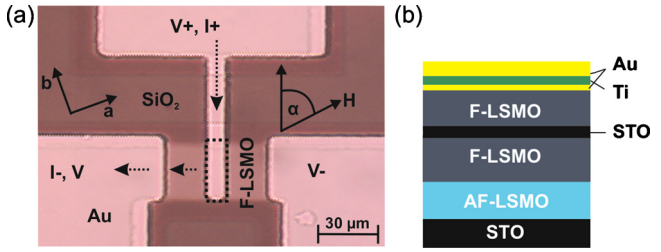

FIG. 1. (Color online) (a) Optical image of the MTJ. The arrows indicate the current flow while the junction area is indicated by the dashed rectangle. (b) The inset shows a cross section of the stacking sequence of the MTJ.

uc) bilayer by superconducting quantum interference device magnetometry measured independently.

Vertical mesa MTJs were patterned in several steps by photolithography and Ar ion milling; for details see Ref. 21. Figure 1 shows in (a) an optical microscope image of an MTJ with a 5×30 μm^2 mesa with vertical current injection from a Au/Ti/Au top contact and the stacking sequence of the sample in (b).

The junction resistance was more than an order of magnitude larger than the electrode resistances, ensuring uniform injection of bias current I.[22] Electrical transport measurements were made in 2- and 3-point geometries in a He-flow cryostat at $T=4-300$ K. A Helmholtz coil outside the cryostat allows full rotation of H from $\alpha=0°-360°$ with a maximum amplitude $H_{max}=1$ kOe. The angle α describes the relative orientation of H with respect to the long side of the junction (cf. Fig. 1). All $R(H)$ loops shown or discussed below were taken after the junction was field-cooled at $H=H_{max}$ with fixed cooling angle $\alpha_{FC}=70°$, which corresponds to the crystallographic lattice a-axis direction. The (differential) junction resistance was measured by a lock-in amplifier at a dc voltage bias $V=0$, using an ac current amplitude of a few nanoampere. Full characterization of the junction $I(V)$ and TMR as a function of dc voltage bias will be reported separately.

The inset of Fig. 2 shows two representative $R(H)$ loops at low temperature ($T=4$ K) and $\alpha=145°$, taken after two identical cooling cycles. We define $\mathrm{TMR}(H)=[R(H)-R_{min}]/R_{min}$ and the maximum TMR ratio within an $R(H)$ loop as $\mathrm{TMR}_{max}=(R_{max}-R_{min})/R_{min}$. Here, R_{max} and R_{min} are the maximum and minimum junction resistances, and only in

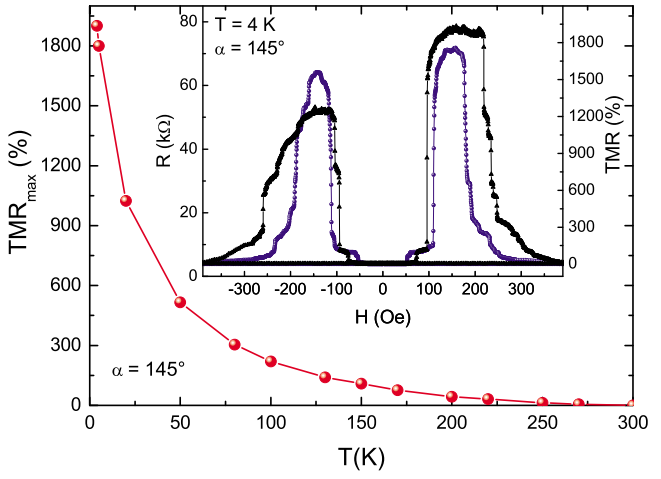

FIG. 2. (Color online) Maximum TMR ratio vs. temperature for $\alpha_{FC}=70°$, $\alpha=145°$. The inset shows two $R(H)$ sweeps measured at 4 K for the same field conditions after different cooling cycles.

the ideal case of uniform and fully antiparallel electrode magnetization does this definition coincide with TMR_J defined above. The $R(H)$ loops differ in shape (asymmetry), R_{max} and width ΔH of the magnetic field window, defined as the full width at half maximum of the $R(H)$ peaks. The $R(H)$ loop with larger ΔH shows a stronger asymmetry in peak heights and the highest $\mathrm{TMR}_{max}=1904\%$, which also exceeds measured TMR ratios for other combinations of field orientations α_{FC} and α, during cooling and measurement, respectively.

The $R(H)$ loops (cf. inset of Fig. 2) show switching to the high and low R states at ~100 Oe and 200–300 Oe, which we attribute to H_c of the upper (free) and bottom (exchange-biased) electrodes, respectively. We note that these values of increased H_c as compared to single layer F films and nearly negligible hysteresis loop shifts H_{eb} for the bottom electrode due to an exchange bias field deduced from the inset of Fig. 2, are consistent with H_{eb} and H_c in exchange bias AF/F bilayers of the same thicknesses measured separately (not shown). The $R(H)$ loops for nominally identical cooling cycles implies that the exchange bias coupling at the AF/F interface can vary between cooling cycles. We attribute this to a history dependence of the exchange bias, i.e., the exchange coupling at the AF/F interface may depend sensitively on exactly its cooling history. Reproducible exchange coupling is required for practical devices, and should be further investigated in our LSMO heterostructures.

The main panel in Fig. 2 shows the temperature dependence of TMR_{max}, which decays quickly with increasing T and vanishes at ~280 K, which is also near the temperature at which exchange bias effects disappear. The strong decay of $\mathrm{TMR}_{max}(T)$, could in principle be explained by different T-dependent mechanisms, for example, intrinsic to the LSMO/STO interfaces (such as intrinsic loss of spin polarization) or extrinsic (such as weakening of the exchange bias pinning of the bottom electrode). Any study of the temperature dependence of the domain structure and thus relative magnetization orientations of the electrodes would require a microscopic technique such as demonstrated in Ref. 23. Evidence for weakened exchange bias pinning at higher T is seen in the decreasing asymmetry of ΔH and R_{max} as temperature is increased; the asymmetry in $R(H)$ between positive and negative H disappears around ~100 K. Further characterization is necessary to distinguish between these competing mechanisms, and will be crucial to understand any limits to the potential high-temperature TMR.

Figure 3 shows a polar plot of $\mathrm{TMR}_{max}(\alpha)$ at $T=30$ K, after field-cooling along the a-axis of LSMO, which still shows a slight asymmetry for opposite field directions. The fourfold symmetry of $\mathrm{TMR}_{max}(\alpha)$ indicates a biaxial anisotropy with easy axis along the a- and b-directions of our F-LSMO layers. The slight difference in TMR_{max} values for orientations close to the a- and b-axes could be due to, e.g., a shape effect correlated with the junction long axis, or a small anisotropy in the exchange bias; fourfold symmetry in the switching fields has been previously reported.[24] We note that cooling the device with the field oriented in different directions does not change the fourfold symmetry seen in the polar plot, although it can have a sizable impact on TMR_{max}. Additional study of the interplay between junction geometry and magnetocrystalline anisotropy will be necessary to further optimize these MTJs.

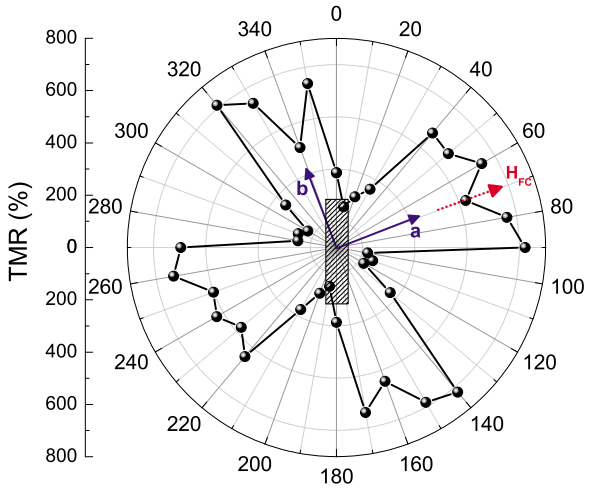

FIG. 3. (Color online) Polar plot of the maximum TMR ratio (at $T=30$ K) vs field direction α for field-cooling at $\alpha_{FC}=70°$ (dashed arrow). Crystalline axis are indicated by solid arrows; junction orientation is indicated by rectangle.

In summary, we have shown $R(H)$ at 4 K for a manganite MTJ with a useful TMR_{max} ratio of 1900%, the largest value for any MTJ reported so far in the literature at low dc bias. The strength of pinning of one electrode magnetization via exchange bias has a noticeable influence on the TMR both by enlarging the magnetic field window of antiparallel alignments and inducing an asymmetry in the $R(H)$ curves but is also very sensitive to the cooling history. The polar plot of $TMR_{max}(\alpha)$ demonstrates that uniaxial anisotropy in the F layers is not necessary for high TMR. It is reasonable that interface roughness, oxygen vacancies and the interface growth play a crucial role in the exchange bias mechanism in these manganite interfaces as has been demonstrated in more conventional exchange bias systems,[25] and merits further study.

R.W. gratefully acknowledges support by the Cusanuswerk, Bischöfliche Studienförderung. B.A.D. and A.Y.P. acknowledges support by the FVG Regional project SPINOX funded by Legge Regionale Grant No. 26/2005 and Decreto Grant No. 2007/LAVFOR/1461. L.A.-M. thanks the Abdus Salam ICTP (Trieste) for financial support through a STEP fellowship. The TASC Technical group is acknowledged for contributions to the design and construction of the MBE system. This work was funded in part by the Deutsche Forschungsgemeinschaft (Project No. KO 1303/8-1).

[1]S. A. Wolf, D. D. Awschalom, R. A. Buhrman, J. M. Daughton, S. von Molnár, M. L. Roukes, A. Y. Chtchelkanova, and D. M. Treger, Science **294**, 1488 (2001).
[2]M. Julliere, Phys. Lett. A **54**, 225 (1975).
[3]J. M. D. Coey, M. Viret, and S. von Molnar, Adv. Phys. **48**, 167 (1999).
[4]J. M. De Teresa, A. Barthélémy, A. Fert, J. P. Contour, F. Montaigne, and P. Seneor, Science **286**, 507 (1999).
[5]M. Bowen, J.-L. Maurice, A. Barthélémy, M. Bibes, D. Imhoff, V. Bellini, R. Bertacco, D. Wortmann, P. Seneor, E. Jacquet, A. Vaures, J. Humbert, J.-P. Contour, C. Colliex, S. Blugel, and P. H. Dederichs, J. Phys.: Condens. Matter **19**, 315208 (2007).
[6]J. Z. Sun, D. W. Abraham, R. A. Rao, and C. B. Eom, Appl. Phys. Lett. **74**, 3017 (1999).
[7]M. Bibes, L. Balcells, S. Valencia, J. Fontcuberta, M. Wojcik, E. Jedryka, and S. Nadolski, Phys. Rev. Lett. **87**, 067210 (2001).
[8]A. Tebano, C. Aruta, S. Sanna, P. G. Medaglia, G. Balestrino, A. A. Sidorenko, R. D. Renzi, G. Ghiringhelli, L. Braicovich, V. Bisogni, and N. B. Brookes, Phys. Rev. Lett. **100**, 137401 (2008).
[9]A. Verna, B. A. Davidson, Y. Szeto, A. Y. Petrov, A. Mirone, A. Giglia, N. Mahne, and S. Nannarone, J. Magn. Magn. Mater. **322**, 1212 (2010).
[10]M. Viret, M. Drouet, J. Nassar, J. P. Contour, C. Fermon, and A. Fert, Europhys. Lett. **39**, 545 (1997).
[11]M.-H. Jo, N. D. Mathur, N. K. Todd, and M. G. Blamire, Phys. Rev. B **61**, R14905 (2000).
[12]J. O'Donnell, A. E. Andrus, S. Oh, E. V. Colla, and J. N. Eckstein, Appl. Phys. Lett. **76**, 1914 (2000).
[13]H. Yamada, Y. Ogawa, Y. Ishii, H. Sato, M. Kawasaki, H. Akoh, and Y. Tokura, Science **305**, 646 (2004).
[14]J. J. Kavich, M. P. Warusawithana, J. W. Freeland, P. Ryan, X. Zhai, R. H. Kodama, and J. N. Eckstein, Phys. Rev. B **76**, 014410 (2007).
[15]S. Ikeda, J. Hayakawa, Y. Ashizawa, Y. M. Lee, K. Miura, H. Hasegawa, M. Tsunoda, F. Matsukura, and H. Ohno, Appl. Phys. Lett. **93**, 082508 (2008).
[16]M. Bowen, M. Bibes, A. Barthélémy, J.-P. Contour, A. Anane, Y. Lemaître, and A. Fert, Appl. Phys. Lett. **82**, 233 (2003).
[17]I. K. Schuller, Mater. Res. Bull. **29**, 642 (2004).
[18]J. N. Eckstein and I. Bozovic, Annu. Rev. Mater. Sci. **25**, 679 (1995).
[19]J. M. Haeni, C. D. Theis, and D. G. Schlom, J. Electroceram. **4**, 385 (2000).
[20]B. A. Davidson, A. Y. Petrov, A. Verna, X. Torrelles, M. Pedio, A. Cossaro, and S. Nannarone (unpublished).
[21]See supplementary material at http://dx.doi.org/10.1063/1.3581885 for details on MTJ patterning.
[22]R. J. M. van de Veerdonk, J. Nowak, R. Meservey, J. S. Moodera, and W. J. M. de Jonge, Appl. Phys. Lett. **71**, 2839 (1997).
[23]M. Wagenknecht, H. Eitel, T. Nachtrab, J. B. Philipp, R. Gross, R. Kleiner, and D. Koelle, Phys. Rev. Lett. **96**, 047203 (2006).
[24]M.-H. Jo, N. D. Mathur, and M. G. Blamire, Appl. Phys. Lett. **80**, 2722 (2002).
[25]W. Kuch, L. I. Chelaru, F. Offi, J. Wang, M. Kotsugi, and J. Kirschner, Nature Mater. **5**, 128 (2006).

Supplementary information for: Improved tunneling magnetoresistance at low temperature in manganite junctions grown by molecular beam epitaxy

R. Werner, A. Yu. Petrov, R. Kleiner, D. Koelle, and B. A. Davidson

This supplement describes in detail the patterning procedure for MTJ fabrication, which is based on optical lithography and Ar ion milling. We use a self-alignment process for final definition of the MTJ area, which ensures alignment of the metallic wiring layer with the upper electrode of the MTJ and which prevents exposure of the junction edges to chemicals during any time in the patterning process. The MTJs were patterned in four steps, which we denote as (I) feed line patterning, (II) edge isolation, (III) metallization and (IV) junction milling.

During Ar^+-milling (beam energy 0.3 keV), the sample was mounted on a water-cooled ($T \approx 8°C$) copper block which reduces heating of the sample. A shutter in front of the sample was used to mill in intervals of $t_o = 5$ s open and $t_c = 10$ s closed. This helps to avoid excessive heating of the sample surface, which might induce interdiffusion at the interface and oxygen loss in the LSMO and STO layers, both of which do have a detrimental effect on the TMR.

I. FEED LINE PATTERNING

This step defines the feed lines of the MTJ. Figure 1 (a) shows a cross section of the as-grown sample, indicating the stacking sequence. The two F-LSMO electrodes are separated by 6 uc thick STO barrier layer (black), and the sample was covered in-situ by a ~ 1 nm thick Au layer (yellow), for protection against humidity and chemicals during the patterning process. In a first step, the sample was coated by photoresist (PR) which was patterned by optical lithography [c.f. Fig. 1 (b)]. Subsequently, the sample was loaded into the milling chamber, and the regions exposed to the Ar ions were milled down into the STO substrate. Figure 1 (c) shows the cross section after PR removal in acetone, and Fig. 1 (d) shows the corresponding top view. After step I, the feed lines for current and voltage terminals (I^+, V^+) and (I^-, V^-) are completely separated.

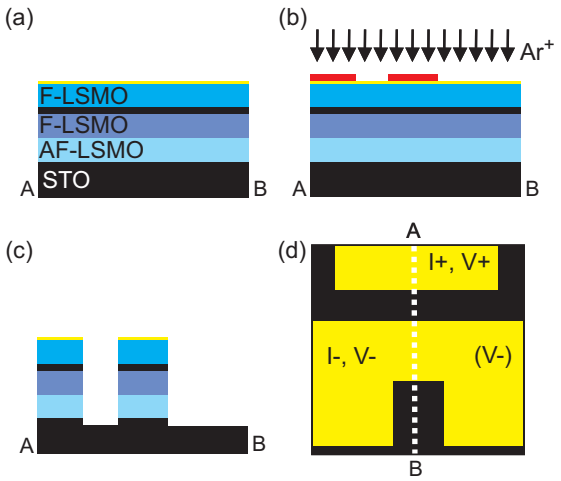

FIG. 1: **Feed line patterning:** cross sections of the sample, (a) prior to patterning, (b) before, and (c) after Ar ion milling and removal of PR. (d) shows top view corresponding to (c); white dashed line indicates the position of cross sections $\overline{AB}$ shown in (a)-(c).

II. EDGE ISOLATION

The next step provides isolation of the edges of the feed lines by an SiO_2 layer and at the same time defines the length (along $\overline{AB}$) of the MTJ. Here, a mask was used which had essentially the same geometry as the one used for feed line patterning. However, the structures on this mask are slightly smaller, i.e. their edges are shifted by 10 μm with respect to the previous mask; c.f. Fig. 2(a). Furthermore, Ar ion milling is stopped after milling into the bottom F-LSMO electrode as indicated in Fig. 2 (b). Subsequently, we sputtered ~ 40 nm of SiO_2 in a Ar/O_2 atmosphere (at 200 Pa), followed by lift-off. This process

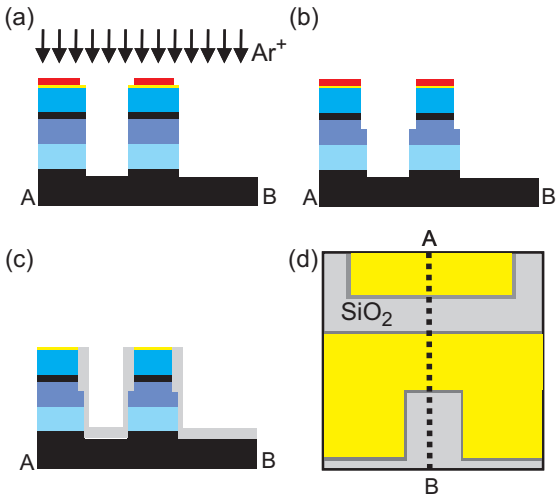

FIG. 2: **Edge isolation:** cross sections of the sample, (a) before, and (b) after Ar ion milling into the bottom F-LSMO layer. (c) shows the structure after deposition of an SiO_2 layer and lift-off patterning (removal of PR). (d) shows top view corresponding to (c); black dashed line indicates position of cross sections $\overline{AB}$ shown in (a)-(c).

results in the structure shown in Figs. 2 (c) and (d).

III. METALLIZATION

Step III provides a low-resistance connection between the upper F-LSMO electrode of the MTJ and the feed line with the (I^+, V^+) terminals, which shall ensure homogeneous current injection into the MTJ. For this purpose, a Ti(2 nm)/Au(50 nm)/Ti(10 nm) trilayer is deposited in-situ by electron beam evaporation. The bottom Ti layer is used as an adhesive layer underneath the Au layer, in order to improve sticking on the SiO_2 layer. The upper Ti layer on top of the Au layer will be used as a milling mask in step IV. We note that the in-situ Au layer (on top of F-LSMO) is crucial to avoid a high contact resistance between the upper F-LSMO layer and the bottom Ti layer.

Step III starts with preparation of a lift-off mask [c.f. Fig. 3 (a)], which covers everywhere, except the green areas shown in Fig. 3 (d). Subsequently, the Ti/Au/Ti trilayer is deposited and patterned by lift-off. Figures 3 (b) and (c) show vertical ($\overline{AB}$) and horizontal ($\overline{CD}$) cross sections, respectively, after this step. Figure 3 (d) shows the corresponding top view at the end of this metallization process. The width of the central Ti/Au/Ti strip (along $\overline{CD}$) defines the width of the MTJ.

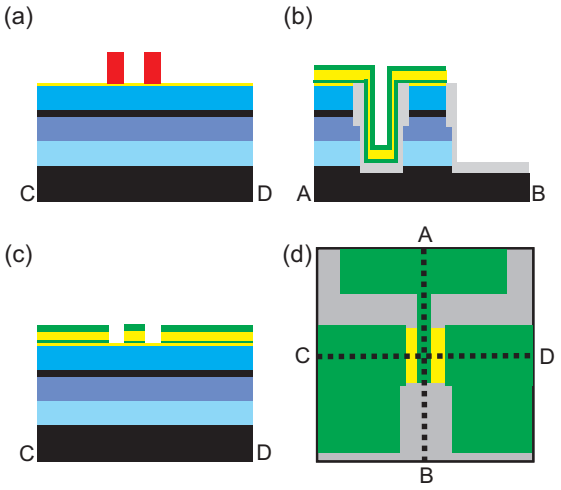

FIG. 3: **Metallization:** cross sections of the sample, (a) after patterning a lift-off mask, and (b),(c) after Ti/Au/Ti trilayer deposition and lift-off patterning (removal of PR). (d) shows top view corresponding to (b) and (c); black dashed lines indicate the position of the cross sections $\overline{AB}$ and $\overline{DC}$ shown in (a), (b) and (c).

IV. JUNCTION MILLING

Step IV is the final patterning step of the MTJ, using a self-alignment method. Here, the whole sample area is milled with Ar^+, without any PR [c.f Fig. 4 (a)]. This step is possible, as the milling rate for Ti is much lower than the ones for Au, F/AF-LSMO and STO. During milling, the areas uncovered by Ti are milled down to the bottom F-LSMO electrode as shown in Fig. 4 (b). The thickness ~ 10 nm of the Ti layer has been adjusted to ensure that after milling, also the upper Ti layer has been removed completely [c.f. Figs. 4 (b) and (c)]. The final top view, shown in Fig. 4 (d), is a schematic representation of the optical image shown in Fig. 1 in the main paper.

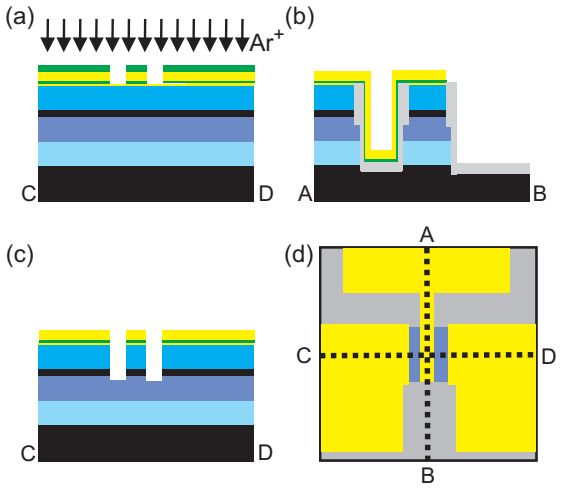

FIG. 4: **Junction milling:** cross sections of the sample, (a) at the start of Ar milling, and (b),(c) after Ar milling. (d) shows top view corresponding to (b) and (c); black dashed lines indicate the position of the cross sections $\overline{AB}$ and $\overline{DC}$ shown in (a), (b) and (c).

Publication VI

Local tunneling magnetoresistance probed by low-temperature scanning laser microscopy

Robert Werner,[1] Mathias Weiler,[2] Aleksandr Yu. Petrov,[3] Bruce A. Davidson,[3] Rudolf Gross,[2] Reinhold Kleiner,[1] Sebastian T. B. Goennenwein,[2] and Dieter Koelle[1,a)]
[1]*Physikalisches Institut and Center for Collective Quantum Phenomena in LISA$^+$, Universität Tübingen, 72076 Tübingen, Germany*
[2]*Walther-Meißner-Institut, Bayerische Akademie der Wissenschaften, 85748 Garching, Germany*
[3]*CNR-IOM TASC National Laboratory, S.S. 14 Km 163.5 in AREA Science Park, 34012 Basovizza, Trieste, Italy*

(Received 29 August 2011; accepted 17 October 2011; published online 4 November 2011)

Tunneling magnetoresistance in a vertical manganite junction was investigated by low-temperature scanning laser microscopy (LTSLM) allowing to determine the local relative magnetization $\boldsymbol{M}$ orientation of the two electrodes as a function of magnitude and orientation of the external magnetic field $\boldsymbol{H}$. Sweeping the field amplitude at fixed orientation revealed magnetic domain nucleation and propagation in the junction electrodes. For the high-resistance state, an almost single-domain antiparallel magnetization configuration was achieved, while in the low-resistance state the junction remained in a multidomain state. Calculated resistance $R_{\mathrm{calc}}(\boldsymbol{H})$ based on the local $\boldsymbol{M}$ configuration obtained by LTSLM is in quantitative agreement with $R(\boldsymbol{H})$ measured by magnetotransport. © *2011 American Institute of Physics*. [doi:10.1063/1.3659301]

Tunneling magnetoresistance (TMR) is an important effect for spintronics[1] which has been vigorously investigated both theoretically[2,3] and experimentally,[4,5] predominantly to develop devices such as magnetic random access memories[6] based on magnetic tunnel junctions (MTJs). In an MTJ, two ferromagnetic electrodes are separated by a thin insulating tunnel barrier. According to the Jullière model,[4] the maximum TMR ratio is $\mathrm{TMR_J} \equiv (R_{\mathrm{ap}} - R_{\mathrm{p}})/R_{\mathrm{p}}$, where R_{ap} and R_{p} is the resistance for antiparallel and parallel orientation of the magnetizations $\boldsymbol{M}$ of the two electrodes, respectively. While integral TMR properties of MTJs have been investigated in detail,[7,8] not much is known about the impact of their magnetic microstructure on the TMR properties. However, both in view of applications and from a fundamental point of view, it is of high interest to identify the spatial dependence of the TMR on the magnetic properties of the electrodes. Nucleation and growth of magnetic domains in ferromagnets has been the focus of many efforts, using techniques such as magneto-optical Kerr, magnetic force, spin-polarized scanning tunneling, spin-polarized scanning electron, and photoemission microscopy.[9] Low-temperature scanning laser microscopy (LTSLM) has been used to visualize locally different resistive states in a quasi-1-dimensional $La_{0.67}Ca_{0.33}MnO_3$ thin film grain boundary junction, for which it has been shown that the obtained LTSLM signal is directly proportional to the local magnetoresistance ratio.[10] These results suggested that LTSLM could also be useful to investigate TMR in vertical MTJs under typical bias conditions and in a wide range of magnetic fields.

In this letter, we report on LTSLM imaging of resistive states in a planar $La_{0.65}Sr_{0.35}MnO_3/SrTiO_3/La_{0.65}Sr_{0.35}MnO_3$ (LSMO/STO/LSMO) heterostructure MTJ upon variation of direction and amplitude of the external in-plane magnetic field $\boldsymbol{H}$. The TMR of this device was investigated in Ref. 11. LTSLM probes changes in the tunneling conductivity induced by local thermal perturbation, which allows to infer the spatial distribution of the relative magnetization orientation of the two electrodes. By varying $\boldsymbol{H}$, imaging of magnetic domain nucleation and propagation during the field-driven transitions between low- and high-resistive states is possible.

The heterostructure samples were grown *in situ* by molecular beam epitaxy on (001)-oriented STO substrates with 19 nm thick top and bottom LSMO electrodes, separated by 2.3 nm thick STO. A 38 nm thick antiferromagnetic $La_{0.35}Sr_{0.65}MnO_3$ layer was grown underneath the junction trilayer to pin the bottom electrode via exchange bias. MTJs with area $A_J = 5 \times 30\ \mu\mathrm{m}^2$ were patterned by optical lithography; for details on sample characterization and fabrication see Ref. 11. Figure 1(a) shows a schematic view of the MTJ. The relative difference in the orientation of the magnetization $\boldsymbol{M}_1$ and $\boldsymbol{M}_2$ of the top and bottom electrode, respectively, is given by the angle Θ. The angle α indicates the $\boldsymbol{H}$ direction with respect to the y-axis (long axis of the junction).

The sample was mounted on the cold finger of an optical ^{4}He flow cryostat. In-plane fields $|H| \leq 1$ kOe were applied by a rotatable Helmholtz coil and the junction resistance R was measured with constant bias current I in two-point configuration. Figure 1(b) shows R vs. temperature T warm-up curves at $H = 0$, recorded after the junction was field-cooled at $\alpha = 70°$ to 5 K and either a low-R state (with resistance R_{min}) or high-R state (with resistance R_{max}) was prepared.

In LTSLM, an amplitude modulated laser beam ($f \approx 10$ kHz, $\lambda = 680$ nm, $P = 5$ mW, spot diameter 1.5 μm,[10,12] penetration depth ~65 nm in LSMO (Ref. 13)) is scanned across the sample. Local heating in vicinity of the beam spot position (x_0,y_0) throughout the entire thickness of the LSMO/STO/LSMO stack induces a change in tunneling conductivity (conductance per area) g and in turn a change ΔG in the global conductance $G = 1/R$, which is detected as a change ΔV of the

a)Electronic mail: koelle@uni-tuebingen.de.

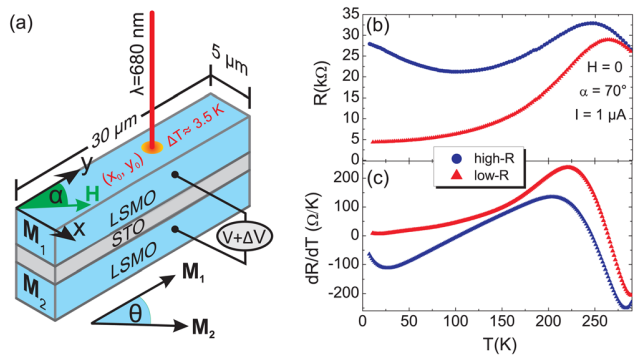

FIG. 1. (Color online) (a) MTJ geometry with angles α (between y direction and in-plane field H) and Θ (between magnetization M_1 and M_2). (b) $R(T)$ for high-R and low-R states. (c) $dR/dT(T)$ for same states as in (b).

voltage V across the sample. If $R(T)$ differs for parallel and antiparallel orientation of the magnetizations [cf. Fig. 1(b)], also $dR/dT(T)$ may be significantly different; cf. Fig. 1(c), which shows even opposite sign for $T \lesssim 120$ K and maximum difference in dR/dT at $T = 30$ K. In this case, LTSLM allows to image local variations of Θ. For a detailed analysis, see Ref. 14, where we assume that (i) local variations of g are due to variations in Θ, i.e., arise from the formation of multidomain states in the electrodes, (ii) laser heating in the top and bottom electrode does not significantly affect Θ, and (iii) the relation[15]

$$g(x,y,T) = g_p(T)\cos^2\left\{\frac{\Theta(x,y)}{2}\right\} + g_{ap}(T)\sin^2\left\{\frac{\Theta(x,y)}{2}\right\} \quad (1)$$

holds, with T-dependent $g_p = g(\Theta = 0)$ and $g_{ap} = g(\Theta = 180°)$. Then from LTSLM images $\Delta V(x_0,y_0)$, we extract (cf. Eq. (14) in Ref. 14) the convolution $\langle\cos\Theta(x_0,y_0)\rangle \approx a_1 \Delta V(x_0,y_0)/R^2 + a_2$ of $\cos\Theta(x, y)$ with the beam-induced T profile,[16] centered at (x_0,y_0) and assumed to be Gaussian with amplitude ΔT and variance σ. Data analysis[14] yields $\Delta T = 3.5$ K, $\sigma = 0.8$ μm, $a_1 \equiv \frac{2A_J}{I(G'_{ap}-G'_p)\Delta T 2\pi\sigma^2} = 4.0\frac{(\mathrm{k}\Omega)^2}{\mu\mathrm{V}}$ and $a_2 \equiv \frac{G'_p+G'_{ap}}{G'_{ap}-G'_p} = 0.6$; here, G'_{ap} and G'_{ap} are the T-derivative of the MTJ conductance for homogeneous parallel and antiparallel magnetization orientation, respectively.

For $T = 30$ K, Fig. 2 shows $R(H)$ and the corresponding $\mathrm{TMR}(H) \equiv [R(H) - R_{\min}]/R_{\min}$ (left panel) together with images $\langle\cos\Theta(x_0,y_0)\rangle$ for three different field orientations [increasing α from (a) to (c)]. Data were obtained for increasing field from $H = 0$, after the junctions were prepared in the low-R state upon applying $H = -1$ kOe. The overall shape of $R(H)$ depends strongly on α. However, in all cases, upon increasing H, we observe a subsequent step-like increase in R up to the maximum resistance $R_{\max}$, which depends on α, and a further decrease in several steps down to $R_{\min}$ at $H \gtrsim 300$ Oe, which is roughly the same for all values of α. For all values of α, at $H = 0$ ($R = R_{\min}$), the LTSLM images reveal $\langle\cos\Theta\rangle \approx 1$ except for the upper and lower edges where $\langle\cos\Theta\rangle$ approaches zero, indicative of domains with $\Theta = 90°$. Consequently, the measured $R_{\min} \approx 4.5$ k Ω is about 2% higher than our estimated value for R_p (i.e., for a homogeneous parallel orientation of the magnetizations).[14] For increasing $R(H)$, we find an inhomogeneous distribution of $\langle\cos\Theta\rangle$ and domains with $\Theta \sim 90° - 110°$ appear for all α. The maximum TMR value is reached for $\alpha = 140°$ and $H = 100$ Oe. The corresponding LTSLM image, Fig. 2(c)9, reveals that the junction is almost completely in the antiparallel state here. A similar value for $R_{\max}$ and a nearly homogeneous antiparallel configuration of M_1 and M_2 is found as well for $\alpha = 70°$. By contrast, for $\alpha = 7°$, an inhomogeneous

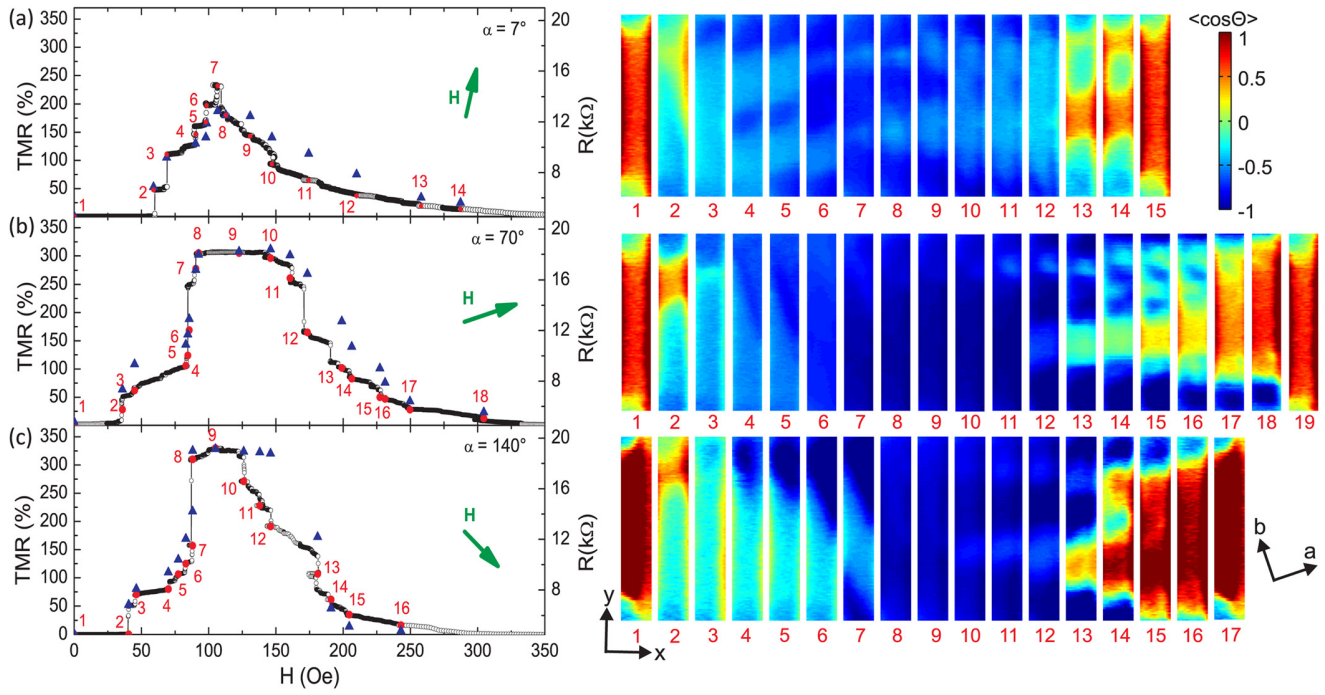

FIG. 2. (Color online) MTJ characteristics at $T = 30$ K ($I = 4$ μA) for different field orientation α. Left: R and TMR vs H (dots); triangles are R_{calc} from corresponding LTSLM images. Right: Spatial dependence of $\langle\cos\Theta\rangle$, as calculated from LTSLM voltage images for the bias points shown left and for $H = 1$ kOe [images 15 in (a), 19 in (b) and 17 in (c)].

distribution of $\langle\cos\Theta\rangle$ can be seen even at maximum resistance and consequently the TMR is strongly reduced compared to $\alpha = 140°$ and $\alpha = 70°$.

We note that the observed magnetic texture is qualitatively different for, e.g., images 5 and 13 in Fig. 2(c), although the integral $R(77\,\text{Oe}) = R(180\,\text{Oe})$. This demonstrates that an integral determination of the TMR is not sufficient to extract information on the magnetic microstructure. Furthermore, in the images of Figs. 2(b) and 2(c), domain walls are predominantly oriented along the *a*-axis [cf. Figs. 2(a)4-6 and 2(c)13-17] or *b*-axis [cf. Figs. 2(b)4-5 and 2(c)4-7] of the LSMO electrodes. From previous measurements of exchange-biased LSMO bilayers, the effect of exchange bias is primarily an increase of the coercive field of the pinned electrode (here, the MTJ bottom electrode) together with a small shift in the hysteresis loop. This coercivity contrast is clearly visible in the $R(H)$ scans of Figs. 2(b) and 2(c), which show a large field window with nearly fully antiparallel magnetizations and a plateau in maximum TMR. Therefore, the non-collinear magnetization configuration seen at small $H < 100\,\text{Oe}$ results from domain switching in the top (unpinned) electrode, while the magnetic structure at large $H > 130\,\text{Oe}$ results from domain switching in the bottom electrode. This suggests that domains tend to form along the crystalline *b*-axis in the upper electrode [Figs. 2(c)4-7 and 2(b)4-6] and along the *a*-axis in the bottom electrode [Figs. 2(c)10-16 and 2(b)12-18]. Using LSTSLM we can conclude that the switching process occurs via evolution of multidomain states, which form due to competition between crystalline anisotropy and shape anisotropy that can also be influenced by exchange bias. Furthermore, even though the LTSLM signal reflects the local relative angle between the two magnetizations, under conditions of sufficient coercivity contrast, the LTSLM technique can also yield information about domain evolution in the individual electrodes.

For each image shown in the right panel of Fig. 2, using Eq. (1) and $\langle\cos\Theta\rangle \approx \cos\Theta$ we can calculate the conductivity g and, by integrating over the junction area, the conductance G and junction resistance R, which is shown as R_{calc} by triangles in Figs. 2(a)–2(c). The measured $R(H)$ and TMR(H) is reproduced quite well for values of α and H below the TMR maximum. For fields above the TMR maximum there are deviations from the measured curves; the origin of this we could not clarify yet.[17]

In conclusion, we have analyzed by LTSLM the local TMR of a LSMO/STO/LSMO MTJ. In a quantitative analysis, we have calculated the local relative magnetization orientation of the two electrodes for different values of amplitude and direction of applied field. LTSLM images visualized magnetic domain nucleation and propagation during magnetic field sweeps. The domain walls are predominantly oriented along the crystalline *a*- and *b*-axes of LSMO. The LTSLM images also allowed to calculate the global TMR, yielding quantitative agreement with the integral $R(H)$ measurements. The results show that LTSLM can be used to link the magnetic microstructure to the integral magnetotransport properties and thus provides a valuable tool for further investigations of MTJs.

R. Werner gratefully acknowledges support by the Cusanuswerk, Bischöfliche Studienförderung. This work was funded by the DFG (Projects KO 1303/8-1 and GO 944/3-1) and the German Excellence Initiative via the Nanosystems Initiative Munich (NIM). B.A.D. and A.Yu.P. acknowledge support by the FVG Regional project SPINOX funded by Legge Regionale 26/2005 and Decreto 2007/LAVFOR/1461.

[1]S. D. Bader and S. S. P. Parkins, Annu. Rev. Condens. Mater. Phys. **1**, 71 (2010).
[2]J. C. Slonczewski, Phys. Rev. B **39**, 6995 (1989).
[3]J. M. MacLaren, X.-G. Zhang, and W. H. Butler, Phys. Rev. B **56** (1997).
[4]M. Julliere, Phys. Lett. A **54**, 225 (1975).
[5]J. S. Moodera, L. R. Kinder, T. M. Wong, and R. Meservey, Phys. Rev. Lett. **74** (1995).
[6]R. Scheuerlein, W. Gallagher, S. Parkin, A. Lee, S. Ray, R. Robertazzi, and W. Reohr, ISSCC Dig. Tech. Papers, 128–129 (2000).
[7]J. S. Moodera, J. Nassar, and G. Mathon, Annu. Rev. Mater. Sci. **29**, 381 (1999).
[8]M. Bowen, J.-L. Maurice, A. Barthélémy, M. Bibes, D. Imhoff, V. Bellini, R. Bertacco, D. Wortmann, P. Seneor, E. Jacquet, *et al.*, J. Phys.: Condens. Matter **19**, 315208 (2007).
[9]M. R. Freeman and B. C. Choi, Science **294**, 1484 (2001).
[10]M. Wagenknecht, H. Eitel, T. Nachtrab, J. B. Philipp, R. Gross, R. Kleiner, and D. Koelle, Phys. Rev. Lett. **96**, 047203 (2006).
[11]R. Werner, A. Y. Petrov, L. A. Miño, R. Kleiner, D. Koelle, and B. A. Davidson, Appl. Phys. Lett. **98**, 162505 (2011).
[12]H. B. Wang, S. Guénon, J. Yuan, A. Iishi, S. Arisawa, T. Hatano, T. Yamashita, D. Koelle, and R. Kleiner, Phys. Rev. Lett. **102**, 017006 (2009).
[13]M. Veis, Š. Višňovský, P. Lecoeur, A.-M. Haghiri-Gosnet, J.-P. Renard, P. Beauvillain, W. Prellier, B. Mercey, J. Mistrík, and T. Yamaguchi, J. Phys. D **42**, 195002 (2009).
[14]See supplemenatry information at http://dx.doi.org/10.1063/1.3659301 for a detailed analysis of LTSLM signal generation.
[15]H. Jaffrès, D. Lacour, F. Nguyen Van Dau, J. Briatico, F. Petroff, and A. Vaurès, Phys. Rev. B **64**, 064427 (2001).
[16]R. Gross and D. Koelle, Rep. Prog. Phys. **57**, 651 (1994).
[17]Each image was taken in the following sequence: After preparing the MTJ at a certain value of H (and measuring $R(H)$), the field was reduced to $H = 0$, the image was taken, and the field was swept back to the initial value of H. During this sweep sequence, the resistance did slightly change (by typically $\pm 5 - 10\%$) but always returned back to the initial value. This procedure could partially explain the deviations between R and R_{calc} for $\alpha = 7°$ for field values above the resistance maximum [cf. Fig. 2(a)], as in this particular case the resistance upon sweeping back to $H = 0$ went up by up to 20%. However, this effect was much weaker in all other cases.

Supplementary information for: Local Tunneling Magnetoresistance probed by Low-Temperature Scanning Laser Microscopy

Robert Werner, Mathias Weiler, Aleksandr Yu. Petrov, Bruce A. Davidson,
Rudolf Gross, Reinhold Kleiner, Sebastian T. B. Goennenwein, and Dieter Koelle

(Dated: August 29, 2011)

We consider a planar magnetic tunnel junction (MTJ) where an in-plane magnetic field H is applied at an angle α with respect to the y-axis of the junction, cf. Fig. 1 (a).[1] An amplitude modulated focused laser beam is scanned across the sample surface in the (x, y)-plane. When the laser beam is positioned at coordinates (x_0, y_0) it locally warms up the MTJ, generating a change in the temperature-dependent local conductivity (conductance per area) g. This can be detected as a beam-induced change $\Delta V(x_0, y_0)$ of the voltage V across the sample, which is biased at constant current I. In the following, we derive a relation between the LTSLM voltage signal ΔV and the local conductance g, which shall be used for obtaining information on the local relative orientation (angle Θ) of the magnetizations in the two electrodes of the MTJ.

If the laser is on ('on-state') the sample has a temperature distribution $T(x - x_0, y - y_0) = T_0 + \delta T(x - x_0, y - y_0)$, where T_0 is the temperature of the undisturbed sample (off-state) and $\delta T(x - x_0, y - y_0)$ is the temperature profile created by the beam. Typically, δT has Gaussian shape, i.e.

$$\delta T(x - x_0, y - y_0) = \Delta T \exp\left\{-\frac{(x - x_0)^2 + (y - y_0)^2}{2\sigma^2}\right\} , \tag{1}$$

and ΔT is a few Kelvin and $\sigma \approx 1 - 2\,\mu$m. For some quantities introduced below, indices 'on' and 'off' refer to laser beam on and off, respectively.

The conductance of the sample in the off-state is given by

$$G_{\rm off} = \int_{A_J} g(x, y, \Theta(x, y), T_0)\; dxdy \tag{2}$$

where the local tunneling conductivity g may explicitly depend on the coordinates x and y, e.g., due to inhomogeneities in the tunnel barrier; T is the temperature and Θ is the relative angle of the local magnetizations of the two electrodes of the MTJ. Θ will in general be a function of x and y and depends on amplitude H and orientation angle α of the applied magnetic field. Integration is over the area A_J of the MTJ.

In the on-state the conductance is

$$G_{\rm on}(\Theta(x_0, y_0), x_0, y_0) = \int_{A_J} g(x, y, \Theta(x, y), T_0 + \delta T(x - x_0, y - y_0))\; dxdy\; . \tag{3}$$

A Taylor expansion leads to

$$G_{\rm on}(\Theta(x_0, y_0), x_0, y_0) \approx \int_{A_J} \left[g(x, y, \Theta(x, y), T_0) + \frac{dg(x, y, \Theta(x, y), T)}{dT}\;|_{T_0}\; \delta T(x - x_0, y - y_0)\right] dxdy\; . \tag{4}$$

Hence, for the laser induced change in conductance $\Delta G \equiv G_{\rm on} - G_{\rm off}$ we find by inserting Eq. (2) in Eq. (4)

$$\Delta G(\Theta(x_0, y_0), x_0, y_0) \approx \int_{A_J} \frac{dg(x, y, \Theta(x, y), T)}{dT}|_{T_0}\; \delta T(x - x_0, y - y_0)]\; dxdy\; . \tag{5}$$

This means, that ΔG is the convolution of $g' \equiv dg/dT$ (at $T = T_0$) with the beam induced temperature profile.

The voltage across the TMR element is $V_{\rm off} = I/G_{\rm off}$ in the off-state, and $V_{\rm on} = I/G_{\rm on}$ in the on-state. For the beam induced voltage change $\Delta V(x_0, y_0) = V_{\rm on}(x_0, y_0) - V_{\rm off}$ we thus find

$$\begin{aligned}
\Delta V(\Theta(x_0, y_0), x_0, y_0) \;&\equiv\; \frac{I}{G_{\rm off}}\left(\frac{1}{1 + \Delta G(\Theta(x_0, y_0), x_0, y_0)/G_{\rm off}} - 1\right) \\
&\approx\; -\frac{I}{G_{\rm off}^2}\Delta G(\Theta(x_0, y_0), x_0, y_0) \\
&=\; -IR_{\rm off}^2\Delta G(\Theta(x_0, y_0), x_0, y_0)
\end{aligned} \tag{6}$$

Here we assumed that $\Delta G/G_{\rm off} \ll 1$ and also introduced the resistance $R_{\rm off}$ of the MTJ in the off-state at a given H, α and T_0.

We next relate $\Delta G(\Theta(x_0,y_0),x_0,y_0)$ to the values G_p and G_{ap} of the conductance for parallel and antiparallel alignment of magnetizations. For the local conductivity $g(\Theta(x,y),T_0,x,y)$ we have the relation by Jaffres *et al.*[2]

$$g(\Theta(x,y),T_0,x,y) = g_p(T_0,x,y)\cos^2\{\frac{\Theta(x,y)}{2}\} + g_{ap}(T_0,x,y)\sin^2\{\frac{\Theta(x,y)}{2}\}\ , \tag{7}$$

where the indices 'p' and 'ap' stand for parallel and antiparallel alignment, respectively, of the magnetizations in the two electrodes. Eq. (7) can be written as

$$g(\Theta(x,y),T_0,x,y) = \frac{g_p(T_0,x,y)+g_{ap}(T_0,x,y)}{2}\left[1+\frac{g_p(T_0,x,y)-g_{ap}(T_0,x,y)}{g_p(T_0,x,y)+g_{ap}(T_0,x,y)}\cos\{\Theta(x,y)\}\right] \tag{8}$$

For the derivative of $g(\Theta(x,y),T_0,x,y)$ with respect to temperature we obtain

$$g'(\Theta(x,y),T_0,x,y) = \frac{g'_p(T_0,x,y)+g'_{ap}(T_0,x,y)}{2}\left[1+\frac{g'_p(T_0,x,y)-g'_{ap}(T_0,x,y)}{g'_p(T_0,x,y)+g'_{ap}(T_0,x,y)}\cos\{\Theta(x,y)\}\right] \tag{9}$$

where we have assumed that Θ does not depend on T. Inserting Eq. (9) into Eq. (5) yields

$$\Delta G(\Theta(x_0,y_0),x_0,y_0) \approx \int_{A_J} \frac{g'_p(T_0,x,y)+g'_{ap}(T_0,x,y)}{2}\left[1+\frac{g'_p(T_0,x,y)-g'_{ap}(T_0,x,y)}{g'_p(T_0,x,y)+g'_{ap}(T_0,x,y)}\cos\{\Theta(x,y)\}\right]\delta T(x-x_0,y-y_0)dxdy \tag{10}$$

For further evaluation we assume that $g(\Theta(x,y),T_0,x,y)$ for a fixed value of Θ does not depend on x and y, i.e., we assume that the MTJ is homogeneous except for local variations in $\Theta(x,y)$. This is supported e.g. by the homogeneous LTSLM images obtained for antiparallel magnetization orientation, cf. Fig. 2. Then, $g'_p(T_0,x,y)$ and $g'_{ap}(T_0,x,y)$ are constant in space and can be calculated from the global quantities $G'_p(T_0)$ and $G'_{ap}(T_0)$ as $g'_p = G'_p/A_J$ and $g'_{ap} = G'_{ap}/A_J$.

Eq. (10) then reduces to

$$\begin{aligned}\Delta G(\Theta(x_0,y_0),x_0,y_0) &\approx \int_{A_J}\frac{(G'_p+G'_{ap})_{|T_0}}{2A_J}\left[1+\left(\frac{G'_p-G'_{ap}}{G'_p+G'_{ap}}\right)_{|T_0}\cos\{\Theta(x,y)\}\right]\delta T(x-x_0,y-y_0)dxdy \\ &= \frac{(G'_p+G'_{ap})_{|T_0}}{2A_J}\left[\int_{A_J}\delta T(x-x_0,y-y_0)dxdy + \left(\frac{G'_p-G'_{ap}}{G'_p+G'_{ap}}\right)_{|T_0}\int_{A_J}\cos\{\Theta(x,y)\}\delta T(x-x_0,y-y_0)dxdy\right]\end{aligned} \tag{11}$$

Using Eq. (1) we obtain

$$\Delta G(\Theta(x_0,y_0)) \approx (G'_p+G'_{ap})_{|T_0}\frac{\Delta T A_s}{2A_J}\left[1+\left(\frac{G'_p-G'_{ap}}{G'_p+G'_{ap}}\right)_{|T_0}\langle\cos\{\Theta(x_0,y_0)\}\rangle\right]\ . \tag{12}$$

Here, $A_s{=}2\pi\sigma^2$ is the approximate size of the area warmed up by the laser, and $\langle\cos\{\Theta(x_0,y_0)\}\rangle = \frac{1}{\Delta T A_s}\int_{A_J}\cos\{\Theta(x,y)\}\delta T(x-x_0,y-y_0)dxdy$.

At this point, by inserting Eq. (12) into Eq. (6), we can determine the magnitude of the LTSLM voltage signals ΔV_p and ΔV_{ap} for homogeneous parallel ($\Theta = 0$) and antiparallel ($\Theta = 180°$) magnetization of both electrodes, respectively. For ΔV_p, with $R_{\rm off} = R_p$ and $\langle\cos\{\Theta(x_0,y_0)\}\rangle = 1$, we obtain $V_p = 2I\Delta T A_s/A_J \cdot R'_p|_{T_0}$. For ΔV_{ap}, with $R_{\rm off} = R_{ap}$ and $\langle\cos\{\Theta(x_0,y_0)\}\rangle = -1$, we obtain $V_{ap} = 2I\Delta T A_s/A_J \cdot R'_{ap}|_{T_0}$. This shows that for these two cases, the voltage signal is proportional to the derivative of the junction resistance with respect to T and that the contrast for the voltage signals between parallel and antiparallel states can be maximized by choosing an operation temperature T_0 which yields a maximum difference in the slopes of the $R_p(T)$ and $R_{ap}(T)$ curves.

By converting Eq. (12), we find for the convolution $\langle\cos\{\Theta(x_0,y_0)\}\rangle$ of the local value of $\cos\{\Theta(x,y)\}$ with the laser beam induced temperature profile

$$\langle\cos\{\Theta(x_0,y_0)\}\rangle \approx \left(\frac{G'_p+G'_{ap}}{G'_p-G'_{ap}}\right)_{|T_0}\left[\frac{2A_J\Delta G(\Theta(x_0,y_0))}{\Delta T A_s(G'_p+G'_{ap})_{|T_0}}-1\right]\ . \tag{13}$$

This equation can be used to calculate the local variation of $\langle\cos\Theta\rangle$ from the beam-induced voltage signal ΔV, i.e., inserting $\Delta G(\Theta(x_0,y_0))=-\Delta V(\Theta(x_0,y_0))/IR_{\rm off}^2$ from Eq. (6) into Eq. (13) finally yields

$$\langle\cos\{\Theta(x_0,y_0)\}\rangle \approx a_1\frac{\Delta V(\Theta(x_0,y_0))}{R_{\rm off}^2}+a_2 \tag{14a}$$

$$\text{with}\quad a_1\equiv\frac{2A_J}{I(G'_{ap}-G'_p)_{|T_0}\Delta TA_s}\qquad\text{and}\qquad a_2\equiv\left(\frac{G'_p+G'_{ap}}{G'_{ap}-G'_p}\right)_{|T_0}\ . \tag{14b}$$

The coefficients a_1 and a_2 can be determined experimentally. In order to obtain maximum contrast between parallel and antiparallel magnetization orientation, we chose $T_0 = 30\,\mathrm{K}$, i.e., the temperature for which we found the maximum difference in the slopes of the $R(T)$ curves for high-R and low-R states [cf. Fig. 2(c)]. $G'_p|_{T_0}$ and $G'_{ap}|_{T_0}$ can be measured, provided that the magnetizations in the electrodes in the MTJ are uniform. Our LTSLM images indicate that this is essentially the case for $\alpha = 70^\circ$ and antiparallel orientation, cf. Fig. 2(b)9, yielding $G'_{ap}|_{T_0} = 0.16\,(\mathrm{M\Omega}\,K)^{-1}$ from Fig. 1(c) at $T_0 = 30\,\mathrm{K}$.

By contrast, for parallel orientation LTSLM imaging revealed some local variations of ΔV, requiring a more careful evaluation of $G'_p|_{T_0}$. We first use $G'_{ap}|_{T_0}$ to determine the product ΔTA_s, which is not known with high accuracy a priori. From Eq. (12), using $\langle\cos(\Theta(x_0,y_0))\rangle = -1$ and $\Delta G(\Theta(x_0,y_0)) = \Delta G_{ap}$ we find

$$\Delta TA_s = \frac{\Delta G_{ap}A_J}{G'_{ap}|_{T_0}} = -\frac{A_J\Delta V_{ap}}{G'_{ap}|_{T_0}IR_{\rm off}^2} \tag{15}$$

With the measured $\Delta V_{ap} = -20\mu V$ and $R_{\rm off} = 18.3\,\mathrm{k\Omega}$ for the antiparallel state at $\alpha = 70^\circ$ we obtain $\Delta TA_s = 14\,\mathrm{K}(\mu\mathrm{m})^2$. From the most abrupt change of $\Delta V(\Theta(x_0,y_0))$ in the LTSLM voltage images we can estimate $\sigma \approx 0.8\,\mu\mathrm{m}$ and with this we get $\Delta T \approx 3.5\,\mathrm{K}$, which is reasonable.

The above value of the product ΔTA_s is the same for all images. Thus, to obtain $G'_p|_{T_0}$ we use this value and the relation $G'_p|_{T_0} = -A_J\Delta V_p/(IR_{\rm off}^2\Delta TA_s)$, where for ΔV_p we use a value measured in the center of the MTJ where the magnetizations were in the parallel configuration, cf. Fig. 2(b)1. With $R_{\rm off} = 4.5\,\mathrm{k\Omega}$ and $\Delta V_p = 5\mu V$ we obtain $G'_p|_{T_0} = -0.66\,(\mathrm{M\Omega\,K})^{-1}$.

Having all parameters fixed now, we convert all LTSLM images, by calculating $\langle\cos(\Theta(x_0,y_0))\rangle$ from Eq. (14), which yields

$$\langle\cos(\Theta(x_0,y_0))\rangle = 4.0\,\frac{(\mathrm{k\Omega})^2}{\mu\mathrm{V}}\,\frac{\Delta V(x_0,y_0)}{R_{\rm off}^2} - 0.6\ , \tag{16}$$

for $I = 4\,\mu\mathrm{A}$; these images are shown in the right panel of Fig. 2.

We further use $\cos(\Theta(x,y)) \approx \langle\cos(\Theta(x_0,y_0))\rangle$ to re-calculate the conductance $G(H)$ from the converted LTSLM images (at given field H and angle α) by integrating Eq. (8) over the junction area. Here, we use $g_{ap} = G_{ap}/A_J = 1/(R_{\rm max}A_J) = 0.36\,(\mathrm{M\Omega})^{-1}\mu\mathrm{m}^{-2}$ with $R_{\rm max} = 18.3\,\mathrm{k\Omega}$ as determined from Fig.2(b), which is justified by the homogenous LTSLM images 8-10 in Fig. 2(b). Since we know from the LTSLM images that the low-R state ($R_{\rm min} \approx 4.5\,\mathrm{k\Omega}$) is inhomogeneous, we cannot simply calculate g_p from $1/(R_{\rm min}A_J)$. Instead, we use g_p as a fitting parameter, to obtain after integration of Eq. (8) for the low-R state $G = (4.5\,\mathrm{k\Omega})^{-1}$. This yields $g_p = 1.51\,(\mathrm{M\Omega})^{-1}\mu\mathrm{m}^{-2}$, which corresponds to $R_p = 1/(g_pA_J) = 4.41\,\mathrm{k\Omega}$, i.e., a value which is $\sim 2\,\%$ smaller than the measured $R_{\rm min}$. From here we obtain $\mathrm{TMR}(H) = [R(H) - R_{\rm min}]/R_{\rm min} = G_{\rm min}/G(H) - 1$ (with $G_{\rm min} \equiv 1/R_{\rm min}$), cf. triangles in Fig. 2.

---

[1] Throughout this text Fig. numbers refer to the figures in the main paper.

[2] H. Jaffrès, D. Lacour, F. Nguyen Van Dau, J. Briatico, F. Petroff, A. Vaurès, Phys. Rev. B **64**, 064427 (2001); Ref. [14] in the main paper.